AN OPTO-ELECTRONIC MEMS OSCILLATOR

for
Resonant Pressure Sensing

Lalit Kumar

Master of Science Thesis

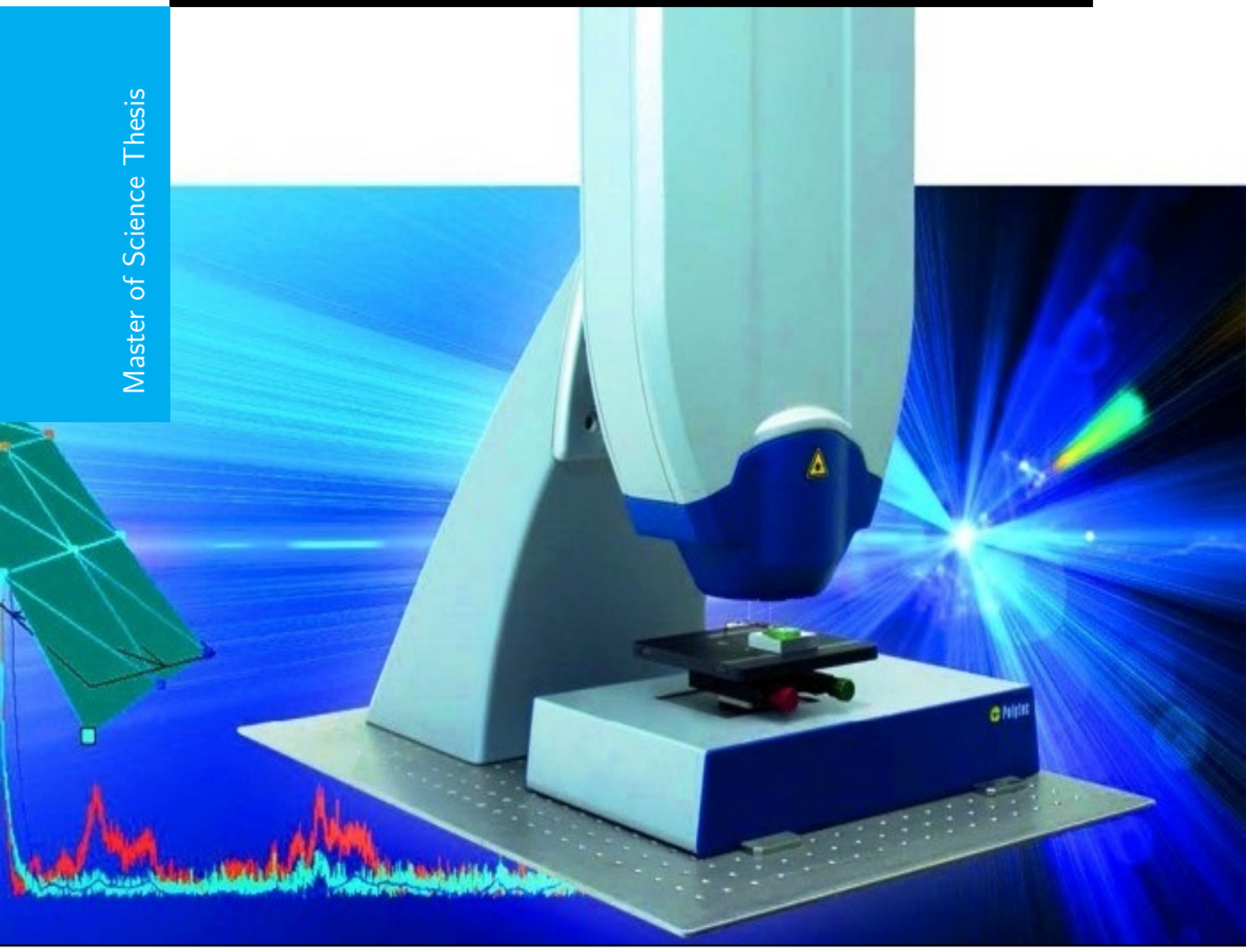

TU Delft Delft University of Technology

Delft Institute of Microsystems and Nanoelectronics

AN OPTO-ELECTRONIC MEMS OSCILLATOR

for

Resonant Pressure Sensing

Master of Science Thesis

For the degree of Master of Science in Electrical Engineering
(Microelectronics) at Delft University of Technology

Lalit Kumar

July 11, 2014

Faculty of Electrical Engineering, Mathematics and Computer Science (EEMCS) · Delft University of Technology

Approved by

Responsible Professor
Prof.dr.ir. P.M. Sarro
Faculty of Electrical Engineering, Mathematics and Computer Science
Delft University of Technology

Supervisor
Prof.dr. Peter Steeneken
Faculty of Applied Science
Delft University of Technology
Principal Scientist-Central R & D
NXP Semiconductors

Third reader & Committee member
Prof.dr.ir. Paddy French
Faculty of Electrical Engineering, Mathematics and Computer Science
Delft University of Technology

The work in this thesis was supported by NXP Semiconductor, Netherlands. Their cooperation is hereby gratefully acknowledged.

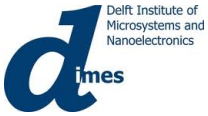

Abstract

This thesis details the design of a self-oscillating MEMS resonator as a pressure sensor. A bi-layer circular diaphragm with a single center perforation is used as a pressure sensitive membrane which measures the absolute pressure of the surrounding medium. A novel aspect of the proposed sensor is that the resonator is made to oscillate by an opto-electronic feedback loop. The membrane is driven electrostatically and it's motion is sensed optically. The optical read-out system measures the velocity of the driven membrane which is subsequently converted into electrical signals for actuation. The proposed opto-electronic MEMS oscillator uses Laser Doppler Vibrometry for detection as well as signal conversion and amplification which to our knowledge has not been reported so far.

Expressions for the resonant frequency and relative pressure sensitivity of the MEMS sensor are based on driven harmonic oscillators and Bao's analytical model for squeeze film damping. A pressure sensitivity of 1 Hz/Pa was measured. The minimum detectable pressure i.e. the resolution is estimated from Allan deviation measured for the oscillator at different pressures. With a measurement time of 1 ms, a lowest resolution of 5 Pa is achieved at atmospheric pressure (10^5 Pa, Q=50, f_o=600 kHz). The performance in terms of linearity, accuracy/stability and resolution is limited by the noise injected from the optical system and is expected to improve for an all-electrical MEMS oscillator.

To have a deeper insight, 32 kHz quartz crystals were configured in both oscillator types-opto-electronic and all-electrical Pierce topology. Tuning fork based resonators behave similar to MEMS resonators but exhibit higher Q and lower pressure sensitivity. An experimental sensitivity of 50 μHz/Pa with a Q=12,500 (10^5 Pa). The noise behavior for both MEMS and tuning fork based opto-electronic oscillators were similar. However, Tuning fork based Pierce oscillator showed 100 times better noise performance in comparison to opto-electronic topology. This translated into a 20 times better resolution. In terms of frequency stability, Pierce oscillators were 1000 times better than opto-electronic oscillator.

The experimental data for the proposed self-oscillating MEMS pressure sensor are comparable to the existing state-of-the-art-pressure sensor technologies (piezoresistive and capacitive sensing) and the concept certainly has a competitive potential for resonant pressure sensors. Power consumption is one important factor for which the experimental data is lacking and further work is required to comment on sensor's complete feasibility.

Preface and Acknowledgements

The thesis work-ET4400 is written as a partial requirement for completion of the *Master of Science* in *Microelectronics* at the *faculty of Electrical Engineering, Mathematics and Computer Science*, at *Delft University of Technology*. The work discussed here has been performed within the the research group - *Advanced Devices, Process and Technology* at *NXP Semiconductors*, Netherlands.

The project is focussed on a conceptual design of a MEMS resonant pressure sensor with better performance than the currently used pressure sensor technologies in the market. The goal of this project is also to educate the reader on MEMS sensors and to explore the possibilities of smart and efficient engineering solutions using MEMS resonator. The report covers the research performed in the domain of opto-electronics and electro-mechanics over the span of 12 months. The process saw some difficulties in certain aspects and it would not be possible to bring this thesis to a success without the constant support, encouragement and help from the people involved. I would therefore like to express my sincere gratitude to

Prof. Lina Sarro for accepting me as a thesis student under her supervision and allowing me to be a part of the research group - ECTM (Electronic Components, Technology and Materials) and Dr. Twan van Lippen for allowing me to carry my research work within NXP. The project would not have started without their approval.

Prof. Peter Steeneken for his guidance as my direct/daily supervisor. His constant encouragement and feedback has been one of the major driving force that kept me motivated during the course of the project. I would also like to thank him for his valuable time for meetings and discussions and helping me publish some of my work.

To the pressure sensor group at NXP research. In particular, I am very thankful to Martijn Goossens and Klaus Reimann for their generous assistance and giving me the benefit of their significant experience. I am also grateful to Oswald Moonen for his practical assistance in circuit implementation.

Prof. Paddy French for his participation in thesis defense committee and Prof. Andre Bossche for his support as my master co-ordinator.

My fellow peers and master students at NXP and Delft University with whom I enjoyed my time and shared my experience.

My family for their unconditional support and who are eagerly waiting to see me graduate.

Last but the not the least, I would like to thank my teachers, friends or anyone who helped me during my master studies.

Delft, University of Technology Lalit Kumar
July 11, 2014

Table of Contents

List of Figures

List of Tables

Table 1: List of Symbols used.

Character	Designation	Unit
Q	Quality factor	-
m	Mass of the resonator	kg
k	Spring Constant	N/m
b	Damping coefficient	N.s/m
ζ	Damping factor	-
t	Time	s
x	Displacement of resonator	m
X_o	Peak value of displacement (amplitude) $x(t)$	m
$X(\omega)$	Fourier transform of $x(t)$	-
$f(t)$	Driving force function	N
F_o	Peak value of driving force	N
$F(\omega)$	Fourier transform of $f(t)$	-
ω_o	Resonant frequency	rad/s
ϕ	Phase	rad
$H(\omega)$	Magnification factor	-
ω_i	Input drive frequency	rad/s
i	imaginary number $\sqrt{-1}$	-
τ_d	Diffusion time	s
τ_A	Measurement time	s
$R(\tau)$	Auto-correlation function	-
$S(\omega)$	Spectral density function	Unit^2/Hz
S_o	Power spectral density of white noise	V^2/Hz
B_f	Bandwidth	rad/s
$S_x(\omega)$	Displacement	m^2/Hz
S_v	Velocity spectral density	$(\text{mm/s})^2/\text{Hz}$
μ	Coefficient of viscosity	Pa.s
A	Area of the circular resonator	m^2
h	thickness of the circular resonator	m
g_o	air gap within the resonator	m
K_n	constant where n refers to mode of vibration	-
w	uniform load per unit area	N/m^2
r	radius of circular membrane	m
r_h	radius of hole	m
N	Number of perforations in the membrane	-
g	gravitional acceleration	m/s^2
D	material's flexural rigidity	N/m^2
E	Materials Young modulus	Pa
ν	Poisson ratio	-
ρ	Specific mass of resonator	N/m^3
R	Universal gas constant	Nm/mole.K
ϵ_o	vacuum permittivity	F/m
k_B	Boltzmann constant	J/K
K_n	Knudsen number	-

Character	Designation	Unit
T	Temperature	K
M_m	Molecular weight of air	kg
p	Pressure	Pa
V	Voltage	V
I	Current	A
q	charge	C
υ	velocity	m/s
R_m	Motional resistance	Ω
L_m	Motional inductance	H
C_m	Motional capacitance	F
C_o	Shunt capacitance	F
η	Electro-mechanical coupling coefficient	-
P	Power	W
E_c	Energy per cycle	J
Z	Electrical impedance	Ω
G	Transfer function	-
$\vec{E}$	Electric Field	N/mC
λ	Wavelength	m
f	Frequency	Hz
I	Intensity of wave	W/m^2
F	Noise Figure	-
U	Noise Source	-
S_p	Relative pressure sensitivity	Pa^{-1}
$\alpha(t)$	Signal amplitude fluctuations	-
$\varphi(t)$	Phase fluctuations	-
ω_{osc}	Oscillator frequency	rad/s
$\Delta\omega$	Offset frequency	Hz
S_ϕ	Phase noise spectral density	dBc/Hz
S_f	Frequency noise spectral density	dBc/Hz
σ_D	Allan deviation	-

Chapter 1

Introduction

1-1 Micro-Electromechanical System (MEMS) Sensor Technology

"They tell me about electric motors that are the size of the nail on your small finger. It is a staggeringly small world that is below", said Richard Feynman while addressing the American Physical Society in 1959 during his now famous talk entitled "there is plenty of room at the bottom" [1]. He thought about control systems at small scale and gave a hope of replacing bulky electromechanical sensor of the day by small rugged device in the same way that transistors had replaced thermionic valves in 1947. This possibility was arguably first considered in 1954 when C.S. Smith discovered the phenomena of piezoresistivity in silicon and germanium. Smith's paper [2] was probably the first publication responsible for the origin of what we now know as *Micro-Electromechanical System (MEMS)* as it showed that silicon and germanium could sense air or water pressure better than metals [3]. It was after this discovery that series of papers from Bell Labs and Honeywell Research center described the first silicon diaphragm pressure sensors in 1961 [4]. Soon, silicon sensor technology gained interest and a number of companies commercializing this field grew up by the late 1960s. The first silicon pressure sensor (Figure 1-1a) can be considered as crude by today's standard but it was in the early 1970s when proliferation of bulk-etched silicon wafers was done to make silicon sensors. Subsequent progress in silicon processing during 1970s and development in micro-machining, lead to sensors with non-planar geometries with superior performance. But today's MEMS sensors (Figure 1-1b) are much more miniature in size in the order of a millionth of a meter (micrometer). They are also referred to as *micro-machines, micro-systems, micro-mechanics* or *Micro System Technology (MST).*

The term MEMS is applied to all miniaturized devices which are mostly fabricated from silicon using various conventional and recently discovered "*state of the art*" micro-engineering fabrication techniques like etching, thin film deposition, masking and doping techniques related to IC manufacture. These devices are present in our everyday life. They have been interfacing with the electronic circuit and systems with its wide range of applications in the form of numerous transducers like inertia sensors (accelerometer, gyroscope), pressure sensors, bioMEMS (DNA chips, micro-bio analysis system etc.), optical MEMS (optical fiber switch,

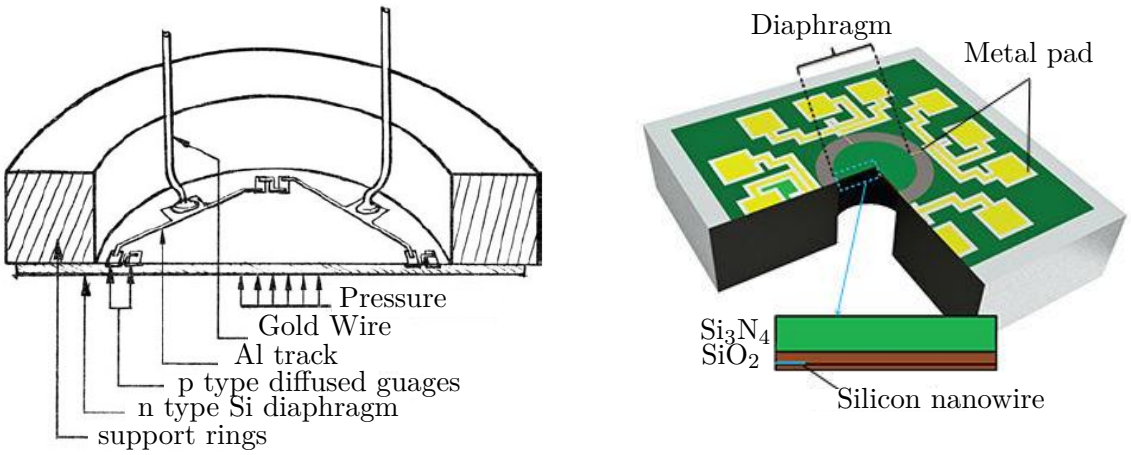

(a) **(b)**

Figure 1-1: Schematic section of an early silicon pressure sensor (a) with a non-micro-engineered diaphragm mounted on the support rings and [4] a modern MEMS pressure sensor (b) with a non-planar micro-engineered diaphragm [5].

micro-mirror array), RF MEMS (antenna filters, switches) and many others. The present day situation of MEMS sensor technology is that it has a major influence on physical sensing and to some extent on gas sensing and recently on chemical sensing. In physical sensing, the impact on pressure sensing has been the most [7]. Today's pressure sensors are much more superior and exceedingly small and capable of detecting pressures by exploiting various phenomena like capacitive, piezoresistivity etc. as discussed in the following section.

1-2 MEMS Pressure Sensor

Unlike all the physical variables like vibration, motion, rotation, inclination, strain, sound etc., MEMS technology has been particularly successful in pressure sensing domain. Several industries require sensors for pressure measurements and MEMS silicon sensors accommodates a large range of pressure by changing the diaphragm dimensions combined with high performance, high-volume batch fabrication and low unit costs. Pressure sensors are expected to produce a total of $ 1.68 billion in 2013 [8], 75 % of which is the outcome of automotive sectors ($ 1.26 billion) while the rest comes from military and aerospace sectors, consumer electronics and medical industries. Figure 1-2 shows an estimated market share of pressure sensor and it's future prospects.

Modern pressure sensor are fabricated by lithographic and non-lithographic techniques. These techniques can be further categorized into bulk micro-machining, surface micro-machining and Lithographie Galvanoformung Abformung (LIGA). The first two techniques are used for producing 2D structures [9] . The various steps involved are shown in Figure 1-3. Bulk micromachining uses anisotropic etching to remove materials while in surface micro-machining, thin films of structural and sacrificial layers are deposited and etched. The end product of both the techniques is a freestanding structure known as a diaphragm. The suspended structure is deflected in response to the surrounding/applied pressure. Depending on the

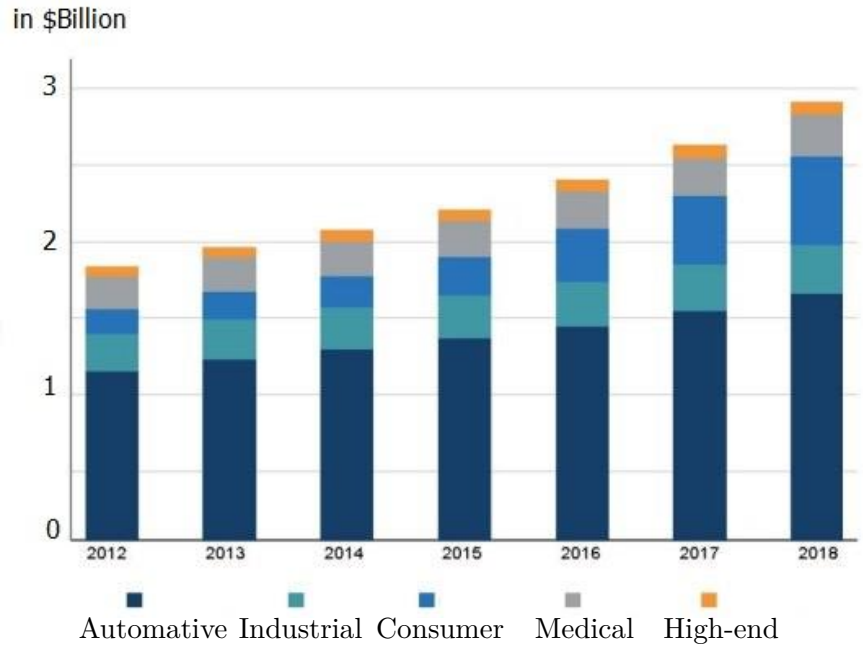

Figure 1-2: MEMS pressure sensor market forecast by applications (2012-2018). *Adapted from i-micronews.com-April 2013.*

structure, the magnitude of deflection is directly or indirectly proportional to the pressure. A suitable transduction mechanism is required which converts the mechanical deformation into electrical signals which can be used to extract pressure by data acquisition electronics. For pressure sensors, different transduction mechanisms have been investigated namely piezoelectric effect of thin films, piezoresistive effect in silicon, optical deflection of suspended films, capacitive effect due to diaphragm deflection, stress effects in p-n junction and frequency shift of resonating structures [10], [11] . Out of these, piezoresistive effect and capacitive effect are most commonly used today. Other pressure sensors are based on resonant transduction which requires a much more advanced sensing scheme and are suited for only certain application.

1-2-1 Piezoresistive sensor

The first pressure sensor demonstrated in 1969 was based on diffused resistors in thin silicon diaphragm and was based on the principle of piezoresistivity in silicon [13]. Since then, piezoresistivity has become the most conventional method in the design of pressure sensors. Piezoresistivity is the property of a material by which a change in the resistivity is observed when the material is subjected to mechanical deformation. Silicon and other semiconducting materials like germanium are piezoresistive in nature. In piezoresistive pressure sensors, semiconductor resistors are assembled on the membrane which experience strain when subjected to stress due to applied external pressure. The change in the resistance is detected by electrical read-out circuits to extract pressure data. The resistors are embedded usually at the edge of the diaphragm where the stress induced strain is maximum and connected in a half-bridge or a full-bridge configuration. Figure 1-4 shows a piezoresistive pressure sensor [12] in a full

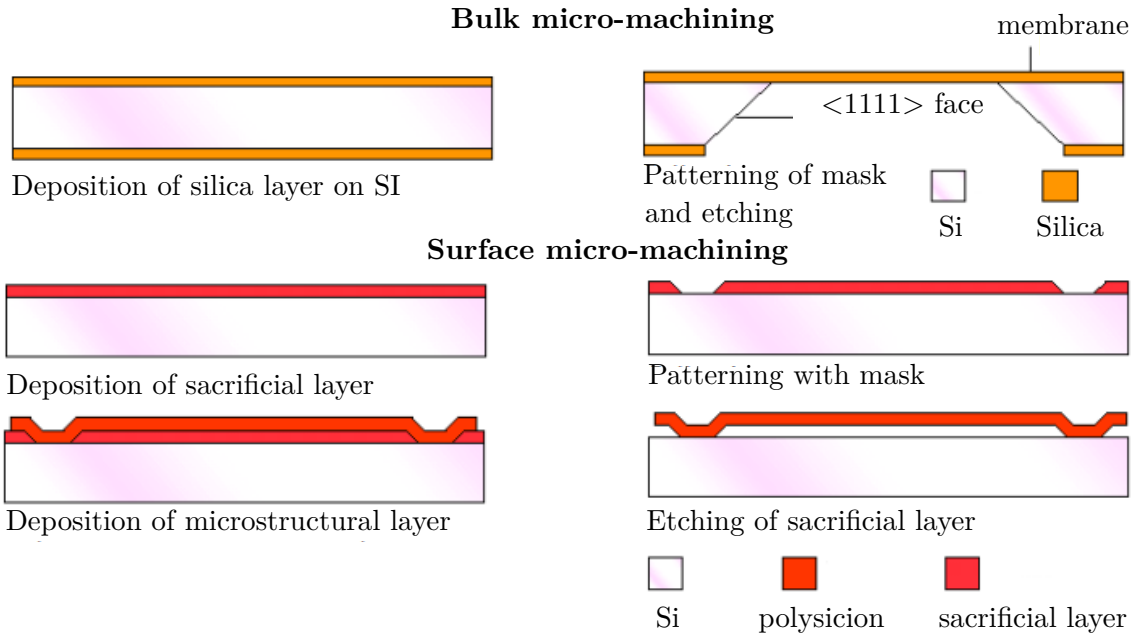

Figure 1-3: Schematic of the process steps involved in bulk micro-machining and surface-micro-machining fabrication of MEMS [6].

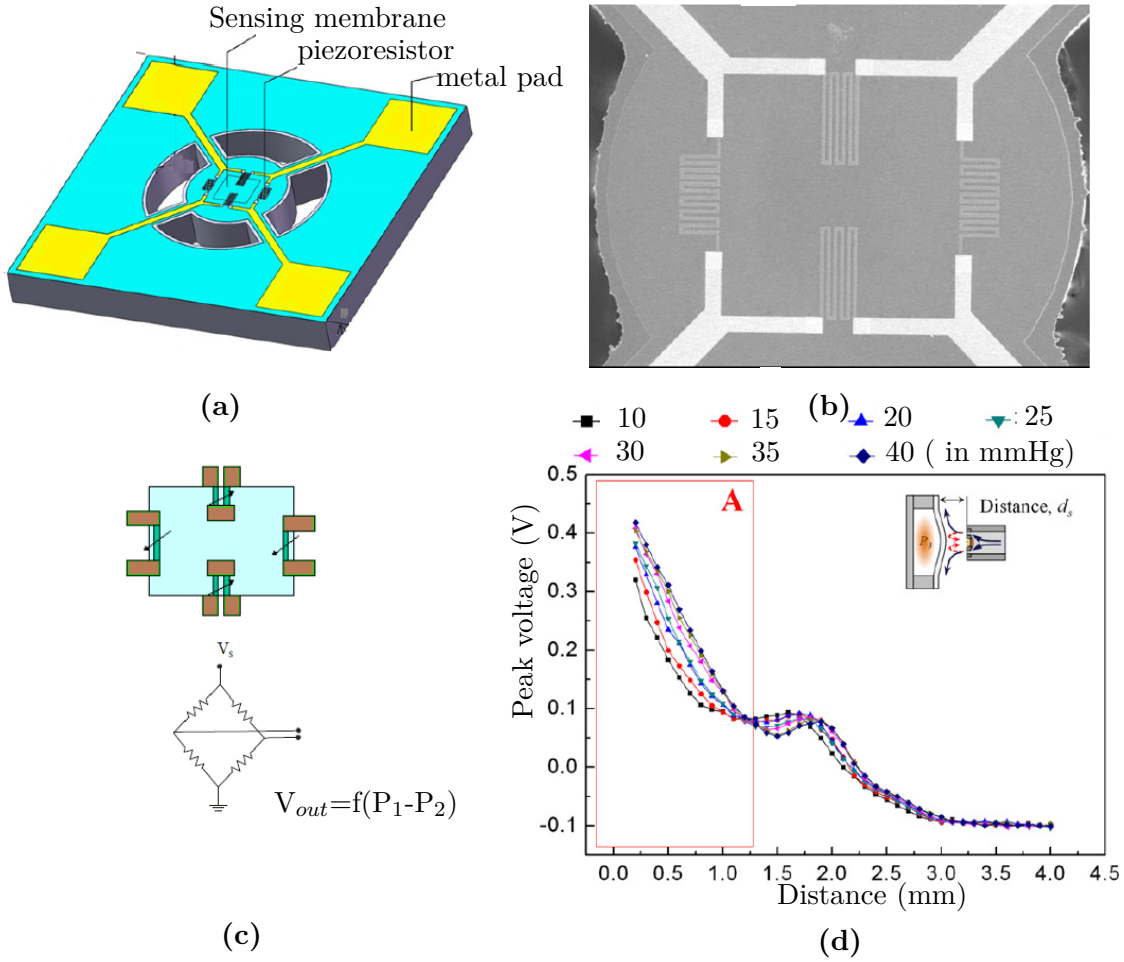

Figure 1-4: (a) Overall view of a piezoresistive pressure sensor. The hollow cylindrical like structure provides the necessary gap for air flow. (b) Scanning Electron Microscopy (SEM) image of MEMS device. (c) Electrical equivalent -Wheatstone bridge network. The output voltage is directly proportional to differential pressure acting on both sides of the membrane. Here f is the proportionality factor. (d) Measured output voltage *vs* distance at different pressures for the proposed micro-relected air pressure sensor. The output voltage is a function of the reflected air pressure from the surface of cornea (of a human eye) seperated by the sensor's membrane at a distance d. For a small d, large amount of reflected air is sensed by the membrane. [12].

bridge configuration. A differential pressure on the membrane results into deflection which changes the resistance thereby shifting the balance point of the wheat-stone bridge.

Piezoresistive sensor is a mature technology and are fabricated by both surface machining and bulk etching and widely used because of their high sensitivity, good linearity, reliability and reduced influence of process fluctuations on the output characteristics [14]. However it does offer some disadvantages. The pressure sensitivity is dependent on shape of the membrane [15] and is limited by small fractional change in resistance of piezoresistors. Temperature dependent resistance and thermal expansion of the membrane requires temperature compensation blocks leading to decreased sensitivity and increased complexity [16].

1-2-2 Capacitive sensor

The capacitive pressure sensors are based on parallel-plate capacitor, the capacitance of which is a function of applied pressure. The sensor consists of 2 electrodes, a fixed bottom electrode and a top electrode attached to the diaphragm as shown in Figure 1-5. In response to external applied pressure, the deflection of the membrane is detected as a variation in capacitance between the 2 electrodes. The output is a change in the capacitance which can be converted into electrical signals to extract pressure information. Different modes of actuation and detection are discussed in [17]. Capacitance changes inversely with pressure and hence the response is not linear as seen from Figure 1-5.

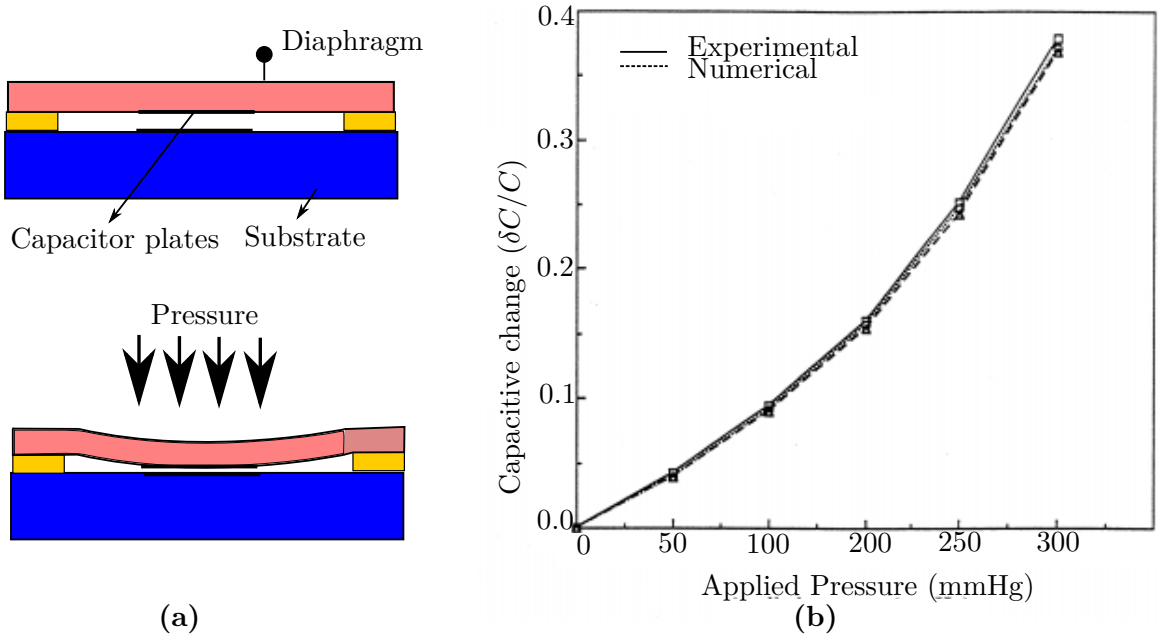

Figure 1-5: (a) Principle of capacitive pressure sensor. The deflection of membrane reduces the gap between the two plates thereby increasing the capacitance at higher pressures as shown in (b) which shows a non-linear relation (adapted from [18]).

For the same geometry of resonator, capacitive pressure sensors offer much higher sensitivity compared to piezoresistive sensors [19] as the capacitive change is much larger than resistive changes. For the same geometry, change in the capacitance is 10-20 % whereas the resistive

changes are in the order of 2-5%. The sensor also eliminates resistive losses and hence consumes less power. One of the key advantage over piezoresistive sensor is their potentially lower temperature sensitivity. However the main drawback of capacitive detection is susceptibility to parasitic effects due to small external capacitances. High output impedance, non-linearity of transducer response and the need for signal conditioning and amplification are some of the other drawbacks of capacitive detection.

1-2-3 Optical sensor

Optic fiber based sensors have been widely used to measure various physical and chemical parameters. In optical sensor, pressure induced deflection of thin flexible diaphragm is measured by Fabry-Perot based [20] or Mach-Zehnder based interferometry methods [21]. The deflection measurement from optical fiber sensor read-out varies linearly with pressure as shown in Figure 1-6. Optical sensors offers high accuracy and immunity to Electro Magnetic Interference (EMI) interferences (noise) but they do suffer from temperature sensitivity problems due to optical heating. Furthermore, large power is required. The experimental setup also requires aligning of optical lenses and calibration in the presence of drift and external vibrations.

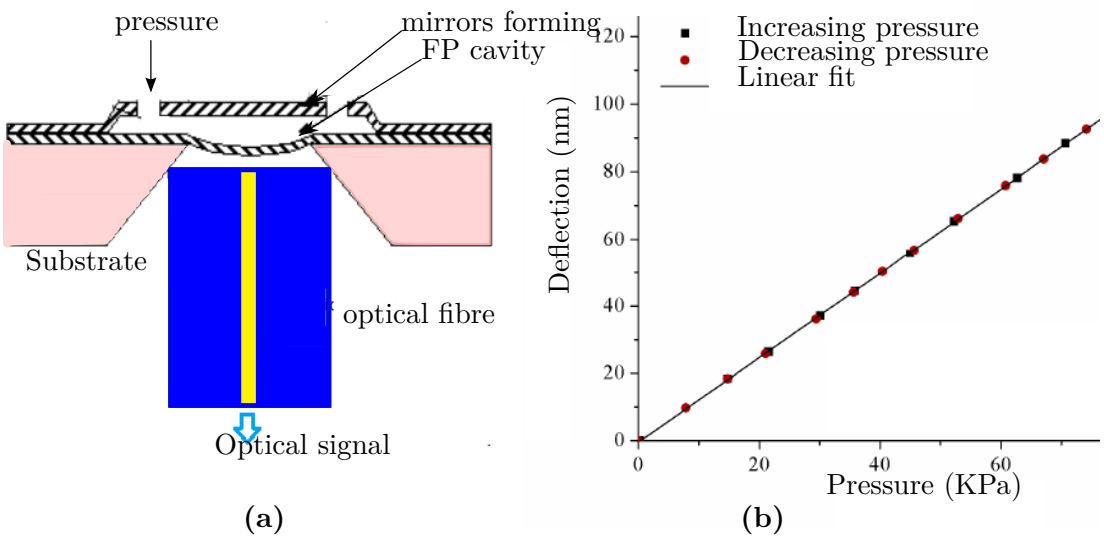

Figure 1-6: (a) Principle setup of optical pressure sensor. The deflection of membrane is sensed by optical signals through fiber read-out scheme. (b) shows a linear relation between pressure and deflection (adapted from [20]).

1-2-4 Resonant sensor

The mechanical frequency of a membrane can be changed by application of stress due to external force or pressure. This principle is used in conventional MEMS devices and are categorized as resonant sensors. Resonant pressure sensors are new class of devices which have been reported in the last decades. They sense the pressure by monitoring the resonant

frequency of a suspended beam or diaphragm which is a function of applied pressure. Frequency read-out can be done entirely in digital domain by various zero-counting algorithms and hardware and as such conversion from analog signals to digital data is not required as compared to the previously discussed pressure sensors. Since the frequency can be extracted with high degree of accuracy, resonant sensors offer higher sensitivity which otherwise is only limited to the resolution of frequency measurement system. Another reason why frequency measurement can offer higher sensitivity than resistance or capacitance measurement is because the oscillating structure is generally more prone to a change in it's internal state than in it's external structure like deformation. In musical instruments, different musical notes are due to frequency variations caused by a suitable external force. The same amount of force hardly influences the length or thickness of the strings . The drawback of resonant pressure sensors is that frequency fluctuations can arise due to condensation, dust and corrosion. The energy loss can be measured by the quality factor of the response and as such it is desirable to have a high quality factor leading to higher precision and long term stability. Hence a sealed structure is required. Also for continuous monitoring of frequency, the suspended structure needs to be driven continuously as shown in Figure 1-7 and therefore excitation and detection of signals is more complex but mostly digital. Temperature and input DC bias dependance on frequency is yet another disadvantage.

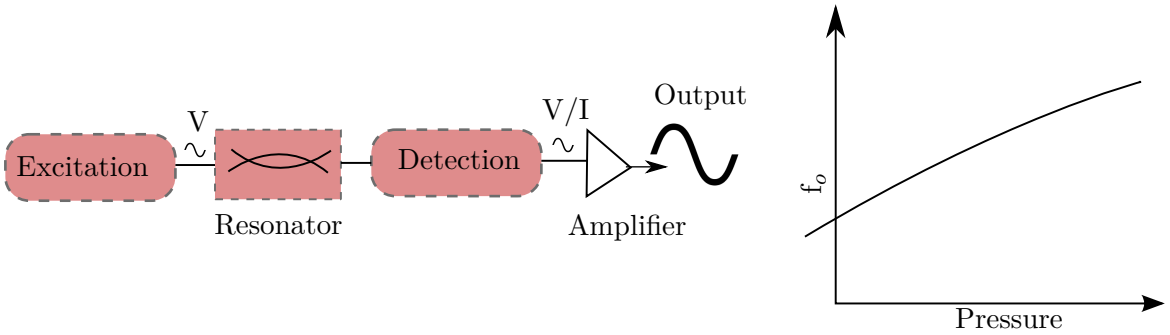

Figure 1-7: Block diagram for frequency readout of MEMS resonator. Different types of excitation and detection techniques can be used as mentioned in the next section.

1-3 Resonant Pressure Sensor : Past work from literature

Mechanical resonant frequency is inherently dependent on it's internal device parameters like stiffness, mass or shape. As such, the resonant frequency can be altered by either changing it's stiffness by application of force or pressure or by changing the mass. Added mass effect have been used to monitor thickness of thin films while shape effects have been extensively used as pressure sensors [22]. A second way for resonant device to act as pressure sensor is damping effect due to surrounding medium (fluid or gas) [23]. The quality factor which is the measure of damping can be used to describe the resonance behavior of the device. Compression forces from surrounding molecules are responsible for the shift in resonant frequency. This is known as squeeze-film damping and will be studied in details in Chapter 2 . Since the sensing element is usually a resonator subjected to change in shape or stiffness, many pressure sensors can be categorized based upon the resonator itself (Figure 1-9). Each resonator can also resonate in

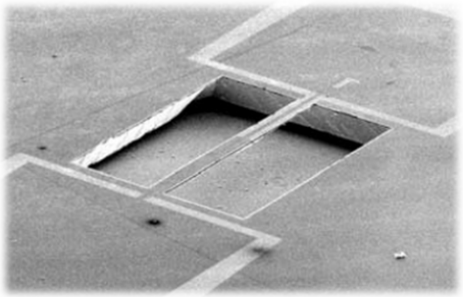

(a)

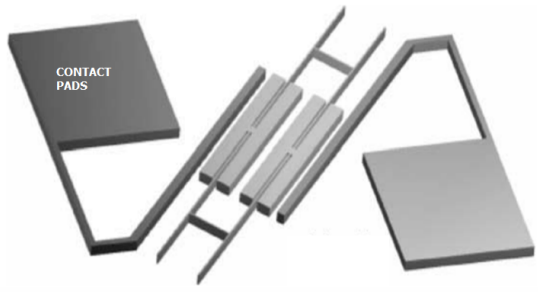

(b)

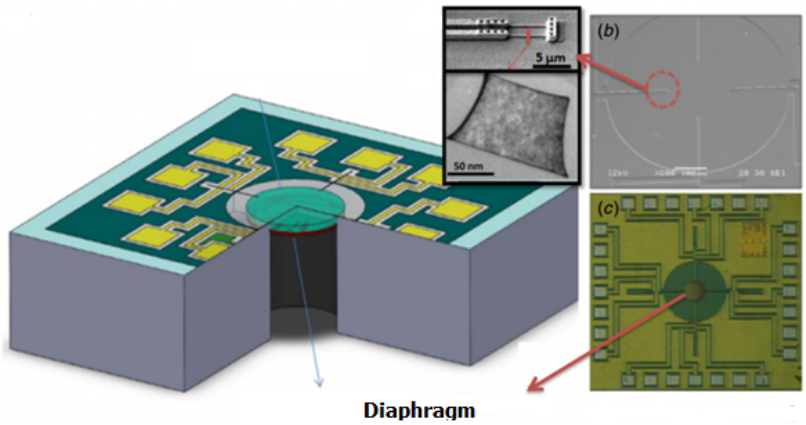

(c)

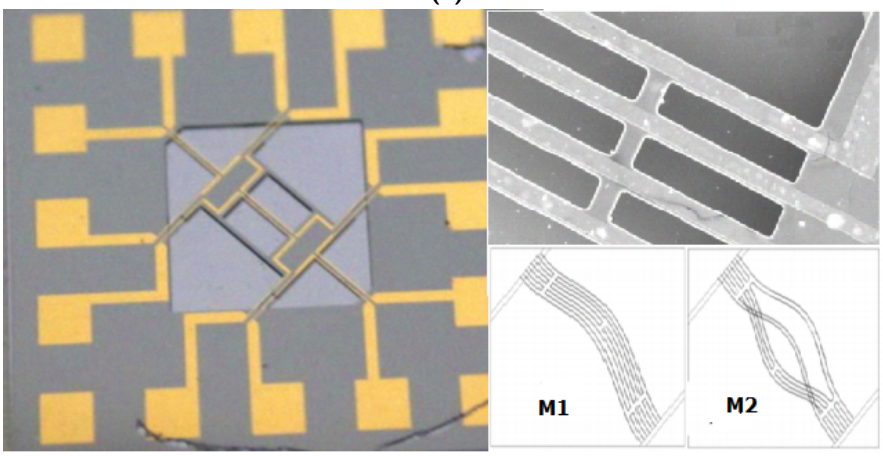

(d)

Figure 1-8: (a) SEM image of a single clamped beam resonator [24]. (b) Double ended tuning fork [25] with drive and sense metal pads. (c) Pressure sensor with a circular diaphrgam [5]. (d) A triple ended tuning fork for resonant pressure sensor [26] with two possible modes of resonance (M1 and M2).

different modes resulting in different deflection shape and resonant frequency. The beam for example has many degrees of freedom and can deflect in vertical (Flexural mode), horizontal (longitudinal mode) or both (torsional mode) directions. Complicated structures like double ended tuning fork (DETF), triple ended tuning fork (TETF) can vibrate in various other modes. Exciting the resonator into the desired mode and detecting the resonant frequency is an entirely a different way to characterize the wide range of pressure sensors available today. Five different ways of excitation and detection [27] are known today in the MEMS community, combinations of which have been used to fabricate various resonant sensors and are discussed below.

- **Electrostatic excitation** : This technique requires two electrodes out of which one of them acts as a vibrating element. An A.C. signal between the electrodes sets up electrostatic force against the damping caused by air setting the device into motion [28], [29], [22].
- **Piezoelectric excitation** : Since silicon is not a piezoelectric material, a layer of piezoelectric material like ZnO is deposited onto the device. On application of voltage signal, the stress induced by piezoelectricity sets the vibrations [30], [31].
- **Electrothermal excitation** :Also known as resistive heating [32], [33], [24] , this technique uses the heat pulse to excite the device. Integrated diffused resistors are used to create local material expansion resulting into material deflection.
- **Optical excitation** : Light beam typically from a laser source is focused on the resonator to generate thermal stress for excitation. The light can also be concentrated in a mirrored cavity to increase thermal stress [34].
- **Electromagnetic excitation** : Use of inductors or electromagnets for excitation of resonators fall under this category which uses the interaction between electrical current and magnetic field [35], [26], [36].
- **Capacitive detection** : Similar to electrostatic excitation, the two electrodes also constitutes a capacitor with changing gap distance. The change in capacitance (in the form of charge storage) is used to read out the deflections [28], [26] , [36].
- **Piezoelectric detection** : In this case, the deposited layer of piezoelectric material is used to read out the electrical signals from the charge generated by deflection of resonator due to the stress induced [30], [31].
- **Piezoresistive detection** : Since silicon is piezoresistive material, it is capable of changing its resistivity when subjected to stress which can be measured, a principle discussed in piezoresistive pressure sensors [32], [24], [29].
- **Electromagnetic detection** : The reverse operation of magnetic excitation where the vibration in a magnetic field generates an induced voltage which is then read-out to detect deflections [35].
- **Optical detection** : An optical arrangement can also be used to study the deflection of the membrane by measuring the reflected beam from the resonator. This can either be done by interferometric techniques (analysis of interference pattern) or amplitude

modulation (analysis of reflected beam's amplitude) [34], [37] . The experimental setup is however complex and need careful aligning of optics.

Table 1-1 summarizes "few" of the various pressure sensors till date and would give the reader an idea of all possible categories of sensor technology.

Table 1-1: Overview of past resonant pressure sensors-1990-2014

Year	Resonator	Excitation	Detection	Sensitivity	Ref.
2013	Diaphragm	Electrostatic	Capacitive	227 Hz/KPa	[28]
2012	Bridge	Electrothermal	Piezoresistive	1.8%/bar	[32]
2010	Beam	Electromagnetic	Electromagnetic	112Hz/kPa	[35]
2010	Diaphragm	Piezoelectric	piezoelectric	3.3Hz/kPa	[30]
2009	Beam	Electromagnetic	Capacitive	155Hz/kPa	[26]
2005	Diaphragm	Electrothermal	Optical	3kHz/kPa	[33]
2005	Beam	Electrothermal	Piezoresistive	27.4Hz/kPa	[24]
2003	Diaphragm	Electromagnetic	capacitive	9.6kHz/kPa	[36]
2001	Beam	Electrostatic	Optical	3.2%/bar	[37]
2000	DETF	Electrostatic	Piezoresistive	2.08 Hz/mbar	[29]
1997	TETF	Piezoelectric	piezoelectric	0.2 Hz/mbar	[31]
1992	Bridge	Optical	Optical	86%/bar	[34]
1990	Diaphragm	Electrostatic	Optical	19%/bar	[22]

1-4 Self-oscillating pressure sensor

In conventional presure sensors, most popular read-out circuits like switch capacitor circuits [38], transimpedance amplifiers [39] or ac bridges [40] translate the capacitive or resistive changes into analog signals. In addition to this, analog to digital converters maybe required for signal processing. The first drawback of these integrated systems is that the sensitivity of the sensor is influenced by the non-idealities of the read-out circuits such as thermal noise, 1/f noise or switch noise. Analog-to-Digital converter (ADC) also require large area which lead to increased power consumption and cost. One solution to the above problems is to use Capacitance-to-Frequency Converter (CFC) [41] which uses a Capacitance-to-Voltage Converter (CVC) followed by Voltage-to-Frequency Converter (VFC). Alternatively, the pressure sensor can be engaged with a Complementary Metal Oxide Semiconductor (CMOS) ring oscillator [42], the frequency output of which is effected by the capacitive or resistive changes as shown in Figure 1-9(a). The resolution of such a system is limited by the phase noise which can be improved at higher operational frequency but switching speed of transistors also places a limit on the frequency. As such it would be difficult to operate at higher frequencies with lower phase noise and superior performance.

Another approach for frequency readout without the need of additonal frequency converters or reference oscillators is to use the MEMS resonator in a feedback loop so as to a form a self-oscillating pressure sensor as shown in Figure 1-9(b). This is similar to designing a MEMS oscillator but for pressure sensing. This concept using MEMS oscillators have been

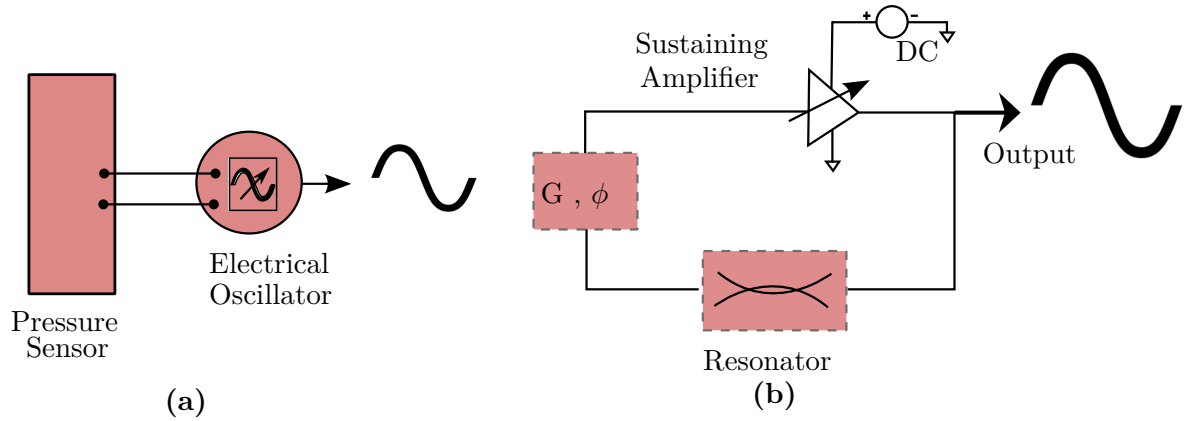

Figure 1-9: (a) Using a conventional pressure sensor in sync with an electrical oscillator with frequency output. (b) Block diagram for frequency readout of MEMS self-oscillating pressure sensor (adapted from [20]). G and ϕ are the gain and phase of the loop. This would be discussed in details in Chapter 3.

widely used for frequency references and timing applications [43] for digital circuits but there are also literature that justifies their use for mass sensing [44], temperature monitoring [45], gas sensing [46] and as such they also hold potential as pressure sensors. The concept will be discussed in more details in chapter 3.

1-5 Goal of Thesis

The research objective for this thesis is driven by the need to develop self-oscillating resonant pressure sensors for high performance over existing sensing technologies. Given the plethora of work done so far in resonant sensors, piezoresistive and capacitive pressure sensors are still the two most widely used technology proven to offer high sensitivity with good accuracy, temperature compensation and linearity. However, an adequate amount of signal conditioning followed by analog to digital conversion is required. Furthermore, integration of electrodes and piezoresistive films adds to the fabrication complexity. Since frequency read-out can be done with a higher resolution than conventional digital output signals (e.g. zero counting algorithms), resonant sensors are capable of giving high sensitivity and linearity. The output does not require signal conversion or additional frequency conversion blocks. The resonators however require continuous excitation and detection for frequency monitoring. The goal of this thesis is to characterize silicon MEMS devices as self oscillating resonant pressure sensors and to achieve higher sensitivity and resolution over the current existing sensors in the same or different category. The key parameters during the project work would be pressure resolution, sensitivity, noise, accuracy, time of measurement and power consumption. The aim is to develop a prototype as a proof of concept for future commercial applicability.

Since a frequency output signal is desired, we aim to design a MEMS oscillator whose output frequency is sensitive to applied/surrounding pressure and hence the experiments are carried out in a controlled pressure enviroment. Compared to conventional sensors, this also eliminates the requirement for hermetic sealing of the resonator. Based on different excitation and detection principles, we propose an opto-electronic MEMS oscillator using electrostatic

actuation and optical detection by Laser Doppler Vibrometry (LDV) which to our knowledge has not been reported in literature so far. Both optical feedback and sustaining amplification is provided by Laser Doppler Vibrometer which significantly reduces the complexity in the design of an oscillator. In addition to this, the non-contact optical readout eliminates problems with the parasitic capacitances. Design of an all-electrical MEMS oscillator can be considered as another thesis topic itself and due to time limitations, it is not covered in this report. To justify an all-electrical working prototype as an oscillating pressure sensor, quartz tuning fork will be used to implement both opto-electronic and an electronic oscillator topology and subsequently be compared on different key parameters mentioned earlier. The samples used in this thesis are pre-fabricated and a major part of the work is based on characterization, measurements and building of related electronic circuitry to develop the proposed sensor technology.

1-6 Outline of Thesis

- For the readers who have skipped the introduction part and have jumped to this section, the first chapter gave a quick overview about the current state of MEMS sensor technology and its potential in various applications. Of all the sensors, a general overview of four different kinds of pressure sensors (piezoresistive, capacitive, optical and resonant) were discussed briefly. Resonant pressure sensors have been discussed in further detail by summarizing the current existing technologies and past work done in this domain leading to a strong motivation for developing smart and efficient pressure sensing technology which gives us our goal for this thesis project - *An opto-electronic MEMS oscillator for resonant pressure sensing*.

- Chapter two will cover the fundamental concepts of MEMS resonators and its motion in response to excitation signals namely sinusoidal signal and white noise. Subsequent sections will consider the theory and explain the principle behind damping based pressure sensing. Of all the types of resonator structures mentioned in chapter one, circular membranes have been studied in more detail because of their relevance to the work performed in this report.

- Chapter three gives a brief introduction to MEMS oscillators and shows the practical implementation of the proposed opto-electronic MEMS oscillator with optical feedback through Laser Doppler Vibromtery (LDV). The detailed analysis on sensitivity, noise, accuracy and comparision to theoretical concepts mentioned in chapter two are also presented.

- Chapter four describes the practical implementation of tuning fork based opto-electronic oscillator and electronic oscillator. The two topologies are characterized under same pressure enviroment and their performance results are compared in order to obtain insight in the effect of the feedback mechanism on the sensor performance.

- Chapter five concludes the report with discussion on experimental results and the feasibility of the proposed technology for future commerical application. Possible recommendations for further improvement are also presented.

Chapter 2

Fundamentals : MEMS Resonator

A mechanical resonator is the key feature of all MEMS devices. Apart from having microscopic dimensions, they also achieve a much higher quality factors (Q) which allows them to be used for precise experiments. The motion of mechanical resonators is used for various sensing applications like force in the order of zeptonewtons [47], yoctogram mass detection [48], sub-attometer position sensitivity [49]. Recently these miniature sensors are pushing the limits of measurable quantities further down to their fundamental limits (quantum zero-point fluctuations [50] where they are restricted by the quantum fluctuations. This chapter will discuss the motion of a resonator under the influence of external force and how it can be used as a pressure sensor. Analysis of circular membrane as a mechanical resonator is also presented.

2-1 Motion of a resonator

We begin by studying the motion of a resonator in a linear regime (dynamics of non-linear resonator are considered out of scope for this chapter). In general, the resonator can exhibit a three dimensional motion each with it's own mode. For simplicity, we reduce the motion to a one dimensional displacement function. In time domain, motion of the resonator is governed by Newton's equation given by Eq. (2-1). The second order differential equation is also known as *Langevin equation*.

$$m\frac{d^2x(t)}{dt^2} + b\frac{dx(t)}{dt} + kx(t) = f(t) \tag{2-1}$$

where

m is mass of the system
b is damping coefficient
k is spring constant
$x(t)$ is time dependent displacement function
$f(t)$ is time dependent drive force

The presence of a damping term suggests that the motion of resonator would cease to exist with time unless otherwise there is a driving force to balance the loss of energy thereby sustaining the motion . As such, the system can be compared to a driven harmonic oscillator similar to a spring-mass system as shown in Figure 2-1. Drive force $f(t)$ is assumed to be harmonic and could represent any type of force due to acoustic, pressure, thermal excitation etc.

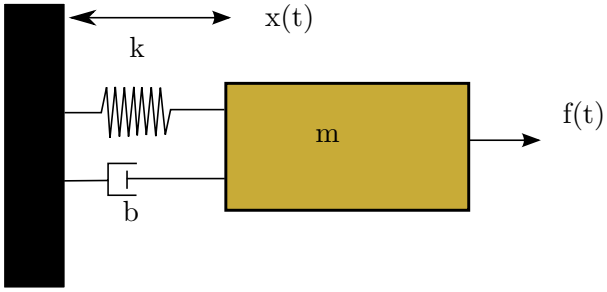

Figure 2-1: Spring-mass damper system describing the motion of a mechanical resonator.

In alternate form, Eq. (2-1) can be written as

$$\frac{d^2x(t)}{dt^2} + 2\zeta\omega_o\frac{dx(t)}{dt} + \omega_o^2 x(t) = \frac{F_o e^{i\omega t}}{m} \tag{2-2}$$

where

$$\omega_o = \sqrt{k/m} = \text{natural frequency of undamped oscillation}$$
$$\zeta = \text{damping factor}$$
$$F_o = \text{peak value of drive force}$$

We can expect the solution for the above equation to be in the form of $x(t) = X_o e^{\lambda t}$. Substiution of $x(t)$ in Eq. (2-2) gives us

$$\lambda^2 X_o e^{\lambda t} + 2\zeta\omega_o\lambda X_o e^{\lambda t} + \omega_o^2 X_o e^{\lambda t} = F_o e^{i\omega t}/m$$
$$[\lambda^2 + 2\zeta\omega_o\lambda + \omega_o^2]X_o e^{\lambda t} = F_o e^{i\omega t}/m$$

Since the number inside the bracket is independent of time, we can conclude that for both sides of the equation to be equal at all times, we must have $e^{\lambda t} = e^{i\omega t}$ or $\lambda = i\omega$. This means that the motion of a resonator is a complex function with the same frequency as the drive force. The complete solution for the displacement function is now given by Eq. (2-3).

$$x(t) = \frac{F_o e^{i\omega t}}{m(\omega_o^2 - \omega^2 + i2\zeta\omega_o\omega)} \tag{2-3}$$

Since $x(t)$ is a complex function of time and frequency, amplitude and phase of the displacement function can be written as

$$X_o(\omega) = \frac{F_o}{m\sqrt{(\omega_o^2 - \omega^2)^2 + (2\zeta\omega_o\omega)^2}} \tag{2-4}$$

$$\phi = tan^{-1}\left(\frac{2\zeta\omega_o\omega}{\omega_o^2 - \omega^2}\right) \tag{2-5}$$

2-2 Frequency response

The effect of frequency on the steady state displacement can be studied directly from Eq. (2-4) and Eq. (2-5). By appling Fourier transform, the steady state displacement can be represented as

$$X(\omega) = H(\omega)F(\omega) \tag{2-6}$$

where

$$H(\omega) = \frac{1}{m\sqrt{(\omega_o^2 - \omega^2)^2 + (2\zeta\omega_o\omega)^2}} \tag{2-7}$$

$H(\omega)$ is called as *magnification factor* which relates the magnitude of the force to magnitude of displacement. Eq. (2-7) can be sketched for various values of damping factors. We observe that at a frequency $\omega = \omega_o$, the denominator attains its minimum value and as such a large response is observed at ω_o. This is known as *resonance*. As seen from Figure 2-2, smaller the damping factor, higher is the amplitude response. Irrespective of damping conditions , it is seen that the response is in phase with the excitation at low frequencies i.e. $\omega << \omega_o$ and lags by 180 degrees at higher frequencies ($\omega >> \omega_o$) . The phase change is most dramatic near ω_o (Figure 2-2) at which the phase angle equals 90.

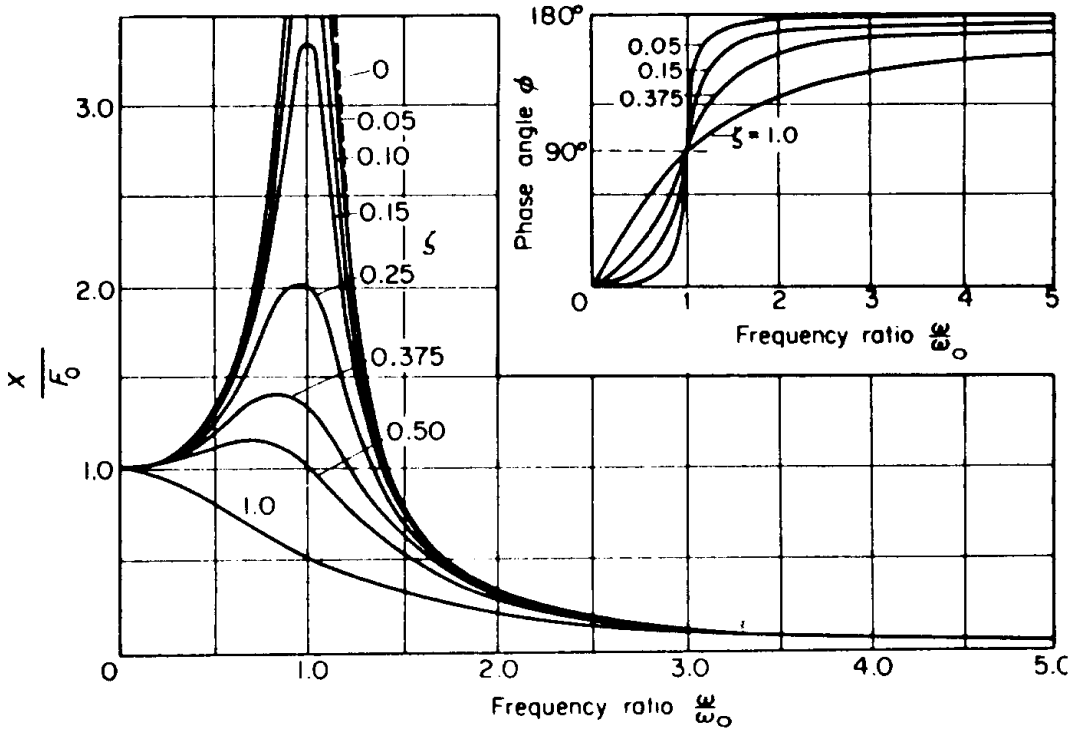

Figure 2-2: Amplitude and phase response as a function of frequency for different values of ζ.

The peak amplitude can also be characterized by the quality factor, a terminology adapted from electrical engineering which is defined as

$$Q = \frac{1}{2\zeta} = \frac{\sqrt{km}}{b} \tag{2-8}$$

Lower damping corresponds to a larger peak and hence a higher quality factor. For high Q systems ($Q > 10$), the response is approximately symmetrical for small variations in ω around ω_o. The amplitude falls to $1/\sqrt{2}$ of its peak value at $\omega_o(1 \pm \zeta)$. These frequencies are known as *half power or 3-dB frequency points* and the frequency band between these two points is known as the *bandwidth* of the system. The quality factor in terms of bandwidth can be represented as

$$Q = \frac{\omega_o}{\Delta\omega} \tag{2-9}$$

The forced displacement response can be found out for any excitation force by using Eq. (2-6). The response could be due to a deterministic signal or a random signal. Using the inverse Fourier transform, displacement function $x(t)$ can be determined.

2-2-1 Response due to deterministic signal

Most of the systems in practical cases are excited by a sinusoidal signal. As such we study the displacement response to an excitation force equal to $F_o sin(\omega_i t)$ where ω_i is the input drive frequency. Using Eq. (2-6), the inverse Fourier transform can be used to determine $x(t)$ according to the following relation

$$x(t) = \frac{1}{2\pi} \int_{-\infty}^{\infty} X(\omega) e^{i\omega t} d\omega \tag{2-10}$$

$$x(t) = \frac{1}{2\pi} \int_{-\infty}^{\infty} H(\omega) F(\omega) e^{i\omega t} d\omega \tag{2-11}$$

For a force $F_o sin(\omega_i t)$, the Fourier transform analysis gives us

$$F(\omega) = \frac{F_o}{2i}[\delta(\omega - \omega_i) + \delta(\omega + \omega_i)] \tag{2-12}$$

Combining Eq. (2-11) and Eq. (2-12), the displacement response is equal to

$$x(t) = \frac{F_o sin\omega_i t}{m\sqrt{(\omega_o^2 - \omega^2)^2 + (2\zeta\omega_o\omega)^2}} \tag{2-13}$$

The above equation can more easily be verified if we assume that the excitation force is equal to $\mathfrak{Re}(F_o e^{i\omega_i t})$. In that case the displacement is simply $\mathfrak{Re}(X_o e^{i\omega_i t})$ and is equal to Eq. (2-13) i.e. the displacement function is also sinusoidal in nature.

2-2-2 Response due to random signal

Unlike deterministic signals, the response to a mechanical system due to a random process cannot be defined explicitly as a function of time. The response function must be determined based on stochastic nature of random process or it's statistical properties. For many practical systems, observations are made over a period of time and under the influence of random effects, observed values are subjected to change with each instance of time. Random variables show

a normal distribution and hence random processes are usually Gaussian in nature. Any linear system subjected to a Gaussian force leads to a Gaussian response. In this section, we study the displacement response under white noise excitation. The white noise is defined as a stationary process since statistical properties found by averaging over a time-period are constant. White noise is defined for a constant power spectral density irrespective of it's signal bandwidth. Hence in order to study $x(t)$, we consider the driving force in the form of Power Spectral Density (PSD) which has units of power/Hz.
Let us consider a sample $f_n(t)$ and $f_n(t+\tau)$ from a random white noise signal separated by a time interval τ. The two samples can be related by auto-correlation function defined by

$$R(\tau) = \lim_{T\to\infty} \int_0^T f_n(t) f_n(t+\tau) dt \tag{2-14}$$

We can see that for $\tau = 0$, the auto-correlation function is reduced to mean square value of the process $f(t)$

$$R(0) = \overline{f_n(t)^2} \tag{2-15}$$

Frequency domain analysis of $f_n(t)$ therefore is best represented by Fourier transform of auto-correlation function and is also known as power spectral density function $S(\omega)$.

$$S(\omega) = \frac{1}{2\pi} \int_{-\infty}^{\infty} R(\tau) e^{i\omega\tau} d\tau \tag{2-16}$$

We can now evaluate the mean square value from it's power spectral density function by taking inverse Fourier transform of Eq. (2-16)

$$R(0) = \overline{f(t)^2} = \int_{-\infty}^{\infty} S(\omega) d\omega \tag{2-17}$$

Hence the mean square value of a random signal can be obtained by integrating its power spectral density over the entire frequency range. The spectral density of band-limited white noise is noted to be constant over the entire bandwidth for which the auto-correlation function mathematically can be written as [51]

$$R(\tau) = B_f S_o \frac{sin(\pi B_f \tau)}{\pi B_f \tau} cos(\omega_c \tau) \tag{2-18}$$

where

B_f=bandwidth
S_o=spectral density over the entire B_f
ω_c=center frequency

From Eq. (2-18), the mean squared value is equal to

$$\overline{f(t)^2} = R(0) = B_f S_o \tag{2-19}$$

Returning to Eq. (2-6), we find the displacement in it's spectral density form. Using Eq. (2-15) and Eq. (2-16), the displacement spectral density can be written as

$$S_x(\omega) = E[X(\omega) X^*(\omega)] \tag{2-20}$$

where $X^*(\omega)$ denotes the complex conjugate function and E denotes the average value.

$$S_x(\omega) = H(\omega)H^*(\omega)E[F(\omega)F^*(\omega)] \tag{2-21}$$

$$S_x(\omega) = |H(\omega)|^2 S_o \tag{2-22}$$

$$S_x(\omega) = \frac{S_o}{m[(\omega_o^2 - \omega^2)^2 + (2\zeta\omega_o\omega)^2]} \tag{2-23}$$

The above equation can be sketched as shown in Figure 2-3.

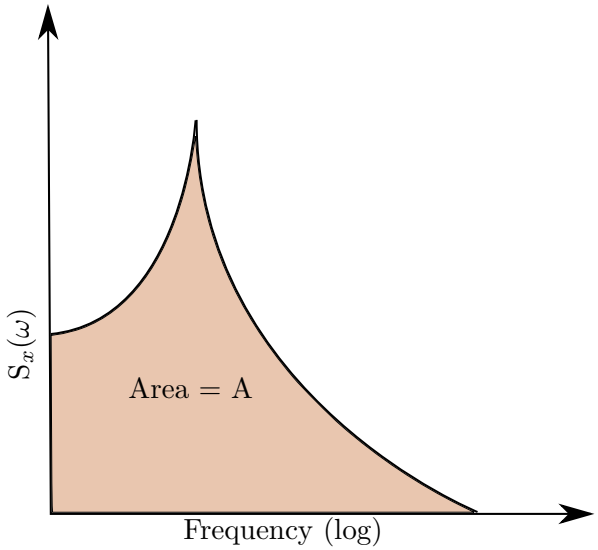

Figure 2-3: Displacement spectral density in response to band-limited white noise

Mean square displacement can be obtained by integrating $S_x(\omega)$ over the entire frequency range. In other words, area under the curve gives the mean square response as [51]

$$A = \overline{x(t)^2} = \frac{\pi f_o(1 + 4\zeta^2)S_o}{4\zeta} \tag{2-24}$$

Therefore the rms displacement response is

$$x_{rms} = \sqrt{\overline{x(t)^2}} \tag{2-25}$$

When a mechanical system is subjected to both white noise and sinusoidal signal, the respective power spectral density add up to determine the net displacement response. Further insight into displacement response for various excitations can be found in [51].

2-3 Q-Factor

The quality factor has been introduced in the previous section in terms of resonator's mechanical parameters. Since the quality factor is the measure of damping in the system, it is an indicative to the energy loss associated with the motion of the resonator. In a MEMS

resonator, excitation energy from the source is converted into mechanical energy. Within the resonator, energy is transformed from kinetic energy (motion) to potential energy (spring). This conversion leads to some energy loss. The quality factor of the system relates the energy lost mathematically as

$$Q = 2\pi \frac{energy\ stored\ in\ the\ resonator}{energy\ dissipated\ per\ cycle} \tag{2-26}$$

The high quality factor corresponds to lower energy losses which is advantageous. Low energy loss means that the system needs less energy to sustain oscillation which reduces power consumption and thermal stress. A high Q means that the resonator has excellent material properties and long term stability. In general, three major different loss mechanism exists which leads to lowering of quality factor.

- **Air/Gas damping**: The energy loss in the resonator which operate in air or gas chamber is related to the surrounding pressure. Depending on the magnitude of surrounding pressure, different loss mechanism are observed as tabulated in Table 3-1[52].

Table 2-1: Pressure dependance on Q-factor

Region	pressure	Loss mechanism Excitation	Q
Intrinsic	low	Negligible damping Q attains its maximum value at vacuum	high
Molecular	Intermediate	Damping due to independent collisions of gas molecules with the resonator	medium
Viscous	atmospheric	Air acts as fluid Damping due to viscous drag	low

- **Support losses**: Energy can be lost at the mounting points due to the motion of resonator because of moments and shear force acting at these points. These losses can be minimized by balanced resonator structures which cancel out the forces or by the use of mechanical filters like spring-mass systems [53].
- **Intrinsic damping**: Resonator also dissipates energy due to intrinsic material losses like internal friction, magnetic fields, atom restructuring (grain boundaries) etc. These losses are usually small but can become significant in a very high Q system.

For each loss mechanism, a Q-factor can be determined. The overall Q factor is given by the expression

$$\frac{1}{Q} = \frac{1}{Q_{air}} + \frac{1}{Q_{support}} + \frac{1}{Q_{intrinsic}} + ... \tag{2-27}$$

Air damping is the dominant loss mechanism. Resonators moving under viscous region (atmospheric pressure) experience high viscous drag. This phenomena where the air is pushed through a narrow channel like the volume between 2 closely spaced plates, is known as *squeeze film damping* which not only lowers the Q but also shifts the resonant frequency as discussed in next section.

2-4 Squeeze film damping

The traditional approach for resonant sensing is to increase the system's Q. This is achieved by reducing the damping effects of air by placing the system in vacuum or in a tightly sealed air cavity. Quality factor as high as 150,000 have been reported in early sensors [54] and many similar sensors are still fabricated now and then. For low Q systems (<100), resonant sensors are based on an entirely different approach which takes into account the effect of air/gas damping also known as *squeeze film damping* [55]. Andrew *et al.* reported the effect on the resonant frequency of micro-structures due to surrounding air pressure. The gas confined between two closely spaced plates results in compressive forces due to the motion of electrodes. At higher frequency of oscillations, the gas is unable to escape the cavity and hence this adds to the stiffness of the structure thereby increasing it's resonant frequency. This is illustrated in Figure 2-4. In this section, we consider air/gas as a fluid and predict it's effects on properties of the resonator.

Many different theoretical approaches have been taken into consideration to study squeeze

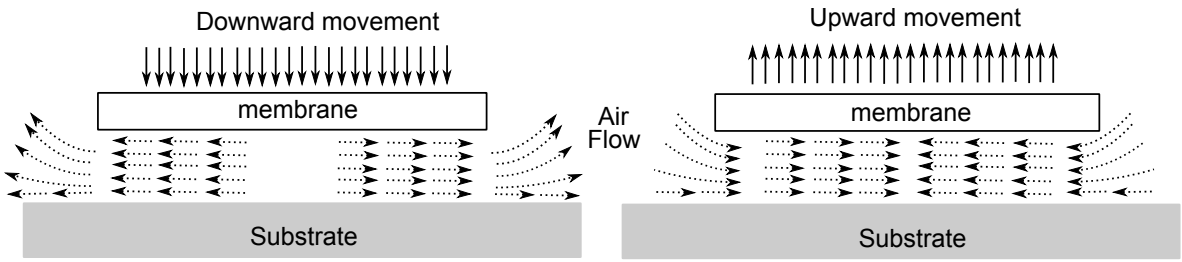

Figure 2-4: A schematic diagram of squeeze film air flow for downward and upward normal motion of the membrane.

film damping. One of the important model to consider is the fluid dynamics model based on compressible gas-film Reynolds equation by Blech [56]. When the air spacing within the resonator is reduced due to downward deflection of structure, net volume for the gas molecules decreases resulting in an increase in the density of particles. This can be seen as an increased number of collisions between the resonator and the gas molecules. In an alternate picture, the pressure distribution has two components. An in-phase component where the fluid film acts as a spring and merely acts as an extra contribution to the spring constant of the resonator and an out-of phase component but in phase with the squeeze velocity thereby acting as a damper. As such, we can now introduce the effective spring constant and damping coefficient as follows

$$k_{eff} = k + k_{squeeze} \tag{2-28}$$

$$b_{eff} = b + b_{squeeze} \tag{2-29}$$

The net displacment response of the resonator can now be modified as

$$m\frac{d^2x(t)}{dt^2} + (b + b_{squeeze})\frac{dx(t)}{dt} + (k + k_{squeeze})x(t) = f(t) \tag{2-30}$$

where

$$\omega_o'^2 = \left(\frac{k + k_{squeeze}}{m}\right) = \omega_o^2 + \frac{k_{squeeze}}{m} \tag{2-31}$$

The above equation clearly suggests that the resonance frequency is related to squeeze film damping due to the term $k_{squeeze}$. For determining the squeeze parameters, extensive research has been done to predict different loss mechanisms in the presence of air damping. It has been observed that the interaction between gas molecules and the membrane is different at different value of pressure [57] and as such different regimes of operation exsits. The parameter that defines the operating regime is known as Knudsen number K_n [58] which is defined as the ratio of the mean free path of the air molecule to the characteristic length of the air flow (air gap). Based on the value of K_n, different regimes have been identified and explored with their unique theoretical model as shown in Table 2-2.

Table 2-2: Different regimes of gas molecule behaviour

Regime	Theoretical Approach	K_n
Continuum regime	Navier stokes Equation with no slip boundry conditions	$K_n < 10^{-3}$
Slip regime	Navier stokes Equation with slip boundry conditions	$10^{-3} < K_n < 10^{-1}$
Transistion regime	Molecular approach	$10^{-1} < K_n < 10$
Molecular regime	Molecular approach	$K_n > 10$

At atmospheric pressure, the mean free path of gas molecules is around 68 nm. For a air gap of 1 μm, the device behaves in the continuum regime with viscous damping as a dominant loss mechanism. The squeeze film damping based on Navier-stokes equation [59] given by Eq. (2-32) can be used to extract squeeze parameters $b_{squeeze}$ and $k_{squeeze}$.

$$12\mu\frac{\partial(pg)}{\partial t} = \nabla.[(1+6K_n)g^3p\nabla p] \tag{2-32}$$

where

p=pressure
μ=coefficient of viscosity
g=thickness of the air gap

Many equations have been formulated to compute the damping coefficient in the past. In our case, we use circular diaphragms as resonators for which [59]

$$b_{squeeze} = \frac{3}{2\pi g^3}\mu A^2 \tag{2-33}$$

where A=area of the circular membrane. Since air/viscous damping is the dominant source of loss in this regime, most MEMS resonators are perforated with single or multiple holes to allow the flow of air through the membrane which reduces the effective damping. A simple modification to Eq. (2-33) including the effect of perforations was given by Skvor [60]

$$b_{squeeze}^{withhole} = \frac{12\mu\pi N r^4}{g^3}\left(\frac{1}{4}ln\frac{r^2}{r_h^2} + \frac{1}{2}\frac{r_h^2}{r^2} - \frac{1}{8}\frac{r_h^4}{r^4} - \frac{3}{8}\right) \tag{2-34}$$

where

r=radius of the membrane

N=number of holes
r_h=radius of the perforation

Skvor's model ignores the damping due to the air flow through the perforations and hence it underestimates the damping parameter. For N=1 and and large enough r_g, the damping resistance due to the hole can be ignored . In such a case, Eq. (2-33) or Eq. (2-34) can be both used for a good estimation of $b_{squeeze}$. If the gap dimensions are comparable to the mean free path of the molecules, then the slip flow model between the gas and the solid walls needs to be taken into consideration. Veijola has proposed the substitution of effective viscosity coefficient instead of μ given by [61].

$$\mu_{eff} = \frac{\mu}{1 + 9.638K_n^{1.159}} \tag{2-35}$$

A more accurate model for circular membrane with a single hole have been covered by various authors, a detailed discussion of which can be found in [62] and is considered out of the scope of this report. Bao's analytical model [63] also predicts the squeeze parameters based on diffusion time τ_d for molecular diffusion which is required to equalize the pressure inside and outside the air gap.

$$b_{squeeze} = \frac{pA\tau_d}{g}\left(\frac{1}{1+(\omega\tau_d)^2}\right) \tag{2-36}$$

$$k_{squeeze} = \frac{pA}{g}\left(\frac{(\omega\tau_d)^2}{1+(\omega\tau_d)^2}\right) \tag{2-37}$$

For high frequency oscillations $\omega >> 1/\tau_d$, the diffusion cannot respond quickly and we expect the squeeze film to only influence the spring constant. For low frequencies $\omega << 1/\tau_d$, we however observe extra damping. A detailed analytical model for above analysis can be found in [64]. Since $k_{squeeze}$ is directly proportional to the pressure, we expect an increase in resonant frequency with increasing pressure according to Eq. (2-31). A typical frequency response due to squeeze film damping is shown in Figure 2-5.

2-5 Electrical model for mechanical resonator

Sensors of any kind discussed so far can be treated as electromechanical transducers which convert mechanical (or acoustical) energy into electrical energy and vice-versa. For example, in case of electrothermal excitation discussed earlier; the electrical input power across the diffused resistors is converted into heat (thermal energy) which finally transforms into mechanical displacements. The generated deflections are next converted into an electrical output signal to transduce several physical variables like force, pressure, mass etc. Based on the structural properties of resonator and boundary conditions, the behavior of mechanical resonators can be described by Eq. (2-1). However, a much deeper, easier and quick insight can be obtained into the dynamics of sensors by an electrical equivalent model in which both electrical and mechanical parameters of sensors are represented by lumped-element electric circuit. The approach is based on the analogy between electrical and mechanical domain in Table 3-2 . The electrical equivalent can be easily solved by Kirchoff's Voltage Law (KVL),

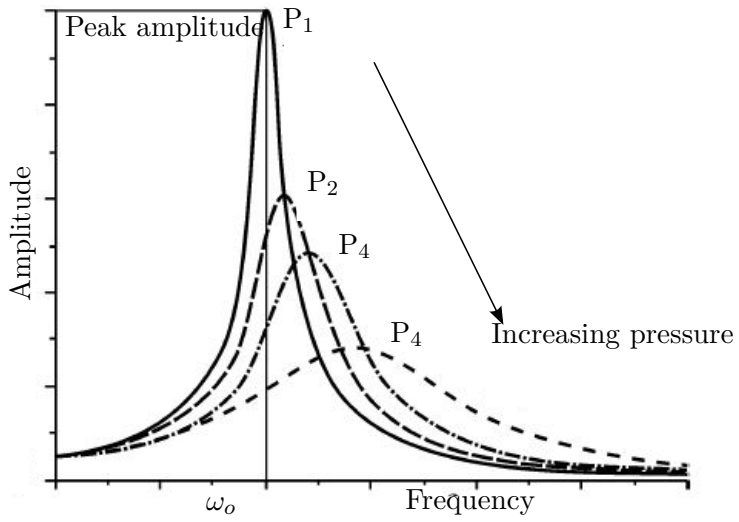

Figure 2-5: Frequency response of a resonator due to squeeze film damping. The resonance frequency increases with increasing pressure but with increased damping as shown (Adapted from [64]).

Kirchoff's Current Law (KCL) etc. which intrinsically solves variables like mass, stiffness or damping for many different domains. We begin by considering the electromechanical coupling

Table 2-3: Relation between electrical and mechanical domain

General	Electrical	Mechanical
Effort	Voltage-V	Force-F
Flow	Current-I	Velocity-v
Displacement	Charge-q	Deflection-x
Energy loss	Resistance-R	Damping-b
Energy Storage	Capacitor-C	Spring Constant-k
	Inductor-L	Mass-m

coefficient η between the efforts in the two domains. The coupling coefficient is a numerical measure of the conversion efficiency between electrical and mechanical energy. For the efforts F and V, we may write

$$F(t) = \eta V(t) \tag{2-38}$$

From the conservation of energy, we have

$$P_{mech} = P_{elec} \tag{2-39}$$

$$F(t).v(t) = V(t).I(t) \tag{2-40}$$

$$F(t)\left(\frac{dx(t)}{dt}\right) = \frac{V(t)^2}{Z} \tag{2-41}$$

where Z is the electrical impedance of the mechanical resonator. Using $V(t) = V_o e^{i\omega t}$, Eq. (2-3) in Eq. (2-38), we obtain

$$\frac{i\omega F_o^2 e^{2i\omega t}}{m(\omega_o^2 - \omega^2 + i2\zeta\omega_o\omega)} = \frac{V_o^2 e^{2i\omega t}}{Z} \tag{2-42}$$

or

$$Z = \frac{m(\omega_o^2 - \omega^2 + i2\zeta\omega_o\omega)}{i\omega\eta^2} \tag{2-43}$$

$$Z = \frac{1}{\eta^2}(2\zeta\omega_o m + i\omega m + \frac{m\omega_o^2}{i\omega}) \tag{2-44}$$

The above electrical impedance is similar to a series RLC circuit for which the input impedance is defined as

$$Z = R + j\omega L + \frac{1}{j\omega C} \tag{2-45}$$

Comparing the above two equations, we can finally determine the electrical model of a mechanical resonator in terms of R, L and C where

$$R_m = \frac{2\zeta\omega_o m}{\eta^2} = \frac{b}{\eta^2} = \frac{\sqrt{km}}{\eta^2 Q} \tag{2-46}$$

$$L_m = \frac{m}{\eta^2} \tag{2-47}$$

$$C_m = \frac{\eta^2}{k} \tag{2-48}$$

The subscript m stands for motional component of resonator. From Table 2-3 we can see that spring constant correlates to capacitance and mass to inductance. The complete electrical equivalent of the mechanical system is shown in Figure 2-6 where C_o is the shunt capacitor formed by the two electrodes separated by an air gap. From the analysis above, we can now formulate Q and ω_o as

$$\omega_o = \frac{1}{\sqrt{L_m C_m}} \tag{2-49}$$

$$Q = \frac{\omega L_m}{R_m} \tag{2-50}$$

2-6 Analytical theory of circular resonators

Circular membranes have been used in a number of experiments with various resonance mode (Figure 2-7) and shapes (ring or disk) as MEMS sensors. Circular plates are capable of both in-plane and out-of-plane vibrations. The membrane deflects in response to external force/pressure and resonates at it's mechanical frequency. Assuming that a solid circular plate clamped all around it's edge has a uniform thickness, the mechanical resonant frequency can be obtained from analytical plate theory [65] which takes into consideration the boundary conditions and Bessel functions corresponding to the in-plane and out-of plane forces. The natural frequencies for different modes is given by [66]

$$\omega_o = K_n\sqrt{\frac{D}{\rho h r^4}} \tag{2-51}$$

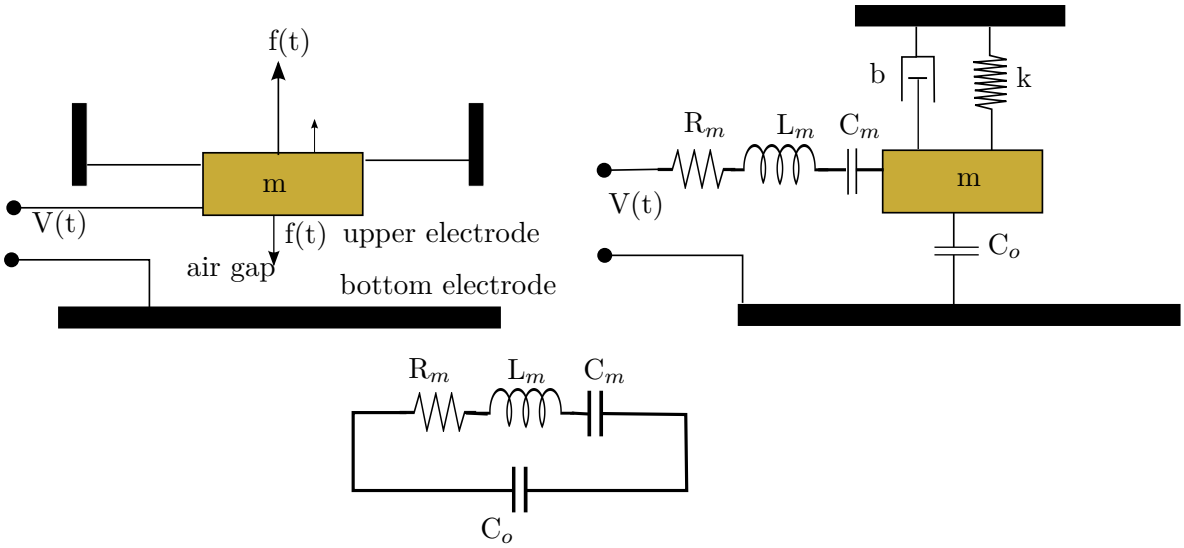

Figure 2-6: Electrical Equivalent of a mechanical resonator. The air gap between the two electrodes represents a capacitor with a parallel plate geometry.

where

K_n is constant where n refers to mode of vibration
h is membrane thickness
r is radius of the membrane
ρ is density of material
D is material's flexural rigidity given by

$$D = \frac{Eh^3}{12(1-\nu^2)} \tag{2-52}$$

where

E is Materials Young modulus
ν is Poisson ratio

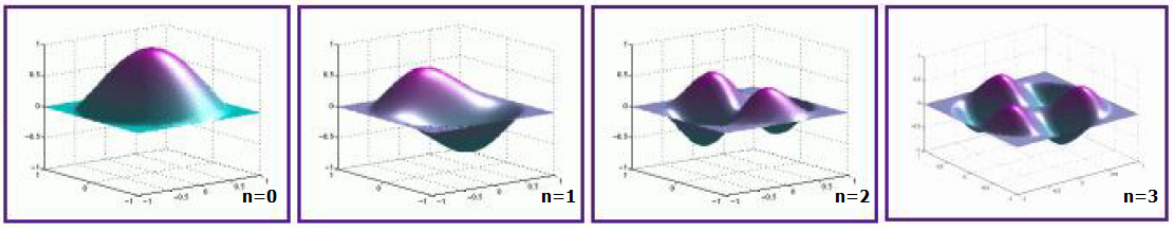

Figure 2-7: Different possible modes of normal (out-of-plane) vibration modes for a solid circular plate (adapted from [67]).

and therefore Eq. (2-51) reduces to

$$\omega_o = \frac{K_n h}{r^2}\sqrt{\frac{E}{12\rho(1-\nu^2)}} \tag{2-53}$$

It should be mentioned here that the the above mentioned frequency is the natural resonance frequency in case of absense of damping. However, for modeling squeeze film damping, we use the damped resonance frequency given by

$$\omega_d = \omega_o\sqrt{1-\left(\frac{1}{2Q}\right)^2} \tag{2-54}$$

Similar theories can be applied to circular membranes with bimetallic layers with same or different values of Poisson's ratio (ν_1, ν_2) and rigidity (E_1, E_2). For a case where these parameters differ by significant amount, we use equivalent values of D_e and ν_e given by [68]

$$D_e = \frac{E_1 h_1^3}{12(1-\nu_1^2)}K_a \tag{2-55}$$

$$\nu_e = \nu_1\frac{K_b}{K_a} \tag{2-56}$$

where

$$K_a = 1 + \frac{E_2 h_2^3(1-\nu_1^2)}{E_1 h_1^3(1-\nu_2^2)} + \frac{3(1-\nu_1^2)(1+h_2/h_1)^2(1+E_1h_1/E_2h_2)}{(1+E_1h_1/E_2h_2)^2-(\nu_1+\nu_2E_1h_1/E_2h_2)^2} \tag{2-57}$$

$$K_b = 1 + \frac{\nu_2 E_2 h_2^3(1-\nu_1^2)}{\nu_1 E_1 h_1^3(1-\nu_2^2)} + \frac{3(1-\nu_1^2)(1+h_2/h_1)^2(1+\nu_1E_1h_1/\nu_2E_2h_2)}{(1+E_1h_1/E_2h_2)^2-(\nu_1+\nu_2E_1h_1/E_2h_2)^2} \tag{2-58}$$

When the membrane is deflected by a uniform external pressure p_{ext}, it also experiences an additional electrostatic force during electrostatic actuation. The total pressure is thereby given by

$$p_o = p_{ext} + \frac{F(t)}{\pi r^2} \tag{2-59}$$

and the plate's deflection at a radial distance r_x from the center can be written as [66]

$$x(r_x) = \frac{p_o r^4}{64 D_e}\left(1-\frac{r_x^2}{r^2}\right)^2 \tag{2-60}$$

The equation of the plate's deflection for a uniform pressure is assumed to hold for all stable deflections. This assumption can be used to determine the equivalent mechanical parameters and predicts its plate displacement as a function of applied voltage which will be discussed in more details in Chapter 3. In [69], a similar analyis has been done to extract mechanical parameters i.e. m, k, and Q for circular membranes.

Chapter 3

MEMS oscillator as resonant pressure sensor

Every resonant sensor requires continuous excitation of MEMS resonator for regular monitoring of resonant frequency as a function of measurand (pressure, mass or force). The resonator can be brought into vibration and mode or frequency can be readout by various excitation and detection techniques as discussed in chapter 1. The detection block typically consist of an interface circuit which converts the measurand dependent variables like capacitive or resistive changes into analog signals via current/charge sensing circuits which are then fed to impedance or dynamic signal analyzer for data acquisition. Such sensors can be configured in either open-loop [70] or closed-loop [71] (using a phase lock loop-PLL [32]) configuration as shown in Figure 3-1. Conventional resonant sensors use hermetic sealing to achieve high Q factors.

For very small pressure fluctuations, detected output signals are too small in magnitude and therefore require additional amplification to achieve high Signal-to-Noise Ratio (SNR). For piezoresitive or capacitive pressure sensors, the outputs are analog in nature and hence sensitive to noise. With a view to have digitally encoded output signals, several pressure sensors with frequency output have been proposed [72], [73], [74]. It is easier and convenient to conduct frequency measurements with digital circuits. In [72], piezoresistive pressure sensors have been integrated with ring oscillators, the output frequency of which is controlled by pressure. The change in the resistivity of silicon causes a change in the injection current in the transistors and hence modulating the frequency output of the ring oscillator. A similar principle has been used in capacitive pressure sensors [75]. These resonant sensors use an external electrical oscillator whose frequency accuracy limits the sensor's sensitivity. High accuracy can be obtained from low noise injection, high quality factors and low temperature drift. In terms of these parameters, emerging class of MEMS based mechanical oscillators provides superior electrical performance over electrical oscillators [76]. In [77], stability of electrical oscillators have been improved by locking them with mechanical oscillators. Due to these reasons, MEMS oscillators have been replacing electrical and highly sensitivity quartz oscillator for frequency references and timing applications [43] as well as for resonant sensing

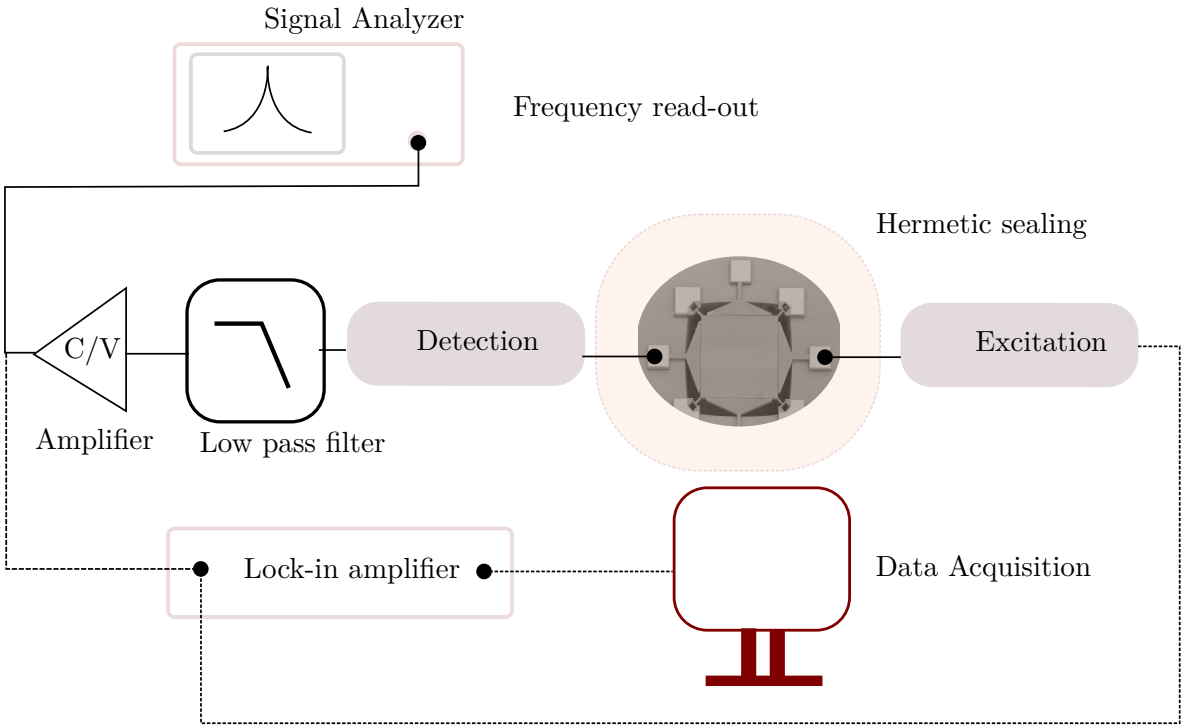

Figure 3-1: Open loop and closed loop (dash line) characterization of resonant sensors.

applications with frequency output signal. One of the main advantages of MEMS devices is their capability to be integrated with current CMOS technology. As such, potential of MEMS oscillators have been explored for measuring displacement [78], mass in attogram range [44], magnetic field [79], acceleration [80] and even molecular interactions. Same principle of self-exciting MEMS oscillators have been used for pressure sensing [81] which combines the features of conventional resonant sensors along with excellent mechanical and electrical performance of MEMS devices.

3-1 MEMS oscillator

For a theoretical case of a lossless system ($Q = \infty$), the resonator would oscillate indefinitely once excited. However, for a finite Q system, the oscillations would cease to exist after certain amount of time due to inherent energy losses. In general, sustained oscillations can be obtained by using a MEMS resonator in a closed loop as shown in Figure 3-2 . The resonator can be considered as a frequency dependent non-linear block with a transfer function $G(\omega, A)$. For a system to oscillate at a frequency ω_{osc}, the two following conditions need to be true.

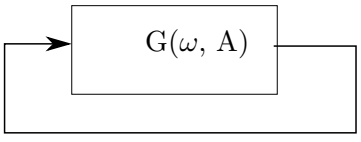

Figure 3-2: A general model for an oscillator.

$$\mathfrak{Re}G(\omega_{osc}, A_{osc}) = 1 \tag{3-1}$$

$$\mathfrak{Im}G(\omega_{osc}, A_{osc}) = 0 \tag{3-2}$$

Eq. (3-2) implies that the total phase of the closed system should be a multiple of 360^0. These conditions are known as barkhausen criteria [82] and are only true under two satisfying conditions [83].

$$\left(\frac{d(argG)}{d\omega}\right)_{\omega_{osc},A_{osc}} < 0 \tag{3-3}$$

$$\left(\frac{|G|}{d\omega}\right)_{\omega_{osc},A_{osc}} < 0 \tag{3-4}$$

Eq. (3-3) is known as phase stability which states that if the phase loop increases, then frequency must decrease. No periodic oscillation can take place if this condition is not satisfied. Eq. (3-4) is known as amplitude stability i.e. the amplitude decreases whenever loop gain increases. As such some non-linearity is required in the circuit for fixing the signal amplitude. For sustained oscillations, the energy loss is compensated by an additional sustaining amplifier which contributes to the total loop gain of the system. Figure 3-3 shows a block diagram of a MEMS oscillator.

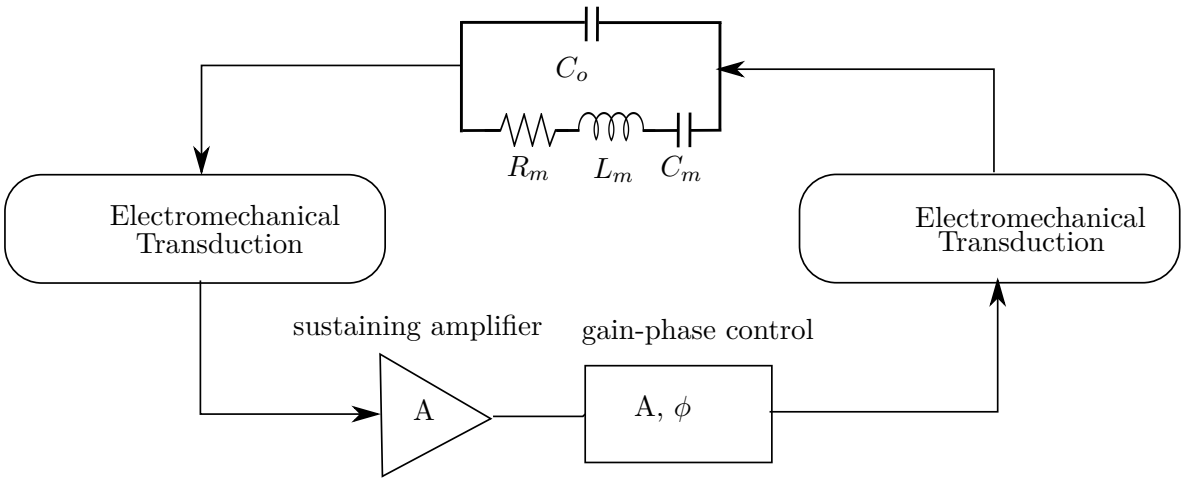

Figure 3-3: Closed loop system of MEMS oscillator. Total loop gain is dependent on all individual blocks.

Depending upon the application or resonator structure, some transduction mechanisms for excitation and detection are preferred over others. For example, electrostatic excitation requires two parallel electrodes (the resonator being the upper electrode). In case of large static deflections due to DC bias, the force distribution is disturbed and can be solved by redesigning the resonator. In fact geometric shaping of resonators for every transduction mechanism is possible [84] to control the desired mode of excitation. Piezoelectric and piezoresistive transduction requires integration of additional layers/components to the resonator and leads to increased complexity during fabrication. Mechanism involving thermal stress lead to temperature drift in the system thereby reducing the accuracy. In such cases, contact-less interrogation like optical or electromagnetic principles seems a better option. While EM transduction requires

close proximity to large magnetic coils, optical systems need large experimental setup and intricate alignment of optics in presence of thermal drift and vibrations. Electrostatic actuation by far is the most common approach and offers the simplest excitation mechanism for MEMS oscillator. This chapter leads to a design of a MEMS oscillator with electrostatic excitation and optical detection by using highly sensitive laser doppler vibrometry (discussed later) which to our knowledge has not been reported so far. The advantages offered by optical feedback will be discussed in the subsequent sections.

3-2 Electrostatic excitation

Consider a resonator geometry as shown in Figure 3-4 excited by a voltage source $V = V_{dc} + V_{ac}$. We assume the plates are supported elastically, so they don't collapse. The charge q induced across the plates generates an electric field $\vec{E}$ between the electrodes resulting in an electrostatic force. Since the bottom electrode is fixed, the upper electrode (the resonator) is set into vibration with a displacement x.

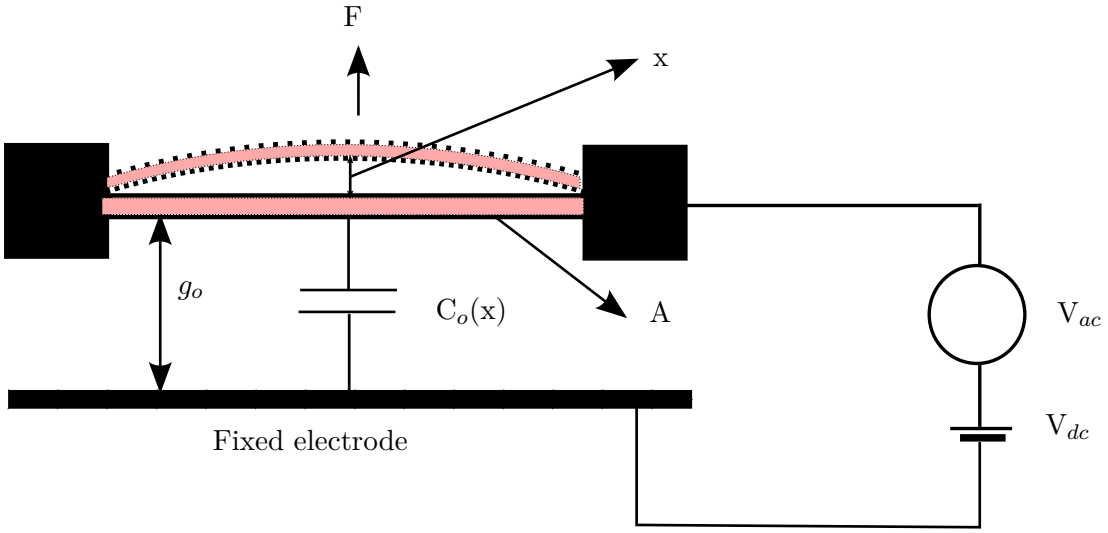

Figure 3-4: Electrostatic excitation of a parallel plate resonator.

Statistically, the driving force should be compensate by the restoring force kx due to the spring for any value of x.Using the well known equations, the generated force is equal to

$$F = q\vec{E} = C_o(x)V\left(\frac{V}{g_o \pm x}\right) \tag{3-5}$$

$$C_o(x) = \frac{\epsilon_o A}{g_o \pm x} \tag{3-6}$$

where A is the area of electrode, ϵ_o is permiivity of air, g_o is static air gap between 2 electrodes. The plus and the minus sign denotes the upward and downward deflection of the membrane thereby modulating the gap capacitance. For any small variations in the input voltage around it's DC value, the corresponding change in force is given by

$$dF = \frac{2\epsilon_o AV}{(g_o \pm x)^2}dV \tag{3-7}$$

which leads to a displacement dx. Alternatively, electrostatic force can be summed up as

$$F = \frac{d\vec{E}}{dx} \tag{3-8}$$

The energy stored in the capacitor as a function of displacement can be written as

$$E = \frac{1}{2}C_o(x)V^2 = \frac{1}{2}\left(\frac{\epsilon_o A}{g_o \pm x}\right)V^2 \tag{3-9}$$

For an input voltage $V = V_{dc} + V_{ac}sin(\omega_i t)$, Eq. (3-9) reduces to

$$F = \left(\frac{\epsilon_o A V_{dc}}{(g_o \pm x)^2}\right)V_{ac} \tag{3-10}$$

The term V_{dc}^2 is a steady term and does not contribute to the driving force. Neglecting the small contribution due to V_{ac}^2 leads to Eq. (3-10). This equation is similar to Eq. (2-38) which gives a mathematical expression for coupling coefficient η.

$$\eta = \frac{\epsilon_o A V_{dc}}{(g_o \pm x)^2} \approx \frac{\epsilon_o A V_{dc}}{{g_o}^2} \tag{3-11}$$

The coupling factor η from Eq. (3-11) indicates the conversion efficiency between input signal V_{ac} to mechanical force F. To increase this factor, we must either increase the area of electrode i.e. increase the size of the resonator or decrease the air gap g_o. The same effect can also be obtained by increasing V_{dc}. However, increasing the DC bias voltage also tunes the resonant frequency . This can be seen if we consider the quadratic dependence of x on driving force due to the denominator $(g_o - x)^2$ in Eq. (3-10). Taylor expansion results in higher order terms suggesting that it is a non-linear spring known as amplitude stiffened duffing spring . Depending on the sign, this additional spring constant k_{elec} can either increase or decrease the resonant frequency; also known as hardening or softening effect respectively [85]. For parallel plate geometries, "soft" spring effect is seen due to cubic dependence on displacement [86]. Complete analysis of induced non-linearity results in [87]

$$\frac{\nabla f}{f_o} \approx -\frac{V_{dc}^2 \epsilon_o A}{2k g_o^3} \tag{3-12}$$

Since frequency shift has a square dependence on DC bias, highly stable DC source are required. From Eq. (2-46)-Eq. (2-48), we also notice the square dependence of V_{dc} on the electrical lumped parameters.

3-3 Electrical Measurement : Open-loop characterization

For our experiments we use a MEMS diaphragm with a center perforation to keep the pressure equal on both sides of the oscillating membrane. The cross-sectional view of the resonator is shown in Figure 3-5 and Table 3-1 lists the device specification.

We perform an open loop characterization of the MEMS resonator using a **HP 4194A impedance/phase analyzer**. The resonator is excited by a **200 mV AC** signal (pk-pk) with a variable DC bias. The input impedance is measured over a suitable frequency range. The resonator was hermetically sealed and connected to a vacuum pump (**Petiffer-D35614 A**) to regulate internal pressure inside the cavity. The device was characterized for different values of pressure and DC bias.

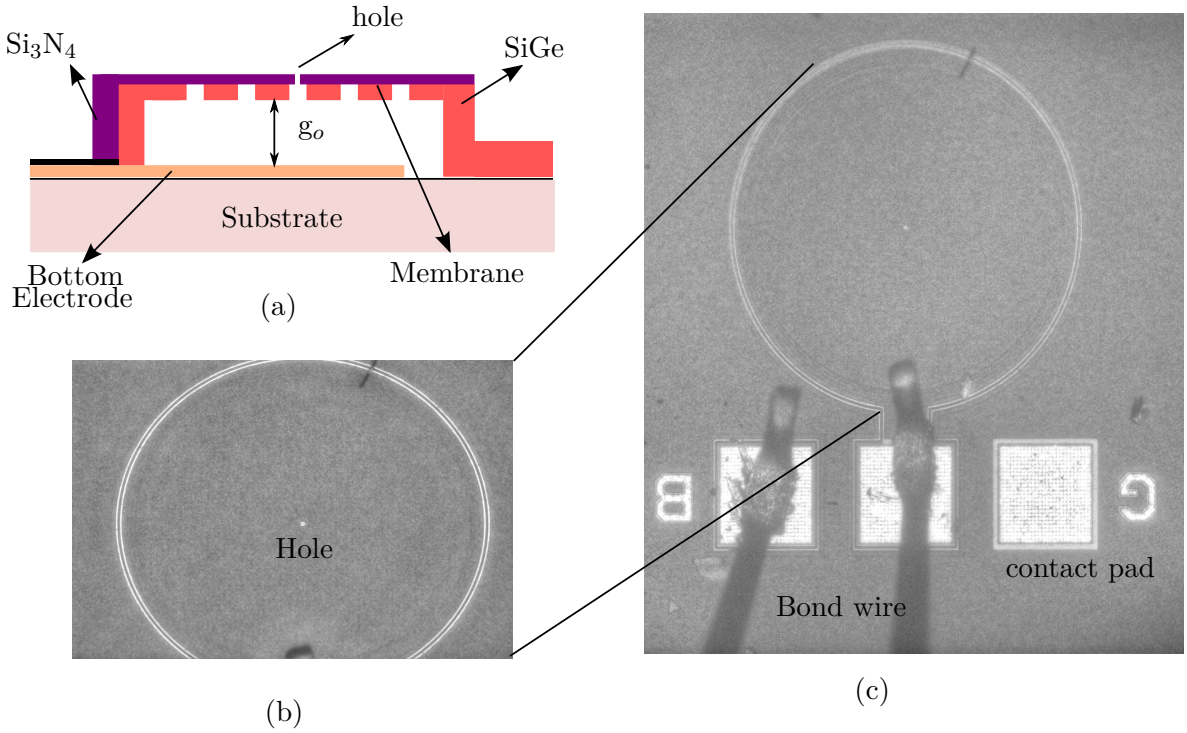

Figure 3-5: (a) Cross sectional view of the MEMS resonator. (b) and (c) are the microscopic images of the actual sample used.

Table 3-1: Electrical and mechanical parameters of resonator and experimental setup

Resonator	Bi-layer Circular diaphragm
Type	open (single center perforation)
Layer 1	$SiGe$
Layer 2	Si_3N_4
Film thickness h_1	$4\mu m$
Film thickness h_2	$2\mu m$
radius d	$170\mu m$
Density -$SiGe(\rho_1)$	$3827kg/m^3$
Density-$Si_3N_4(\rho_2)$	$3100kg/m^3$
Youngs modulus E_1	392 GPa
Youngs modulus E_2	310 GPa
Poisson's ratio ν_1	0.275
Poisson's ratio ν_2	0.27

3-3-1 Parameter extraction

For electrical parameter analysis, we consider a modified model of MEMS resonator known as Butter-worth Van Dyke (BVD) model [88] which is more accurate for extraction of parameters and design analysis. It takes into account the parasitic effects due to external connections, routing of electrodes and support losses. The modified model is a five element model with an additional shunt resistance as shown in Figure 3-6.

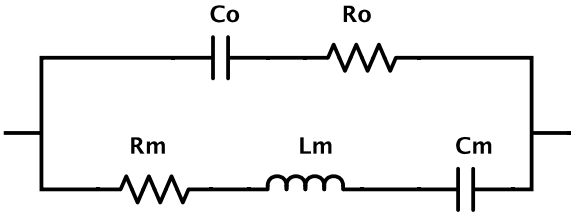

Figure 3-6: Butter-worth Van Dyke model for MEMS resonator.

For the above model, we can write

$$Z(\omega) = \left(R_m + j\omega L_m - \frac{j}{\omega C_m}\right) || \left(R_o - \frac{j}{\omega C_o}\right) \tag{3-13}$$

$$Y(\omega) = \frac{1}{Z(\omega)} = G + jB \tag{3-14}$$

The signal analyzer measures the real and imaginary part of input admittance (Figure 3-7). The electrical parameters are then extracted by curve fitting.

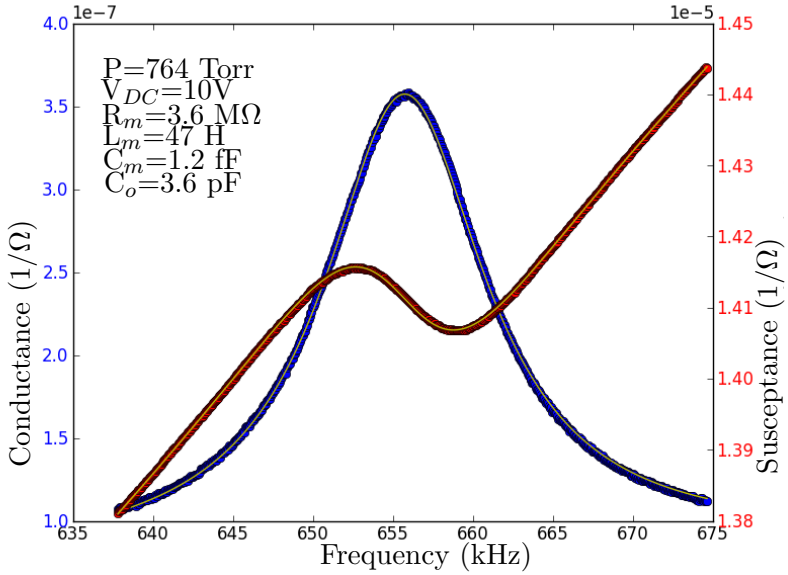

Figure 3-7: Input admittance measurement obtained from HP4194 analyzer. The superimposed-yellow graph is obtained from curve-fitting algorithm corresponding to Eq. (3-14)

To study the analytical behavior of the model, extracted parameters are plotted against DC bias at various pressures. The result is summarized in Figure 3-8 which shows the expected response according to Eq. (2-46)-Eq. (2-48). The slope of the graphs can be used to extract the mechanical parameters by using the following equations:

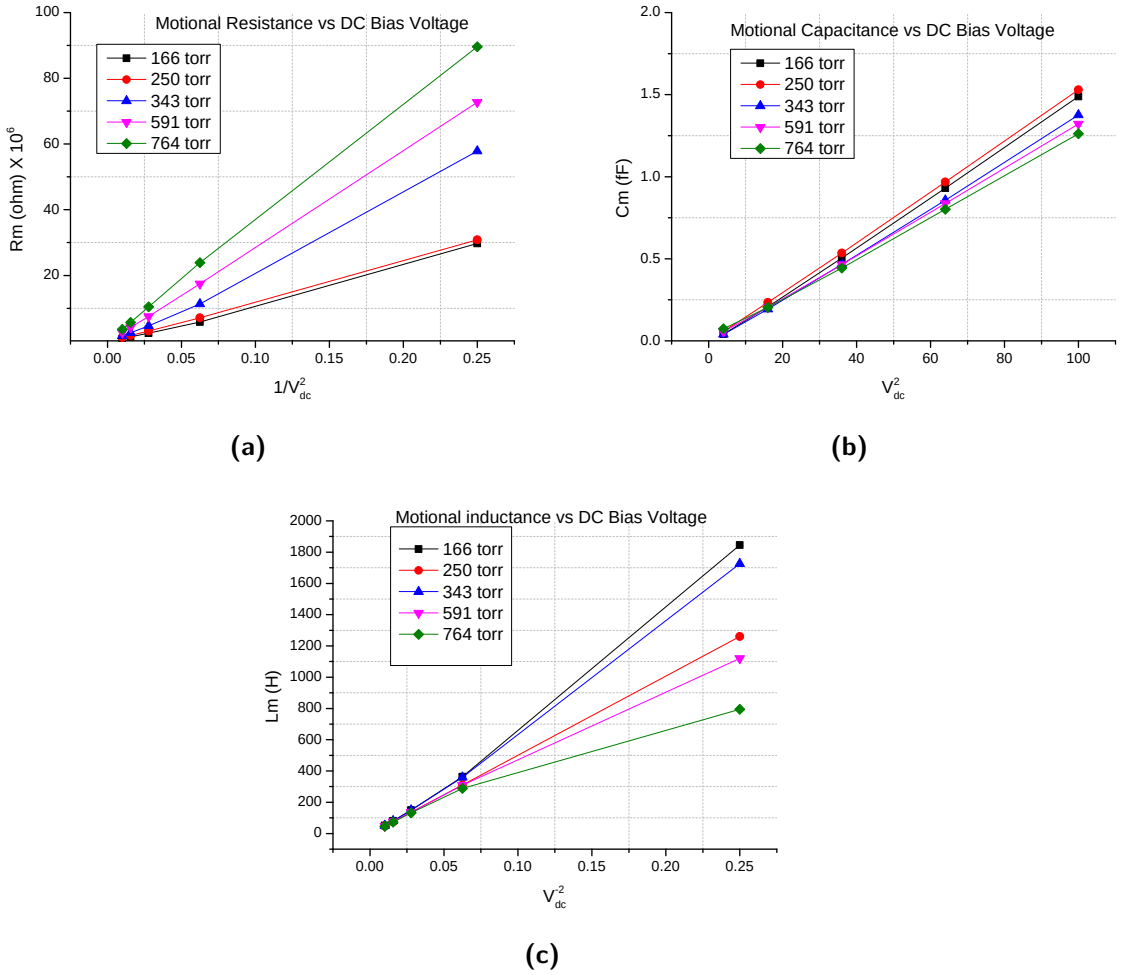

Figure 3-8: Variation of motional parameters vs square of the DC bias.

$$Q = \left(\frac{\sqrt{km}g_o^4}{\epsilon_o^2 A^2}\right)\left(\frac{\partial(1/V_{dc}^2)}{\partial R_m}\right) \tag{3-15}$$

$$k = \left(\frac{\epsilon_o^2 A^2}{g_o^4}\right)\left(\frac{\partial V_{dc}^2}{\partial C_m}\right) \tag{3-16}$$

$$m = \left(\frac{g_o^4}{\epsilon_o^2 A^2}\right)\left(\frac{\partial L_m}{\partial(1/V_{dc}^2)}\right) \tag{3-17}$$

From analytical theories [89], the effective mass of resonators is constant irrespective of it's resonance mode, Q or surrounding pressure. The squeeze film damping only contributes to

the damping factor and spring constant. Solving Eq. (3-17) at different pressures by using values from Table 3-1 and Figure 3-8, we obtain

$$\mathbf{m}_{expt}\mathbf{=3.676e\text{-}09\ kg}$$

The theoretical mass of the circular diaphragm obtained from Table 3-1 is equal to

$$m_{theo} = \alpha.[\rho_1 V_{SiGe} + \rho_2 V_{Si_3N_4}] \tag{3-18}$$

where α is the multiplication factor obtained from COSMOL simulation for circular membranes. It corrects for the displacement due to amplitude variations over the membrane area for the fundamental resonance mode. For our case, we obtain α =1.8.

$$m_{theo} = \alpha.[\pi r^2(\rho_1 h_1 + \rho_2 h_2] \tag{3-19}$$

$$\mathbf{m}_{theo}\mathbf{=3.69e\text{-}09\ kg}$$

The experimental results for effective mass are similar to the expected theoretical value. Since we expect mass as well as slope in Figure 3-8c to be constant at all conditions of pressure, we see a deviation in the response at low voltages. At low excitation amplitudes, the inaccuracies in the effective mass could be due to asymmetrical properties of the membrane arising to contact probes and discontinuities on the edges (Figure 3-5). Due to the uncertainty in air-gap and electrode area in Eq. (3-15) - Eq. (3-17), extraction of mechanical parameters from electrical measurements may lead to inaccuracies . To study the effect of squeeze-film damping on quality factor and spring constant, we alternatively use the following equations

$$Q = \frac{\omega_o L_m}{R_m} \tag{3-20}$$

$$k = m\omega_o^2 \tag{3-21}$$

$$b = \frac{m\omega_o}{Q} \tag{3-22}$$

3-3-2 Modeling squeeze film damping

For five different values of pressure in Figure 3-9 and Figure 3-10, we clearly see the shift in resonance frequency with a slope of **95.25 kHz/bar** accompanied by decreasing Q with increasing pressures. At resonance, the membrane deflection is maximum and more mechanical energy is dissipated i.e work done against the ambient gas pressure. Since this dissipation must be compensated, a peak in the conductance response is seen.

From Eq. (2-37), we can estimate the theoretical upper limit for frequency shift for $\omega\tau >> 1$ which is given by

$$\frac{dk_{eff}}{dp} = 2m\frac{d\omega_o}{dp}\omega_o \tag{3-23}$$

$$\frac{dk_{squeeze}}{dp} = 2m\omega_o\frac{d\omega_o}{dp} \tag{3-24}$$

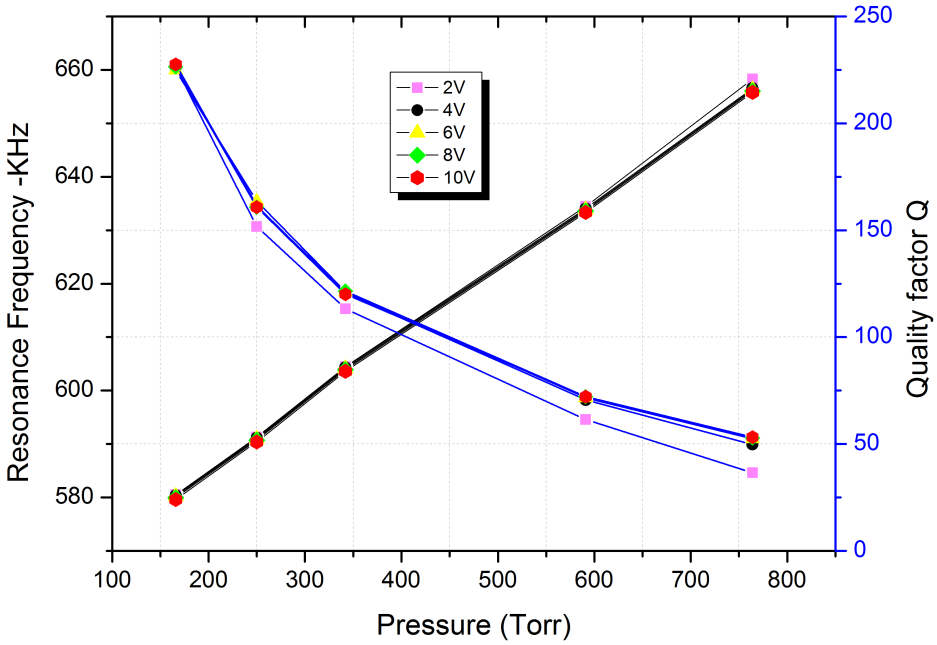

Figure 3-9: Dependence of Quality factor (Eq. (3-20)) and resonance frequency for different values of pressure. The measured frequency shift is equal to **95.25 kHz/bar**.

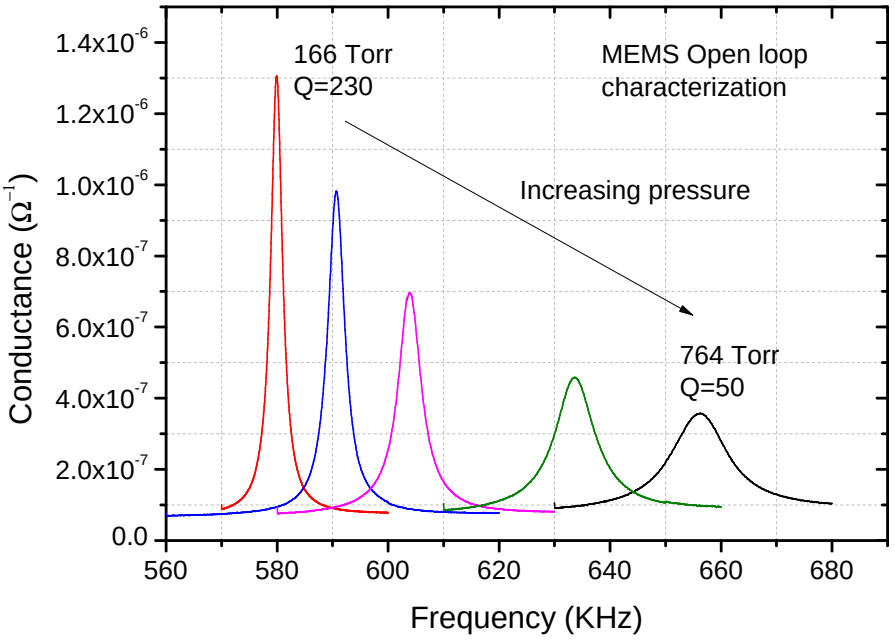

Figure 3-10: Conductance response of the MEMS resonator for different pressures.

$$\frac{d\omega_o}{dp} = \frac{1}{2m\omega_o}\frac{A}{g_o} \tag{3-25}$$

For a measured value m and ω_0 (at atmospheric pressure), we estimate a frequency shift of 50 kHz/bar which is less than 2 times larger than the observed shift of 95.25 kHz/bar. We can conclude that our device is operating in the regime where $\omega\tau >> 1$. Theoretical change in the spring constant can be calculated as

$$\left(\frac{dk_{eff}}{dp}\right)_{theo} = \frac{A}{g_o} = 0.09 \tag{3-26}$$

which can be compared to the experimental data equal to

$$\left(\frac{dk_{eff}}{dp}\right)_{expt} = 2m\frac{d\omega_o}{dp}\omega_o \approx 0.1 \tag{3-27}$$

Since the analytical model is valid in our case, the damping coefficient from Eq. (2-36) now reduces to

$$b_{squeeze} = \frac{pA}{g_o\omega^2\tau_d} \tag{3-28}$$

By knowing the quality factor and resonance frequency, we can now calculate the damping coefficient by using Eq. (3-22) and estimate the diffusion time at different pressures (Table 3-2)

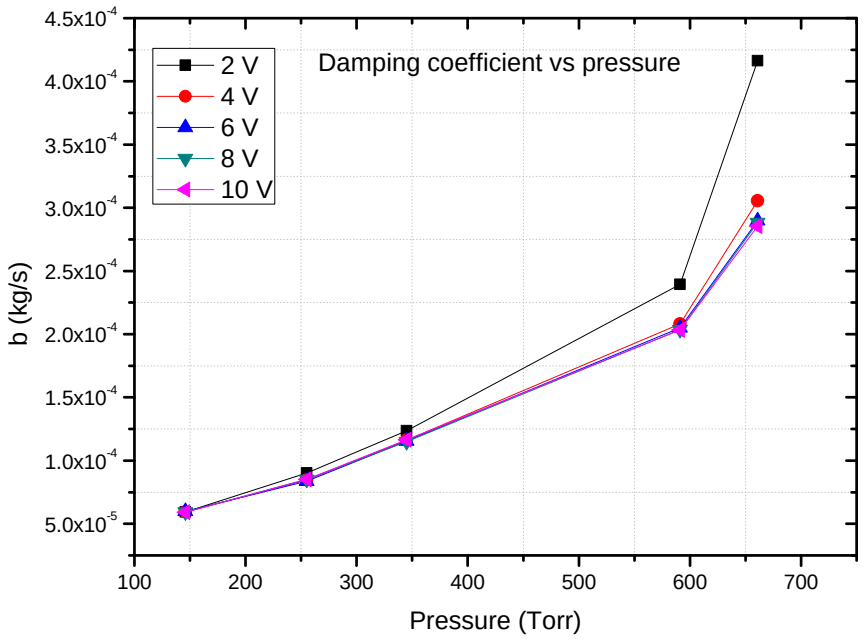

Figure 3-11: Damping coefficient estimated from Bao's model at various pressures.

From the above result we see that squeeze film damping introduces a fractional change of **0.001** % in damping coefficient and **0.0034** % in spring constant. Skvor's model has not

Table 3-2: Squeeze film model -extracted parameter

Pressure	$b(Kg/s)$	$k_{eff}(N/m)$	$\tau_d(\mu s)$
146 Torr	5.94e-05	4.87e+04	2.23
255 Torr	8.58e-05	5.05e+04	2.61
345 Torr	1.17e-04	5.28e+04	2.46
591 Torr	2.11e-04	5.81e+04	2.12
661 Torr	3.17e-04	6.24e+04	1.48

been used here as it underestimates the damping parameters. The model is applicable for low frequencies or large air gap. At an operational frequency of 600 kHz and low diffusion time of gas molecules, the effective area of the membrane seen by the gas molecules is much lower than one used in Skvor's model. From the extracted sensitivity of k and b, we obtain a diffusion time of **2.18** μs with an **error of 0.38** μs which returns $\omega\tau_d \approx 9$. Although the product does not exactly fall under the assumed regime ($\omega\tau_d >> 1/\tau_d$), the model quite fairly estimates the sensitivity $dk_{squeeze}/dp$ with **11.11 % error** in comparison to it's theoretical counterpart.

3-4 Optical Detection

Non-electrical nature of signals is what distinguishes optical detection from various other detection techniques for vibration analysis. Fiber optic sensor technology has emerged as a new replacement for existing sensor technology [90] by providing a non-contact, perturbation free means of vibration monitoring by using compact instrumentation in electrical machinery with electrical isolation. This reduces fabrication complexity for MEMS resonators which otherwise requires integration of additional materials for electrical read-out. The negative influence of electromagnetic interference (EMI) with electrical signals which is a real problem, can be eliminated by optical measurements [91]. Vibration sensing can take place inside the optical fiber (intrinsic sensors) or outside (extrinsic sensors) but depending upon the working principle, they can be categorized into [92] :

- **Intensity modulation detection** : The light intensity from the source is modulated (change in transmitted power) by the vibrating resonator. The modulated signal is guided to a photo diode and converted into electrical signals for processing. They have been used in micro-bend sensors for strain/stress sensing [93] and non-contact displacement sensing [94]. Intensity based sensors are low cost and easy to implement but significant amount of error can arise due to the change in transmitted power at the reflective surfaces.
- **Interferometric detection** : The dark and bright fringes formed due to interference between transmitted and reflected beams from the sample are used to measure the vibrations. Various interferometric systems like Fabry Perot (FP) interferometer or Michelson interferometer have been used for sensing application [95]. In [96], a highly accurate system using double FB cavity is used. They provide high precision during

real-time measurements and are classified as one of the most sensitive structures. The main disadvantage is the error due to optical system alignment.

- **Fiber Bragg Grating (FBG) detection** : FBGs are devices which consists of longitudinal periodic variations in refractive index of the core of an optical fiber. A series of FBGs placed in an optical path results in a series of interferences when light travels through them. Depending upon the value of refractive index which the beam sees, some wavelengths experience a transmission blockage and are reflected (Fresnel reflection [97]). As such FBGs acts as wavelength selective reflectors and the reflected beam represents a peak (Bragg peak) in the frequency domain. When a vibration is applied to a FBG, the reflection spectrum curve shifts in the direction according to the motion of the resonator and is processed for sensing applications . This technique offers dense wavelength multiplexing complexity for accurate vibration sensing [98], [99] .

Of all the types discussed above, interferometric detection offers the highest resolution and are hence suited for characterization of nano-mechanical vibrations. Of all the available interferometric based detection system , Laser Doppler Vibrometry (LDV) will be used for our goal and is discussed in the subsequent section.

3-5 Laser Doppler Vibrometry (LDV)

Laser doppler vibrometry is a velocity transducer i.e. it measures the velocity of the moving resonator on the principle of measuring the doppler frequency shift. When a laser beam of wavelength λ is targeted on a moving sample with a velocity v, the source sees a frequency modulated reflected signal due to the doppler effect. The shift in the frequency is dependent on the velocity of the moving sample according to the following relation

$$f_d = \frac{2v}{\lambda} cos\theta \tag{3-29}$$

where $v.cos\theta$ is the velocity component along the laser beam. To be able to estimate the surface velocity of the sample, the doppler frequency shift needs to be measured at a given wavelength. For MEMS resonator, surface velocities can be as low as 1 mm/s . For a He-Ne laser source with a corresponding wavelength of 632.8 mm, a frequency shift of 3.16 kHz is observed per 1 mm/s which compared to the laser frequency (4.7×10^{14} Hz) is very small. To measure such small shifts we use interferometers. Figure 3-12 shows a block diagram of LDV system.

The source beam f from the laser is split in two by a beam splitter. One part of the beam is directed towards the sample and the other is directed towards a bragg cell. The reflected doppler shifted beam $f + f_d$ from the sample is interferred with a bragg cell shifted frequency $f \pm f_b$. The path difference r_1 and r_2 between the two input beams to the interferometer leads to dark and bright pattern pattern. The intensity of the total signal is given by

$$I_{tot} = I_1 + I_2 + 2\sqrt{I_1 I_2 cos[2\pi(r_1 - r_2)/\lambda]} \tag{3-30}$$

The moving sample generates a time dependent path difference $r_1(t) - r_2$ which modulates the frequency shift. Each fringe represents a sample displacement equivalent to $\lambda/2$ i.e 316 nm

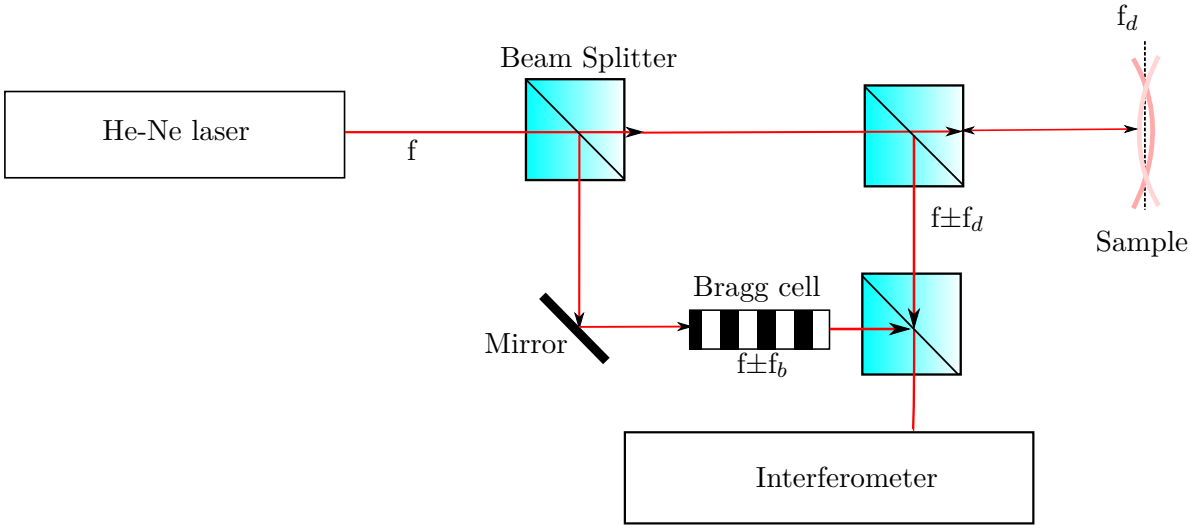

Figure 3-12: Optical setup of Laser Doppler Vibrometry.

(for He-Ne laser). The purpose of the bragg cell is to determine the direction of velocity. It works as an opto-acoustic modulator which shifts the input frequency by $f_b = 40$ MHz. If the sample moves towards the laser source, detector receives a frequency lower than f_b otherwise a frequency higher than f_b. As such LDV can be used to measure both the magnitude and the direction of the sample velocity. LDV can be used to measure displacement amplitudes x of any sample from the measured velocity by using

$$v = 2\pi f.x \tag{3-31}$$

The measured velocity or displacement are then converted into analog signals for data processing and acquisition. Apart from offering a high resolution, LDV also allows 3-D surface measurements by scanning the laser beam across the surface of the sample. We have used POLYTEC instruments to study the various resonance modes due to Brownian motion of an Atomic Force Microscopy (AFM) cantilever as shown in Figure 3-13.

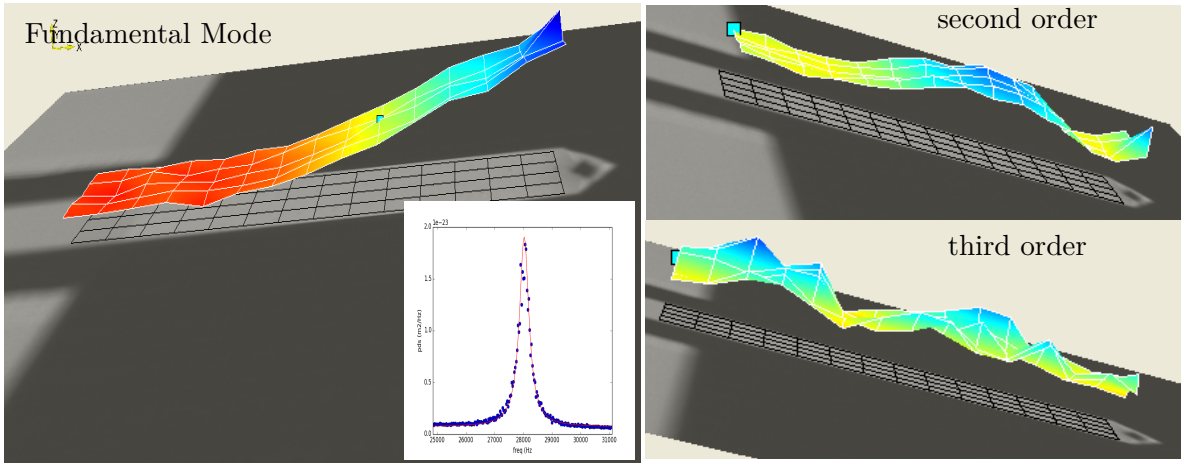

Figure 3-13: Measuring brownian motion of an AFM cantilever using polytec LDV system.

3-6 Optical measurement : Open Loop characterization

Polytec MSA-400 scanning LDV was used to optically detect vibrations of the resonator and to study its surface topography. The sample was placed directly under the laser source ($\lambda = 633$ nm) and was actuated by applying a voltage signal using **Agilent 33250A**. The measured velocity was converted into electrical signal by using a suitable velocity decoder **(VD-20)** supported by polytec **OFV 5000** vibrometer. The conversion of velocity to voltage was done with a sensitivity of $S_v = 20mm/s/V$. Maximum output signal is obtained with the laser spot positioned in the center of the membrane where deflection amplitude attains its maximum value. Experimental setup and frequency response of the sample is shown in Figure 3-14.

To measure the air gap between the two electrodes, we actuate the sample with high DC voltage up to 120V . In the absence of an ac signal, the membrane doesn't resonate but instead undergoes static deflection due to force generated by DC source. With higher DC bias, the deflection amplitude increases to a point when the top electrode collapses with the bottom electrode. The surface measurement under collapse condition using polytec topography analyzeris shown in Figure 3-15. We measure an air gap of g_o=**960 nm** which is close to fabricated specification (1000 nm) of the sample.

3-7 MEMS oscillator using optical feedback

From Figure 3-3, we can finally construct an optical feedback based oscillator. Electrostatic excitation converts electrical signal into mechanical motion while Polytec MSA analyzer detects the vibration by optical interference thereby converting the mechanical motion into frequency modulated optical signal. Rather than using a conventional sustaining amplifier to close the loop, we instead use the optical signal via vibrometer that outputs a velocity decoded voltage signal. Figure 3-16 shows the complete experimental setup of the proposed opto-electronic MEMS oscillator. The sample is confined inside a vacuum chamber, the internal pressure is controlled by an external knob. The phase and gain loop conditions are controlled by the phase shifter and an Automatic Gain Control (AGC) circuitry respectively. The Bias-Tee superimposes a DC signal onto the generated AC signal which is used to actuate the MEMS resonator. The frequency of the output signal is measured by a high precision frequency counter.

Returning to the electrical model of MEMS resonator, the system would only oscillate if the following condition [43] holds

$$R_m \leq \frac{1}{2\omega_o C_o} \tag{3-32}$$

i.e. for Figure 3-6, the system will not oscillate if :

- R_m is too large. ;
- ω_o is too high.;
- C_o is too large.

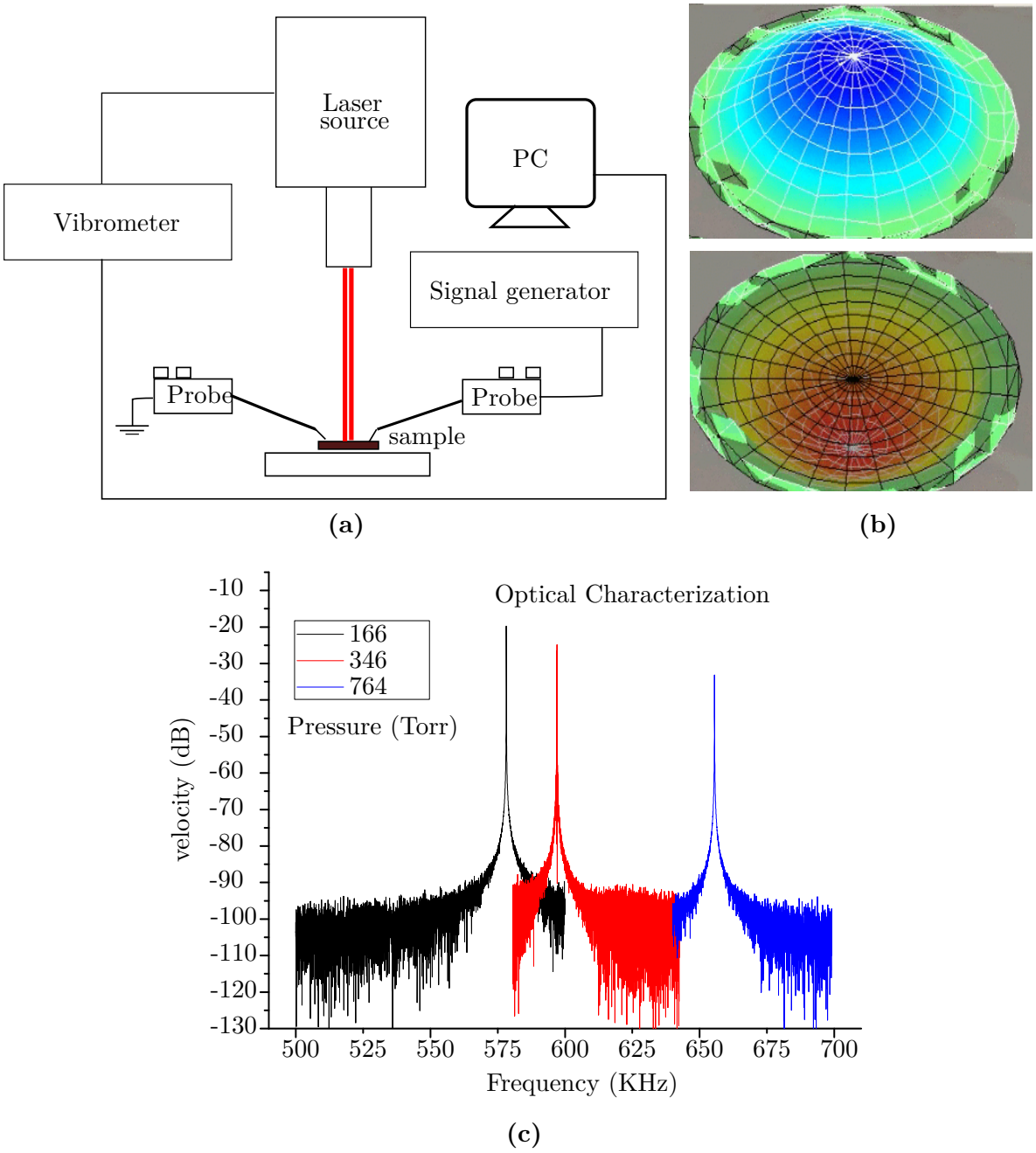

Figure 3-14: (a) Experimental setup for sample characterization using LDV. (b) 3D grid-view of the membrane at resonance. (c) The measured frequency response for 3 different pressures at 10 V_{dc} and 200 mV_{ac}. The peak signal at resonance is decreased due to increased damping at higher pressures.

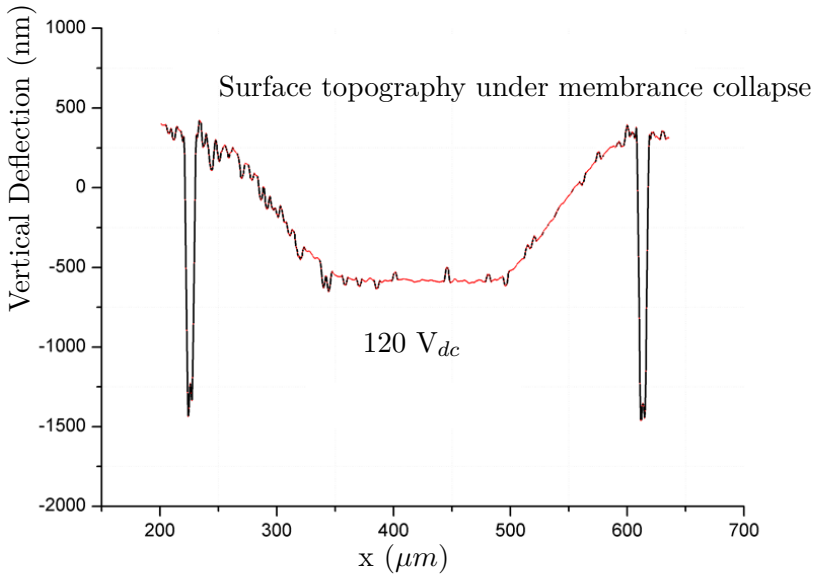

Figure 3-15: Membrane capacitive gap analysis using polytec topography analyzer. The measurement was carried out in short coherent mode followed by linear regression.

With conventional MEMS oscillator that use electrical signals for vibration detection, the shunt capacitor (along with external parasitic capacitance) posses a big problem for achieving stable oscillation. The effect of C_o and other parasitic capacitance is completely eliminated when LDV as a velocity transducer is used. Yet, the basic oscillation conditions needs to be fulfilled i.e. Eq. (3-3) and Eq. (3-4) needs to be satisfied . For this purpose, the Gain/Phase control block in Figure 3-3 consists of a phase shifter which adjusts the closed loop phase until the oscillation conditions are met. To have a closed-loop stability, it is important to limit the amplitude of the signal. This is done by an automatic gain control circuit and is discussed in the following section.

Table 3-3: Components used in Figure 3-16.

Laser Scanner	Polytec MSA 500
Vibrometer	Polytec OFV 5000
velocity Decoder	20 mm/s/V
Spectrum Analyzer	HP 89410A VSA
Frequency counter	Fluke 6681
DC Source	Agilent 33250A
Bias Tee	Picosecond 5530A
Pressure Readout	GRANVILLE-275 Mini Convectron
Pump	Pfeiffer

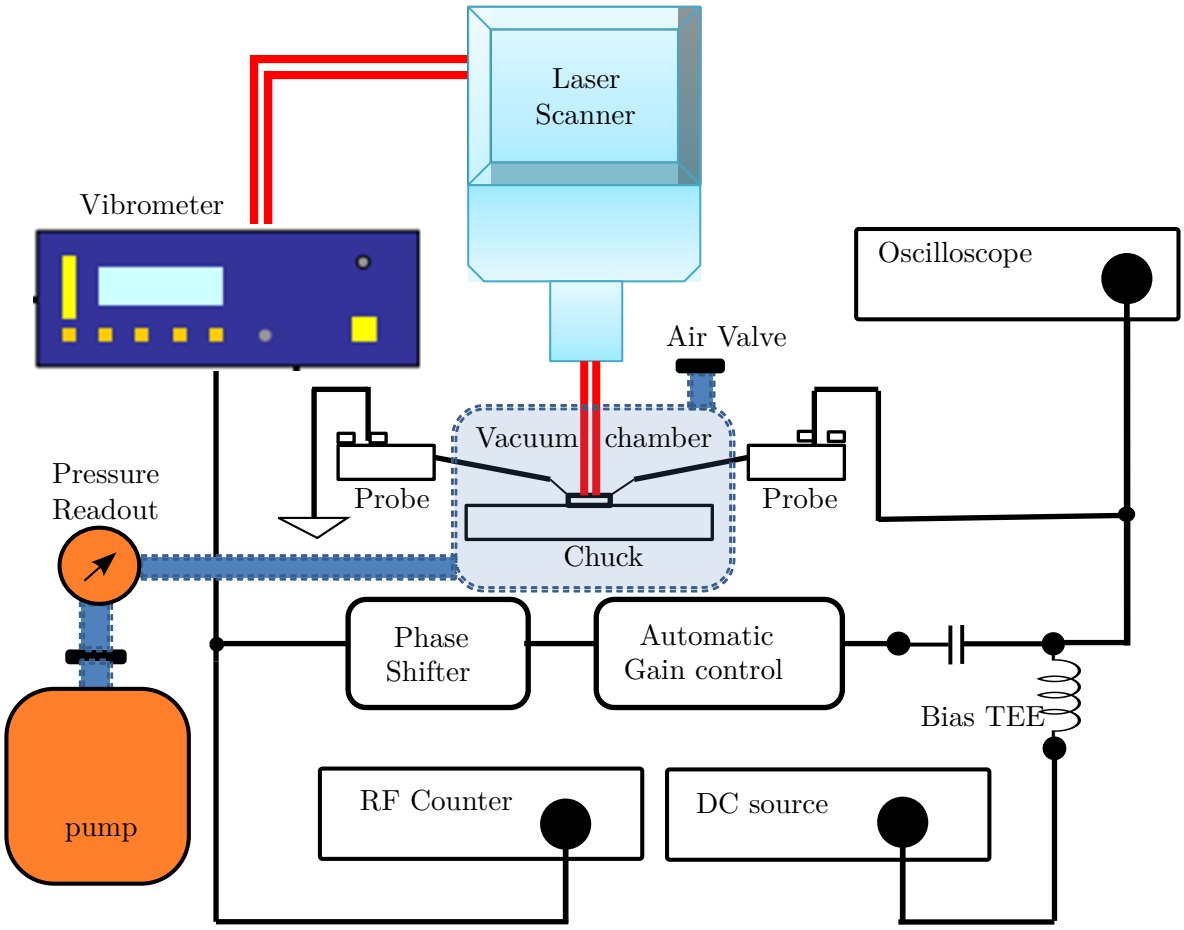

Figure 3-16: Experimental setup of the proposed MEMS oscillator using optical feedback by laser Doppler vibrometer. Refer to Table 3-3 for the list of components used.

3-7-1 Phase -Shifter

The basic principle of a phase shifter is to have a complex input impedance in the path of an input signal. Simple R-C ladder circuits can be used to add delay (phase) but this leads to attenuation due to resistive paths. We use an active 1^st order all pass filter as shown in Figure 3-17 as a phase shifter. When $R_1 = R_2 = R_3$, the filter provides a unity gain for all frequencies but adds a delay to the output response. The transfer function for a 1st order all pass filter is given by

$$\frac{V_{out}}{V_{in}} = \frac{s - \frac{1}{R_3 C_1}}{s + \frac{1}{R_3 C_1}} \tag{3-33}$$

which gives a frequency dependent phase shift of

$$\phi = -2tan^{-1}\left(\frac{R_3 C_1}{\omega}\right) \tag{3-34}$$

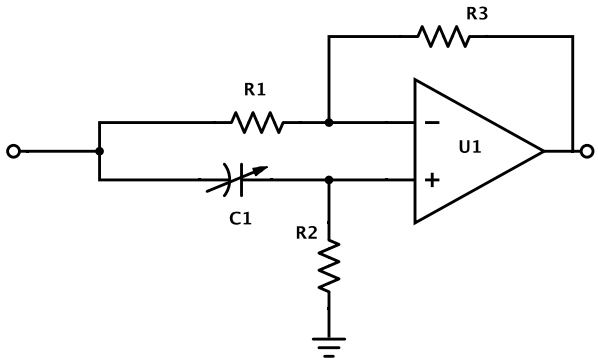

Figure 3-17: First order all pass filter used as a phase shifter.

The phase shift goes from -180 degrees at 0 Hz to 0 degrees at high frequency. By using the variable resistor or a capacitor, a suitable phase shift can be added to the signal. In our case we use a tunable capacitor **(10 pF-150 pF)** and obtain a the phase delay from **-105 degrees to 2 degrees** as shown in Figure 3-18. Additional phase shift of **75 to 180 degrees** can be obtained by inverting the input signal thereby introducing a shift of 180 degrees.

3-7-2 Automatic Gain Control (AGC)

The second part of the control block, automatic gain control (AGC) circuit is used to stabilize the oscillation amplitude to an optimum level. A basic principle of an AGC is shown in the block diagram (Figure 3-19). The signal's absolute value is extracted by a peak detector and filtered by an RC low pass filter giving an output signal average value. The subtractor block then compares it with a reference (or optimum level) signal . The integrator together with a variable gain amplifier regulates the signal amplitude to minimize the error. Of course various other topologies can be made for AGC circuits [100] but the basic principle remains the same.

AGC designed for our oscillator consists of an op-amp U2 configured as a variable gain amplifier. Diode D1 acts as peak detector passing a negative DC ripple which is rectified by

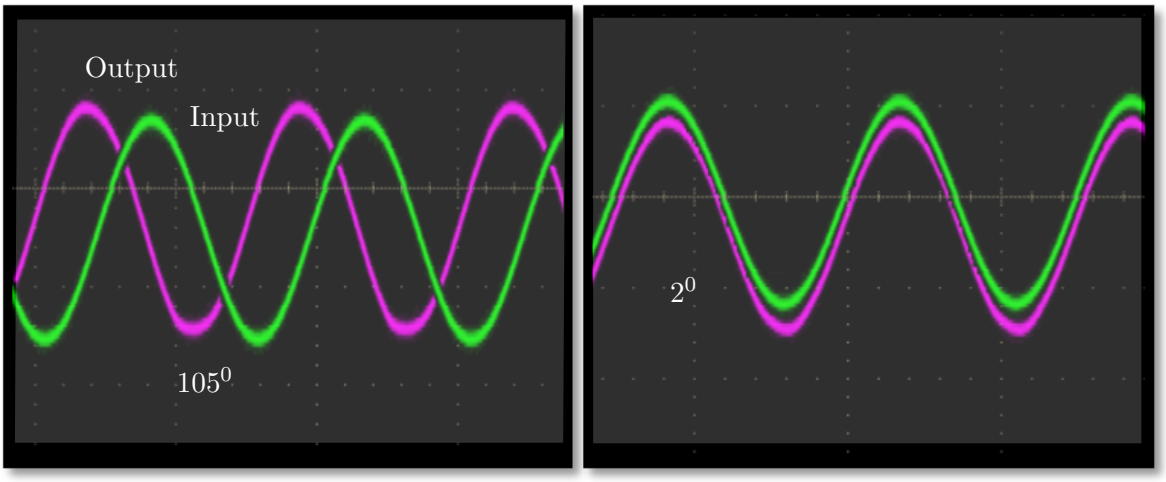

Figure 3-18: Phase shifter response as measured with an oscilloscope by varying C1 from 10 pF to 150pF.

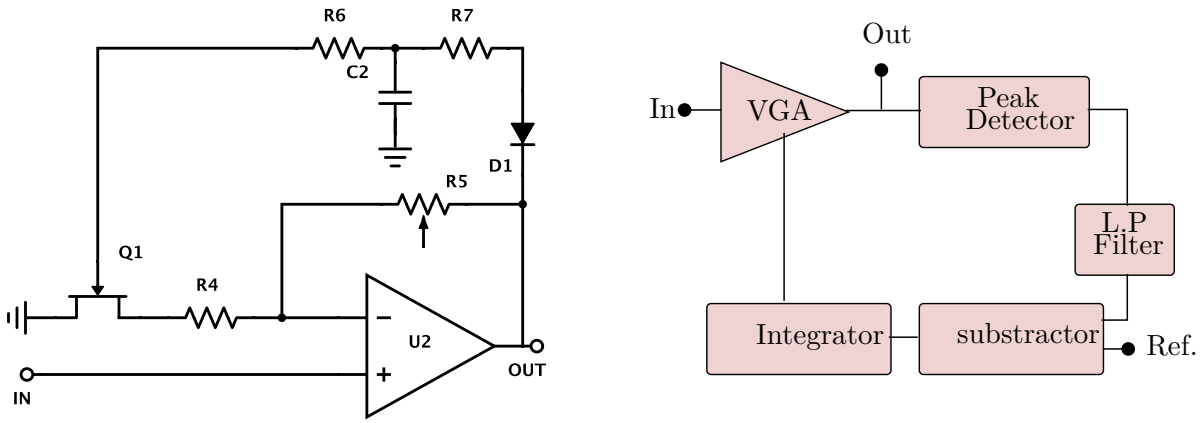

Figure 3-19: Block diagram of an AGC circuit along with it's actual implementation.

the low pass filter (R7-C2) . The DC signal is applied to the gate of Q1, a N-channel J-FET used as a gain controlling element and offers excellent control due to its wide range of drain-source resistance which is controlled by the gate voltage. The gain of U2 for a non-inverting configuration can be written as

$$\frac{V_{out}}{V_{in}} = 1 + \frac{R_5}{R_Q + R_4} \tag{3-35}$$

Depending upon the negative swing at the output, R_Q is modified by the DC bias of Q1 and thus controlling the gain until the voltage is stabilized. An optimized signal level can be obtained by tuning the variable resistor R5.

3-8 Resonant pressure sensing

The system would start oscillating only when the loop gain is unity and a closed loop phase shift is 0. For a given phase and gain, the oscillator can resonate at any frequency in the

vicinity of ω_o. To have the resonator oscillate exactly at its mechanical resonance frequency, we tune the phase shift and gain to a point where the system begins to oscillate at a minimum value of input DC bias. A higher input DC bias shifts the oscillating frequency in either direction so as to satisfy the oscillation conditions. The internal pressure of the chamber was pumped down to low pressures and a minimum DC bias was found for each oscillator response. The frequency output at this minimum input signal was measured by a spectrum analyzer at various pressures and plotted. The results are summarized in Figure 3-20 and Figure 3-21.

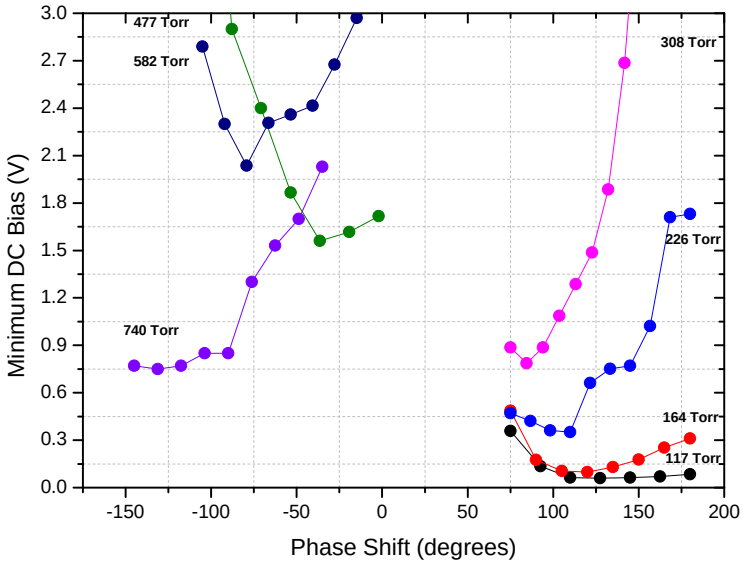

Figure 3-20: Measured DC bias vs phase shift for various pressure. The phase shift was obtained by tuning the capacitor from 10-150 pF.

Pressure dependence of **97.16 kHz/bar** from Figure 3-21 is experimentally obtained i.e. for a frequency shift of 1 Hz (0.97 Hz), the pressure changes by 1 Pascal. From practical point of view, detection of 1 Hz frequency shift is not easily achievable. The smallest change in pressure, δp_{min} that the oscillator can detect is limited by minimum resolution of frequency measurement system according to

$$\delta p_{min} = \frac{1}{S_p}\left(\frac{\delta\omega}{\omega}\right)_{min} \tag{3-36}$$

where S_p , the relative pressure sensitivity is given by

$$S_p = \frac{1}{\omega}\left(\frac{d\omega}{dp}\right) \tag{3-37}$$

To achieve a high resolution, the frequency response should be free from instability which may arise due to various noise sources within or outside the loop.

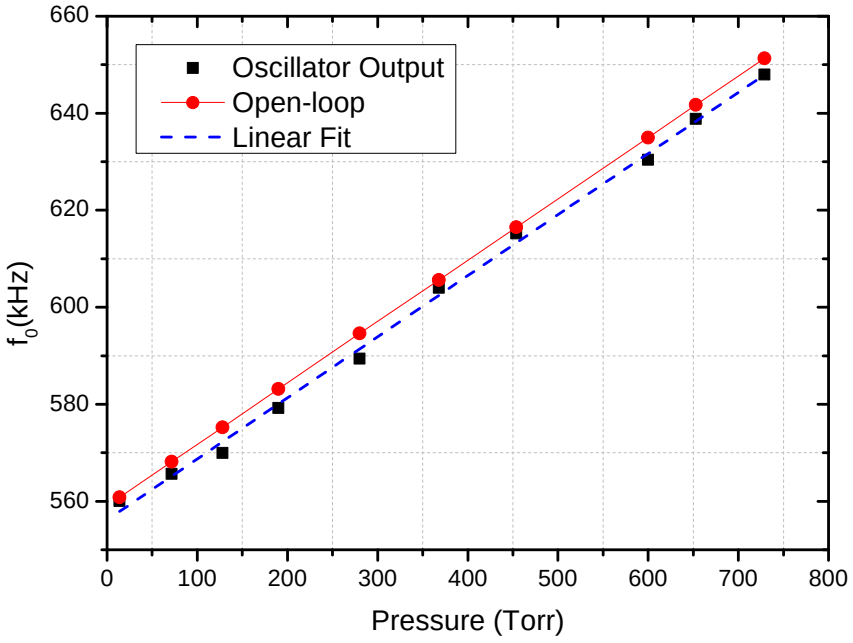

Figure 3-21: Measured frequency output vs pressure. As expected, the system's resonant frequency shows a linear dependence on the pressure with a slope of **97.16 kHz/bar**.

3-9 Oscillator frequency response : Phase noise

The frequency spectrum on an oscillator should ideally contain only a single frequency but in reality the presence of short term frequency fluctuation leads to broadening of the frequency spectrum. The frequency instability can be due to non-deterministic noise sources such as flicker noise and white noise and can cause fluctuations in the phase ($\varphi(t)$) and amplitude ($\alpha(t)$)of the oscillator signal as shown in Figure 3-22.

Compared to an ideal response given by $V_o sin\omega t$, a noisy oscillator response can be represented by

$$V(t) = V_o(1 + \alpha(t))sin[\omega t + \varphi(t)] \tag{3-38}$$

The cleanness of the output spectrum is the defining factor for the overall accuracy of the system which determines the maximum bit rate and minimum power consumption. While the amplitude fluctuations can be reduced by AGC , the phase noise still remains unaffected and gets accumulated with time and hence characterizes the cleanness of oscillation. It negatively influences the bandwidth especially in communication systems with narrow channel spacing. Considerable amount of theoretical and experimental work has been done on phase noise for conventional oscillators based on LC tank circuits [101], [102], CMOS oscillators [103], and noisy signal sources [104]. For MEMS oscillators, electrostatic transduction [105], amplifier non-linearities due to AGC [106], input noise at resonator bias ports [107] and mechanical noise from the resonator [108] itself leads to further noise. An analytical model of phase

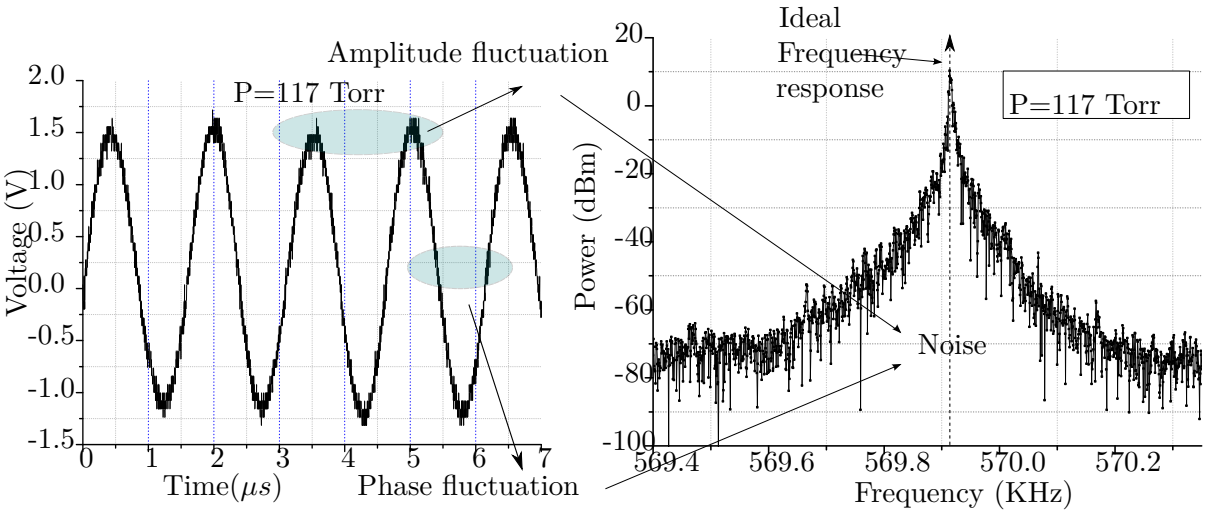

Figure 3-22: Oscillator output at a pressure of 117 Torr measured using (a) oscilloscope and (b) spectrum analyzer. Compared to an ideal single peak, the response is much wider due to external/internal noise sources.

noise for MEMS oscillator can be derived by using the RLC model of resonator as shown in Figure 3-23.

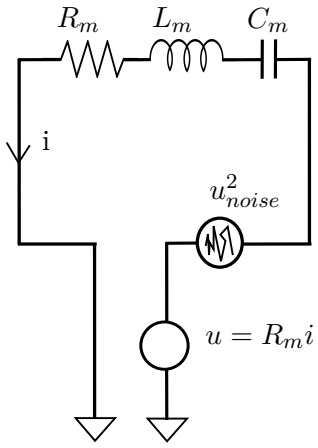

Figure 3-23: Idealized oscillator with a MEMS resonator and a trans resistance amplifier converting current into a voltage source. All the possible noise signals are summed up into one voltage source.

The transresistance amplifier ($u = R_m i$) provides the feedback for closed loop oscillations. At resonance, the loop gain is unity, the amplifier cancels the resistive losses and L_m and C_m cancels each other at ω_o. At a small offset frequency $\omega_o + \Delta\omega$, we can write

$$i = \frac{u_{ac}}{Z} \approx \frac{u_{ac}}{R + j2\Delta\omega L} \tag{3-39}$$

Including the voltage sources from the amplifier and noise signals, we have

$$\frac{u}{R_m} \approx \frac{u + u_{noise}}{R + j2\Delta\omega L} \tag{3-40}$$

Solving Eq. (3-40) for u gives an expression for output noise as

$$|u_{noise-out}|^2 = |u_{noise}|^2 \left[\left(\frac{\omega_o}{2\Delta\omega Q} \right)^2 + 1 \right] \tag{3-41}$$

Normalizing the output noise signal to signal u_{ac} gives an expression for single band phase noise.

$$S_\phi(\omega) = \frac{|u_{noise-out}|^2}{|u_{ac}|^2} \left[\left(\frac{\omega_o}{2\Delta\omega Q} \right)^2 + 1 \right] \tag{3-42}$$

Expression for the noise signal can be simplified if we consider the thermal noise and the noise due to amplifier which results in the well known Leeson's phase noise model [109] given by

$$S_\phi(\omega) = \frac{FkT}{2P_{in}} \left[\left(\frac{\omega_o}{2\Delta\omega Q} \right)^2 + 1 \right] \tag{3-43}$$

where F is the noise figure of the amplifier, k is Boltzmann constant, T is the absolute temperature and P_{in} denotes the input power that is available at the node where the noise is inserted. The factor of 2 arises from the fact that only one-half of the total noise corresponds to phase noise while other half goes to amplitude noise. Leesons'model predicts a $1/f^2$ roll-off i.e. -20 dB/dec fall with increasing offset frequency. However, in practice MEMS oscillator also exhibit a strong $1/f^3$ roll-off due to the presence of $1/f$ flicker noise at lower frequencies which is considered in the modified leeson's equation given by Eq. (3-44). Figure 3-24 shows a phase noise response of the opto-electronic MEMS oscillator at 2 different pressures where only $1/f^2$ noise is observed.

$$S_\phi(\omega) = \frac{FkT}{2P_{in}} \left[\left(\frac{\omega_o}{2\Delta\omega Q} \right)^2 + 1 \right] \left[1 + \frac{\Delta\omega_{1/f^3}}{\Delta\omega} \right] \tag{3-44}$$

The first term in Eq. (3-45) corresponds to the thermal-mechanical noise of the resonating membrane and the second term is due to the noise injected by the measurement system i.e. the noise from the oscillator electronics plus the noise injected from the LDV. From Figure 3-24, we can conclude that at low offset frequency, noise decreases with a $1/f^2$ slope. At an offset frequency equal to 10 kHz, the total phase noise is limited by the thermal noise (f^0 slope) due to the measurement electronics and is equal to

$$S_\phi^{circuit+LDV}(\omega) = -80dBc = 1 \times 10^{-8} rad^2/Hz \tag{3-45}$$

It is clear that the reduced phase noise can be obtained at higher input power i.e. driving the resonator at higher bias voltage . The same effect can also be achieved at higher Q and have been experimentally reported [110].

3-10 Accuracy and noise of MEMS oscillator

Any external noise/interactions which gets translated into variations in amplitude or phase results in the fluctuations in the oscillation frequency and hence limits the performance of sensor devices. The oscillator considers a MEMS resonator as an energy tank storing vibrational

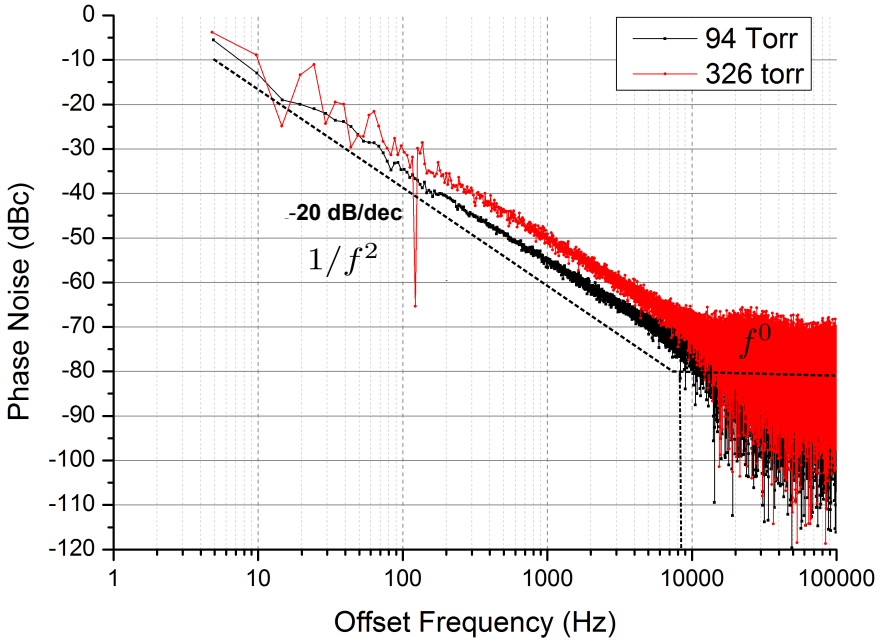

Figure 3-24: Phase noise response of the oscillator. A slope of -20dB/dec indicates the presence of $1/f^2$ noise at low offset frequencies.

energy at ω_o. The total energy fluctuates slightly around it's mean value E_o due to random energy fluctuation i.e. noise $U(t)$ whose spectral content is centered around ω_o. Keeping a high level of signal-to-noise ratio, the error in frequency δf can be made low, thereby increasing the accuracy of the sensor. There are at least four sources of noise which can lead to phase/frequency fluctuations namely

- Thermal-mechanical noise of resonator.;
- Noise from the detector due to displacement variations of the membrane.;
- Noise from the actuator providing driving force.;
- Feedback induced noise (amplification, filtering etc).

Electrostatic driving offers excellent phase control [111] and hence noise from the actuator is usually dominated by thermal and sensor induced noise. Compared to conventional non-feedback resonant sensing, feedback loops shows a shift from it's native f_o (without feedback) to $f_{osc} = f_o + \delta f_{loop}$ [112], [113]. The slope of the phase-frequency transfer function around the native f_0 is the highest one thereby giving the highest frequency stability due to phase variations. The loop makes the system to oscillate out of f_0 thereby lowering the frequency stability which give rise to feedback induced noise. The feedback induces noise can be lowered/eliminated by running the system at the minimum DC bias signal as previously discussed in Figure 3-20.

3-10-1 Thermal-mechanical noise

Thermal mechanical noise is due to the agitation of surrounding molecules which induces the so called random thermal motion or Brownian motion. Returning to Eq. (2-3), we can consider an extra contribution of the Brownian motion to the total membrane's displacement as $\delta x_b(t)$.

$$x(t) = X(\omega_{osc})e^{i(\omega_{osc}t-\phi)} + \delta x_b(t) \tag{3-46}$$

$$X(\omega_{osc}) = \frac{\eta V_{ac}}{m\sqrt{(\omega_o^2 - \omega_{osc}^2)^2 + (2\zeta\omega_o\omega_{osc})^2}} \tag{3-47}$$

The term $\delta x_b(t)$ occurs due to the presence of noise force $f_n(t)$ which has a white spectral density $S_{fn}(\omega)$ and a Gaussian distribution with a zero mean. Fluctuation-dissipation theorem [114] applies to mechanical resonator with a finite Q and therefore by using the well-known Nyquist criteria [115], noise force spectral density can be written as

$$S_f^T(\omega) = \frac{2}{\pi}\left(\frac{k_B T m\omega_o}{Q}\right) \tag{3-48}$$

where the subscripts T denotes thermal noise. Similar to Eq. (2-23), the noise displacement spectral density due to noise driven amplitude $x_b(t)$ is given by

$$S_x^T(\omega_{osc}) = \frac{S_{fn}}{m^2(\omega_o^2 - \omega_{osc}^2)^2 + (2\zeta\omega_o\omega_{osc})^2} \tag{3-49}$$

$$S_x^T(\omega_{osc}) = \frac{2k_B T}{\pi m Q}\left(\frac{\omega_o}{(\omega_o^2 - \omega_{osc}^2)^2 + (2\zeta\omega_o\omega_{osc})^2}\right) \tag{3-50}$$

Eq. (3-50) represents frequency distributed displacement noise and only half the total power is associated with phase modulation; the other half is associated with amplitude modulation. In applications where frequency output is measured by counting zero-crossing, error due to amplitude modulation can simply be ignored. We can now calculated the phase noise due to thermal-mechanical motions from Eq. (3-50). Phase noise mathematically can be expressed as ratio between amplitude noise and mean amplitude and is given by Eq. (3-51).

$$S_\phi^T(\omega_{osc}) = \frac{1}{2}\frac{S_{xnt}(\omega_{osc})}{|X(\omega_{osc})|^2} \tag{3-51}$$

For an offset frequency $\Delta\omega = \omega - \omega_{osc}$ such that $\omega_{osc}/Q << \Delta\omega << \omega_{osc}$, the off-resonance phase noise reduces to

$$S_\phi^T(\omega) \approx \frac{k_B T}{4\pi m Q\omega_{osc}\Delta\omega^2|X(\omega_{osc})|^2} \tag{3-52}$$

We define the mean amplitude of oscillation by stored energy at ω_o as $E_c = 1/2.m\omega_o^2|X(\omega_{osc})|^2$. The energy dissipated per cycle due to the finite Q needs to be provided externally to maintain the oscillation. This input power is equal to $P_{in} = E_c\omega_o/Q$. Eq. (3-52) can now be reduced to

$$S_\phi^T(\omega) \approx \frac{k_B T}{8\pi P_{in} Q^2}\left(\frac{\omega_{osc}}{\Delta\omega}\right)^2 \tag{3-53}$$

Eq. (3-53) is identical to expression given in [116] and defines the ultimate sensitivity for a resonant sensor. However the contribution of other noise sources is significantly much larger than thermal noise limits; thereby degrading the sensitivity.

3-10-2 Displacement detector noise

The deflection of the membrane cannot be measured by infinite precision but is subjected to the noise induced by the measurement setup. In addition to this, electrical noise injected by the amplifiers that converts the optical signals into voltage also decreases the sensitivity. In the closed loop optical system, the membrane starts to oscillate when

$$\phi(f) + \phi_{circuit}(f) = 2n\pi \tag{3-54}$$

where $\phi(f)$ is given by Eq. (2-5) and $\phi_{circuit}(f)$ is the additional phase added by the optical system and the electronics. Since the oscillating frequency is dependent on the total closed loop phase, any phase fluctuations in $\phi_{circuit}(f)$ can lead to shift in the frequency as shown in Figure 3-25. The shift is related to the slope of the graph which makes the situation worse in case of low Q systems (or at high pressure).

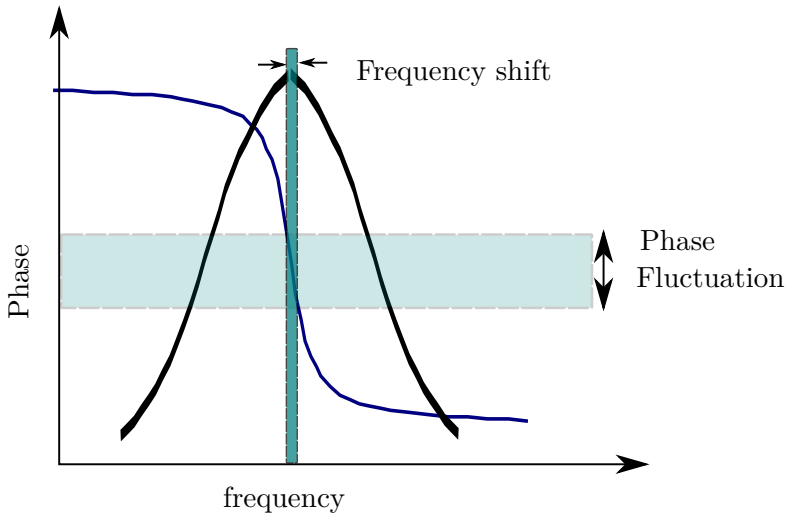

Figure 3-25: Schematic of evolution of frequency shifts due to phase fluctuations.

To estimate the phase variations, output voltage from the vibrometer can be written as

$$V_{out}(t) = \frac{1}{S_p^v} \frac{d[X(\omega_{osc})e^{i(\omega_{osc}t-\phi)} + \delta x_b(t)]}{dt} + \delta V \tag{3-55}$$

where S_p^v is the vibrometer's sensitivity (mm/s/V) and δV is the noise induced due to detection system. Given the constant velocity noise spectral density of sensor $S(v)$ $[(ms^{-1})^2/Hz]$, the output noise voltage can be written as

$$\delta V = \sqrt{S(v).B_f} \tag{3-56}$$

The above noise is equally divided into amplitude and phase noise. The detector induced phase noise can be written as

$$\langle S_\phi^D \rangle^2 = \delta\phi_{nd} = \frac{\delta V}{\langle V_{out} \rangle} \tag{3-57}$$

Since the variable velocity is uncorrelated, the induced phase noise spectral density S_ϕ^D can be considered as white phase noise.

3-10-3 Total Noise

From Eq. (3-57) and Eq. (3-53), the total phase fluctuation can be written as

$$S_\phi(\omega) = S_\phi^T(\omega) + S_\phi^D \tag{3-58}$$

$$S_\phi(\omega) = \frac{k_B T}{8\pi P_{in} Q^2} \left(\frac{\omega_{osc}}{\Delta\omega}\right)^2 + S_\phi^D \tag{3-59}$$

$$\delta\phi = \sqrt{S_\phi(\omega) B_f} \tag{3-60}$$

From Figure 3-25 we observe that for an self oscillating loop at ω_{osc}, the phase phase of the resonator is $\phi = -\pi/2$ and the frequency noise due to $\delta\phi$ is determined by the frequency derivative of the curve at $\phi = -\pi/2$ given by

$$\left(\frac{\delta\phi}{\delta\omega}\right)_{\omega_{osc}} = -\frac{2Q}{\omega_{osc}} \tag{3-61}$$

For offset frequency $\Delta\omega << \omega_{osc}/2Q$, the frequency noise due to $S_{\phi 1}^D$ can be equated to

$$S_{\omega 1}^D(\omega) = \left|\frac{\delta\omega}{\delta\phi}\right|^2 . S_\phi^D \tag{3-62}$$

while for $\Delta\omega >> \omega_{osc}/2Q$, the frequency noise is related to S_ϕ^D by the simple relation (frequency is the time derivative of phase)

$$S_{\omega 2}^D(\omega) = (\Delta\omega)^2 . S_\phi^D \tag{3-63}$$

The above relation is also valid for noise due to S_ϕ^T. The total frequency noise spectral density can now be written as

$$S_\omega(\omega) = \frac{k_B T \omega_{osc}^2}{8\pi P_{in} Q^2} + \left(\frac{\omega_{osc}}{2Q}\right)^2 S_\phi^D + (\Delta\omega)^2 S_\phi^D \tag{3-64}$$

The above equation has not considered the thermal noise of the amplifier which acts as the fourth source for frequency fluctuations. The evolution of displacement noise into oscillator frequency noise is represented in Figure 3-26. In absence of detector noise, the noise due to thermal motion in the range $\pm\omega_{osc}/2Q$ is shown in (a) which gets translated with a slope of $1/\Delta\omega$ according to Eq. (3-52) as shown in (b). The noise is converted into constant oscillator frequency noise when multipled by the bandwidth $\Delta\omega$ which is depicted in (c). The dash line shows the thermal noise due to measurement system. Contribution of the detector noise can be seen seperately in (d) and (e). (d) corresponds to constant oscillator noise in the range $\Delta\omega < \omega_{osc}/2Q$ in accordance with Eq. (3-62) while (e) represents the white phase noise for $\Delta\omega > \omega_{osc}/2Q$ according to Eq. (3-63) . The total noise (f) can be seen as the summation of three noise sources i.e. (d)+(e).

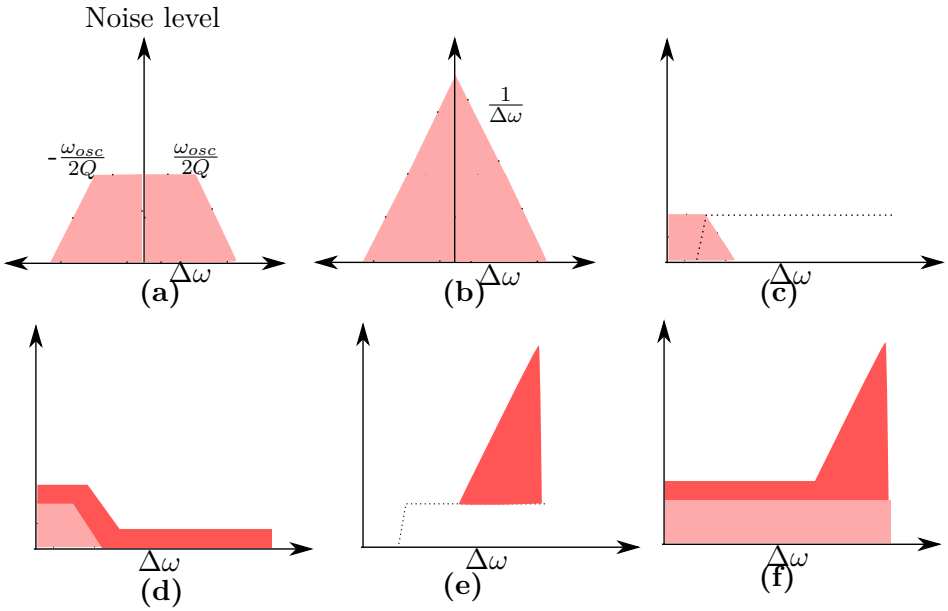

Figure 3-26: Schematic of evolution of frequency shifts due to phase fluctuations. (a)-(c) represents the thermal noise in the absence of detector noise. (d) represents the detector noise near the oscillation frequency according to Eq. (3-62) and (e) shows the upconoversion of detector noise according to Eq. (3-63). The total noise is shown in (f).

3-10-4 Allan Variance

A more useful quantity is Allan variance [117] which is used commonly to characterize the stability of oscillators in the presence of noise . It is defined as the average of sample variances between two adjacent fractional frequencies measured over a time interval of τ_A. Mathematically , the Allan variance $\sigma_A^2(\tau_A)$ can be written as

$$\sigma_A^2(\tau_A) = \left\langle \frac{(\bar{f_n} - \bar{f_{n-1}})^2}{2} \right\rangle \tag{3-65}$$

where $\bar{f_n}$ is the nth fractional frequency sample measured with a time span of τ_A and is given by

$$\bar{f_n} = \frac{1}{\tau_A} \int_t^{t+\tau_A} \frac{\delta f(t) dt}{f_o} \tag{3-66}$$

In practical situations, only a finite number of samples (M) are available for measuring the frequency sample f_n and Eq. (3-65) reduces to

$$\sigma_A^2(\tau_A) = \frac{1}{2(M-1)f_o^2} \sum_{n=2}^{M} (f_n - f_{n-1})^2 \tag{3-67}$$

The time-domain Allan variance is related to $S_\phi(\omega)$ in frequency domain by [118].

$$\sigma_A^2(\tau_A) = 2\left(\frac{2}{\omega_{osc}\tau_A}\right)^2 \int_0^\infty S_\phi(\omega) sin^4(\Delta\omega\tau_A/2) d\omega \tag{3-68}$$

This useful expression can be used to calculate Allan variance due to various phase noise spectral densities. For $1/f^2$ noise, using Eq. (3-68) and Eq. (3-53), we obtain

$$\sigma_A^2(\tau_A)_{1/f^2} = 2\left(\frac{2}{\omega_{osc}\tau_A}\right)^2 \int_0^\infty \frac{k_B T}{8\pi P_{in} Q^2} (\frac{\omega_{osc}}{\Delta\omega})^2 sin^4(\Delta\omega\tau_A/2) d\omega \tag{3-69}$$

$$\sigma_A^2(\tau_A)_{1/f^2} = \frac{k_B T}{\pi P_{in} Q^2 \tau_A^2} \int_0^\infty \frac{sin^4(\Delta\omega\tau_A/2) d\omega}{\Delta\omega^2} \tag{3-70}$$

$$\sigma_A^2(\tau_A)_{1/f^2} = \frac{k_B T}{\pi P_{in} Q^2 \tau_A^2} \frac{\pi\tau_A}{8} \tag{3-71}$$

$$\sigma_A^2(\tau_A)_{1/f^2} = \frac{k_B T}{8 P_{in} Q^2 \tau_A} \tag{3-72}$$

Allan variance for the second term in Eq. (3-64) gives us

$$\sigma_A^2(\tau_A)_{f^0} = 2\left(\frac{2}{\omega_{osc}\tau_A}\right)^2 \int_0^\infty \frac{S_\phi^D}{4Q^2} (\frac{\omega_{osc}}{\Delta\omega})^2 sin^4(\Delta\omega\tau_A/2) d\omega \tag{3-73}$$

$$\sigma_A^2(\tau_A)_{f^0} = 2\left(\frac{S_\phi^D}{Q^2\tau_A^2}\right) \int_0^\infty \frac{sin^4(\Delta\omega\tau_A/2) d\omega}{\Delta\omega^2} \tag{3-74}$$

$$\sigma_A^2(\tau_A)_{f^0} = \left(\frac{S_\phi^D}{Q^2\tau_A}\right) \frac{\pi}{4} \tag{3-75}$$

Similarly, the output Allan variance for 3rd term corresponding to f^0 white phase noise can be computed as

$$\sigma_A^2(\tau_A)_{f^0} = 2\left(\frac{2}{\omega_{osc}\tau_A}\right)^2 \int_0^\infty S_\phi^D sin^4(\Delta\omega\tau_A/2) d\omega \tag{3-76}$$

The above integral does not converge. For a given bandwidth B_f, Eq. (3-76) reduces to

$$\sigma_A^2(\tau_A)_{f^0} = 2\left(\frac{2}{\omega_{osc}\tau_A}\right)^2 \int_0^{B_f} S_\phi^D . sin^4(\Delta\omega\tau_A/2) d\omega \tag{3-77}$$

$$\sigma_A^2(\tau_A)_{f^0} = 2\left(\frac{2}{\omega_{osc}\tau_A}\right)^2 S_\phi^D \left(\frac{6\tau_A B_f - 8sin(B_f\tau_A) + sin(2B_f\tau_A)}{16\tau_A}\right) \tag{3-78}$$

For a bandwidth of 1 MHz and a minimum time of 20 μs we can assume that $B_f\tau_A >> 1$ following which the Allan variance is equal to

$$\sigma_A^2(\tau_A)_{f^0} = 2\left(\frac{2}{\omega_{osc}\tau_A}\right)^2 \frac{3.B_f S_\phi^D}{8} \tag{3-79}$$

Combining Eq. (3-79), Eq. (3-75) and Eq. (3-85), the frequency error given by Allan deviation can be written as

$$\sigma_A(\tau_A) = \sqrt{\frac{k_B T}{8 P_{in} Q^2 \tau_A} + \frac{\pi S_\phi^D}{4Q^2\tau_A} + \frac{3 S_\phi^D B_f}{\omega_{osc}^2 \tau_A^2}} \tag{3-80}$$

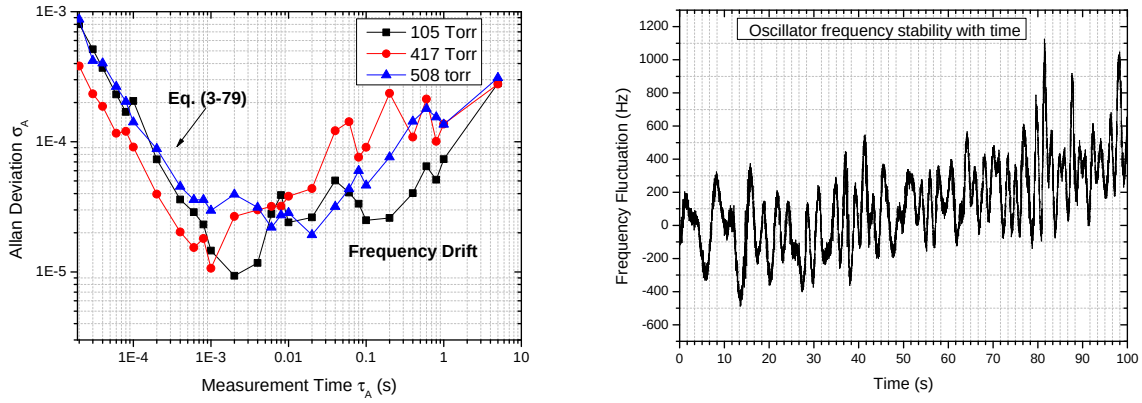

Figure 3-27: Allan deviation at 3 pressures measured vs measurement time. The effect of frequency drift can be seen at higher values of τ_A as shown in (b).

Figure 3-27a shows the measured Allan Deviation using Fluke PM6681 RF counter. At lower measurement time we see σ_A decreasing with τ according to Eq. (3-79) but at higher values of measurement time, we see that error gets accumulated and is proportional to τ^m where $m > 0$. This is due to the unintended progressive frequency drift [119] due to various effects like aging, change in temperature, voltage regulation or Doppler shift due to the motion of the sample. For $m = 1$, the shift is known as linear drift, for $m = 2$, it becomes quadratic drift and for higher values of m, it is known as random-walk. Figure 3-27b shows the progressive drift in the measured frequency with time.

Of particular area of interest is the region with low τ where $m < 0$. To find the exact value of m, we fit the curve with the equation $\sigma = n\tau^m$ for various pressures as shown in Figure 3-28.The extracted parameters n and m for different values of pressure are tabulated in Table 3-4. Since $m \approx -1$, it can easily be assumed that $\sigma_A(\tau_A) \propto 1/\tau_A$ i.e. the 3^{rd} term in Eq. (3-80) is much higher than the 1^st and 2^nd term. We can thus conclude that the dominating source of error is from the displacement sensor. Neglecting the error due to thermal noise, the Allan deviation can be approximated to

$$\sigma_A(\tau_A) \approx \frac{1}{\tau_A}\sqrt{\frac{3S_{\phi nd}B_f}{\omega_{osc}^2}} \tag{3-81}$$

where

$$n \approx \sqrt{\frac{3S_{\phi nd}B_f}{\omega_{osc}^2}} \tag{3-82}$$

The phase fluctuations are seen to be independent of the ambient pressure. During our experiment, a different minimum DC bias point and gain was set to have the system into oscillation which gave us different signal amplitudes at every pressures. According to Eq. (3-57), we expect different phase error with different signal amplitudes. To characterize the phase noise of the LDV system, we perform an open loop excitation of the MEMS resonator and measure the phase between the excitation signal and the output of the AGC block to

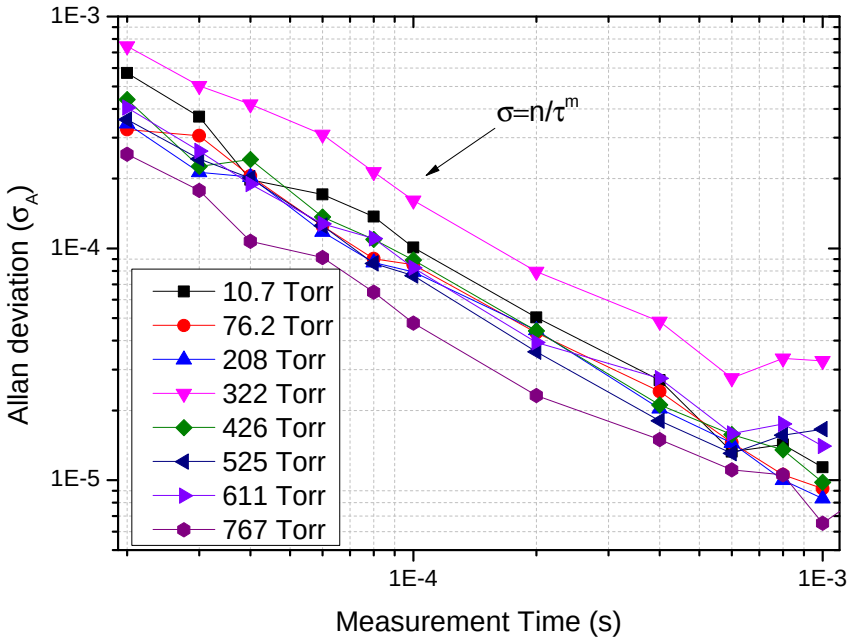

Figure 3-28: Allan deviation for low τ. Table 3-4 shows the linear fit parameters obtained

Table 3-4: Extracted parameter from power fit for Figure 3-28

Pressure	n Figure 3-28	m Figure 3-28	f_{osc} Figure 3-21	B_f	$S_{\phi nd}$ Eq. (3-82)	$\delta\phi$ Eq. (3-60)
10.7 Torr	2.51353E-9	1.13868	559427.549699 Hz	1 MHz	1.0489e-13	0.04^0
76.2 Torr	3.20602E-8	0.86095	566893.414708 Hz	1 MHz	1.752e-11	0.6^0
208 Torr	1.48446E-8	0.92798	582396.775956 Hz	1 MHz	3.965e-12	0.28^0
322 Torr	4.95737E-8	0.88896	594668.11927 Hz	1 MHz	4.610e-11	0.97^0
426 Torr	8.18512E-9	1.00238	612529.970579 Hz	1 MHz	1.333e-12	0.16^0
525 Torr	1.14234E-8	0.95773	625313.026396 Hz	1 MHz	2.706e-12	0.23^0
616 Torr	8.25232E-9	0.99674	635074.813835 Hz	1 MHz	1.457e-12	0.17^0
767 Torr	4.33487E-9	1.01489	656122.918377 Hz	1 MHz	4.291e-13	0.09^0

experimentally estimate the phase fluctuations due to the LDV. Figure 3-29 shows the noisy output signal from the LDV when excitated with a frequency of 655 kHz measured from the oscilloscope output. A phase fluctuation of $\mathbf{0.756}^0$ was obtained which corresponds to a spectral density of $\mathbf{2.772e\text{-}11\ rad^2/Hz}$ which corresponds to the extracted values from Table 3-4. The selected velocity decoder used in our measurement **VD-09-20 mm/(s.V)**. For a peak amplitude of **1.5 V**, the output noise voltage due to detector is approximately **0.0131 V** over a bandwidth of **1 MHz** or noise velocity of **266** $\mu m/s$, which gives us an experimental estimation of the noise spectral density equal to **0.28** $\mu s^{-1}/\sqrt{Hz}$. For the reported velocity noise density (reference to user manual for OFV 5000) of S_v = 0.02-0.25 $\mu s^{-1}/\sqrt{Hz}$, theis is close to the upper limit for the reported value and justifies the measurement results.

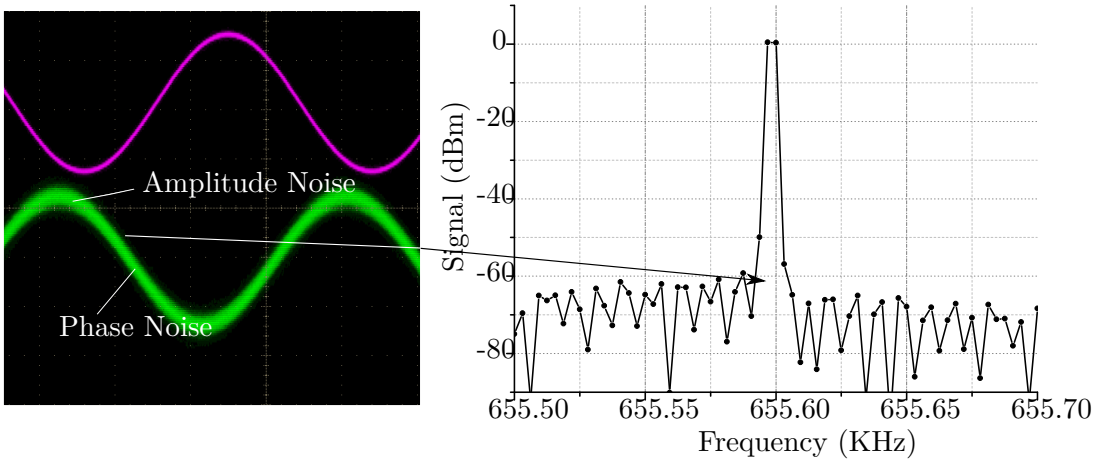

Figure 3-29: (a) Comparison with the input and noisy output signal for a open loop characterization of LDV+AGC. (b) Frequency spectrum of the output signal broaden around the peak frequency.

3-10-5 Frequency Error and Resolution

From Eq. (3-46) and Eq. (3-47), we can write the minimum detectable pressure change equal to

$$\delta p_{min} = \delta\omega \frac{dp}{d\omega} \tag{3-83}$$

where

$$\delta\omega = \sigma_A . \omega_{osc} \tag{3-84}$$

With an extracted slope of S=97.16 kHz/bar from Figure 3-21 and allan deviation measured in Figure 3-28, the resolution as a function of measurement time is shown in Figure 3-30.

The resolution in pressure measurement is limited by the noise injected from the LDV. In the absence of LDV induced noise, the displacement sensitivity can be calculated from Eq. (3-85)

$$\sigma_A^2(\tau_A)_{1/f^2} = \frac{k_B T}{8 P_{in} Q^2 \tau_A} \tag{3-85}$$

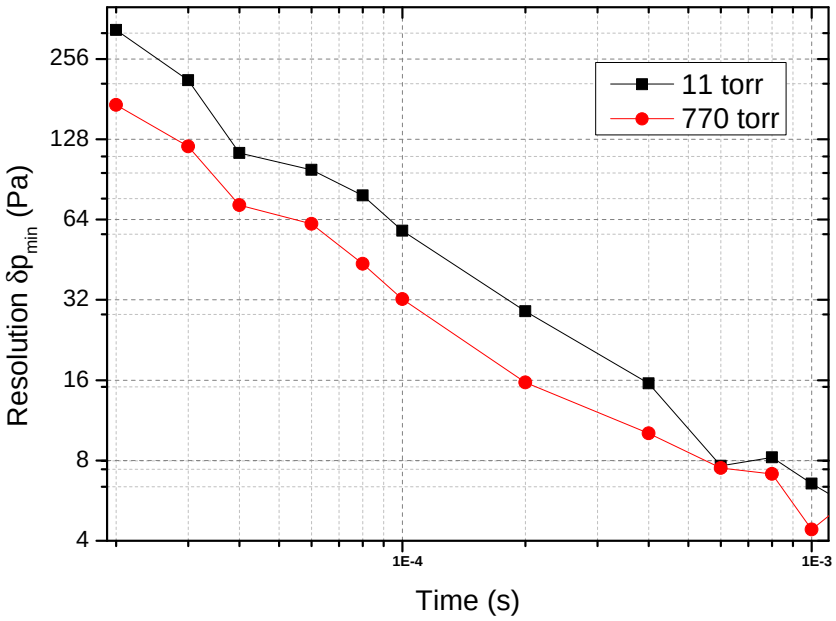

Figure 3-30: Resolution of the opto-electronic system with different measurement time.

where P_{in} can be written as

$$P_{in} = \frac{1}{2} m \omega_o^2 |X_{osc}|^2 \frac{\omega_{osc}}{Q} \tag{3-86}$$

or (Eq. (3-31))

$$P_{in} = \frac{1}{2} m v^2 \frac{\omega_{osc}}{Q} \tag{3-87}$$

The resolution of the oscillator due to thermal noise of the resonator is hence limited to

$$\delta p_{min}^T = \sigma_A . \omega_{osc} \frac{dp}{d\omega} \tag{3-88}$$

$$\delta p_{min}^T = \sqrt{\frac{k_B T f_o}{8\pi m v^2 Q \tau_A}} \frac{dp}{d\omega} \tag{3-89}$$

For two different pressures, Table 3-5 list all the required parameters to obtain the thermal noise limited resolution. In the absence of LDV induced noise, for a detected peak velocity from the LDV equal to 0.1 m/s, the thermal noise limited pressure resolution as depicted in Figure 3-31 shows a difference of 3 orders of magnitude.

Although the allan deviation is a function of ω_{osc} according to Eq. (3-80) or the approximated Eq. (3-67), we observe no dependence on pressure. It should be mentioned that Eq. (3-80) ignores the thermal noise due to the oscillator electronics and amplifier which is independent on pressure which could be comparable to the noise due to optical detection system. A

Table 3-5: Parameters used in Eq. (3-89)

	11 Torr	770 Torr	
f_{osc}	559 kHz	656 kHz	Figure 3-21
Q	3650	50	Figure 3-9
m	3.67e-09 kg	3.67e-09 kg	Eq. (3-19)
v	0.1 m/s	0.1 m/s	Measured with LDV

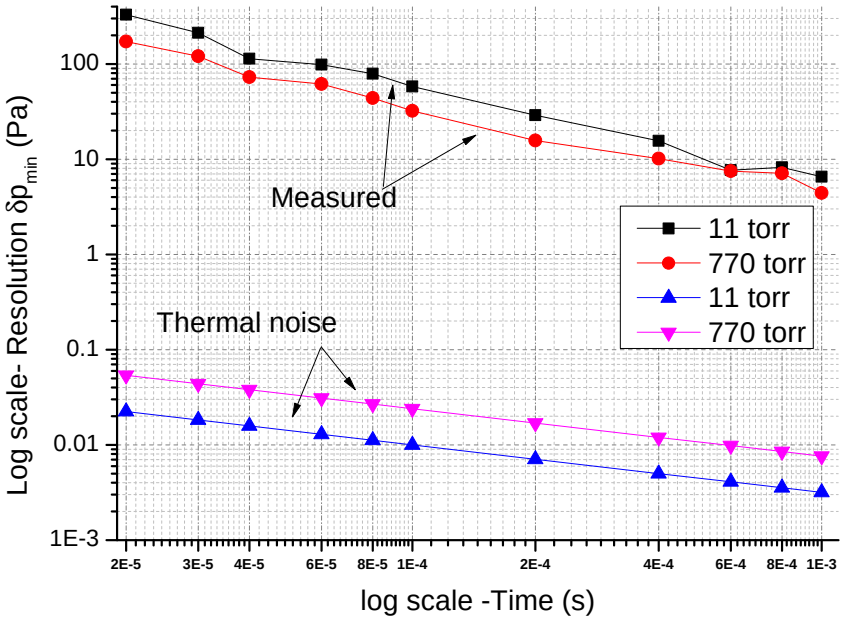

Figure 3-31: Comparison of measured resolution with resolution limited by the thermal-mechanical noise.

minimum resolution of 5 Pa can be obtained from the proposed opto-electronic MEMS oscillator whereas the fundamental limit is estimated to be as low as **0.003 Pa**. This corresponds to a frequency shift of 5 Hz around the resonance. However, Figure 3-27b shows that frequency error due to drift noise is almost 500 Hz which makes the system not suitable for pressure sensing. The drift is assumed to be due to the instability and the time delay in the optical measurement system and external environmental interferences. In terms of resolution, accuracy and stability, the optical system limits the performance of MEMS device as a pressure sensor. From application point of view, optical systems are generally not used and instead electrical oscillators using MEMS device can be used as pressure sensor. The next chapter evaluates the performance of electrical oscillators and opto-electronic oscillators to have a better understanding and comparison.

Chapter 4

Quartz resonators : Electrical vs opto-electronic oscillators

In the previous chapter we discussed that the resolution of the MEMS opto-electronic oscillator pressure sensor was limited by the detector noise from the Laser Vibrometry. Other noise sources such as oscillator feedback noise from the gain control circuitry and thermal noise were far less dominating and did not effect the sensor's sensitivity. For commercial applications however, an electronic MEMS oscillator is more suitable for its small size, lower power consumption and simplicity when compared to the bulky opto-electronic system. The long-term frequency drift and instability further makes the system incapable of resonant sensing. Electrical MEMS oscillators are seen to exhibit $1/f^3$ noise near carrier roll-off due to the up-conversion of $1/f$ flicker noise [43] along with white noise which limits the performance of the sensors. Based on transduction principle, piezoelectric and capacitive MEMS oscillators are most commonly used. In terms of noise performance, capacitive MEMS oscillators gives lower phase noise than piezoelectric oscillators at a fixed frequency. This is due to the fact that capacitive resonators exhibit high Q, whereas piezoelectric resonators show a lower Q due to losses associated with the integrated piezoelectric layers. For a frequency of 1 MHz (closest to our frequency of 660 kHz from the past literature), capacitive resonators shows a noise floor of -88 dBc/Hz at an offest frequency of 500 Hz [120] while piezoelectric resonators exhibit a phase noise of -100 dBc/Hz at 1 kHz offset [121]. This is five orders of magnitude lower than our measurement results (-55-60 dBc @ 1 kHz, see Figure 3-24). In practice, today's best MEMS oscillator have a much better noise performance of -135 to -140 dbc/Hz [122], [123].

The opto-electronic oscillator eliminates the effect of shunt capacitor C_o (Figure 3-6) as it directly measures the velocity of the resonating membrane. For electrical oscillators however, the conditions Eq. (3-1) and Eq. (3-2) imposes a restriction given by Eq. (3-32) i.e.

$$R_m \leq \frac{1}{2\omega_o C_o} \tag{4-1}$$

The system will not oscillate if R_m is large or C_o is large. Since R_m is a function of DC bias (Figure 3-8), the system can be made to oscillate by tuning V_{dc}. Figure 4-1 shows the

estimated DC bias required as a function of pressure. It was foreseen that it would therefore be difficult to create an electrical oscillator with the MEMS device. A high DC voltage up to 45 V is required at 764 Torr which might lead to device breakdown.

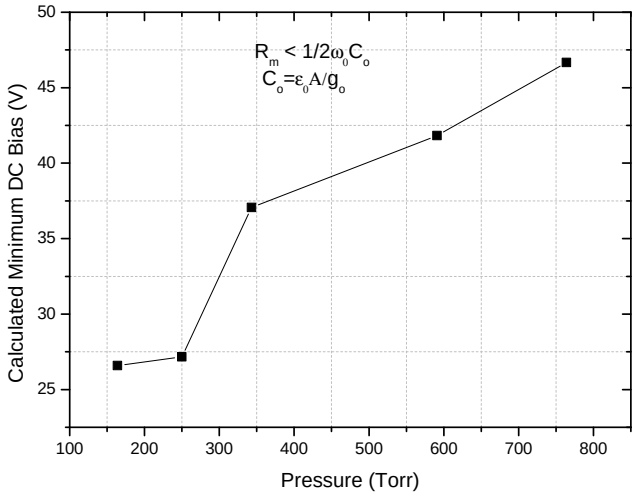

Figure 4-1: Estimated DC bias required as a function of pressure for the MEMS resonator to oscillate Eq. (4-1).

To compare the performance of electrical and opto-electronic MEMS oscillators, we therefore use the most widely used quartz crystal (found commonly in wrist watches) with an operating frequency of 32.768 kHz and has the same electrical equivalent as that of a MEMS resonator.

4-1 Quartz Tuning fork resonators

A Quartz resonator is essentially a capacitor where SiO_2 acts as a dielectric that exhibits piezoelectric properties. A part of the electrical energy stored within the capacitor is converted into mechanical energy. The energy conversion equations for MEMS resonators can also be applied to quartz resonators resulting in an identical equivalent electrical model as shown in Figure 2-6. This feature makes them quite attractive because they simply need to be connected to an electronic signal source to get the resonator into excitation mode. Different shapes and size of quartz resonator leads to different modes of oscillation. A quartz resonator split into two parallel bars and supported at it's foot is known as tuning fork (Figure 4-2). The tiny 32.768 kHz tuning fork has become a standard for most electronic watches and has found many applications [124] due to their small size, low cost and low power consumption.

Unlike conventional harmonic oscillators discussed in chapter two, the dynamics of a tuning fork can be understood by considering it as a coupled oscillator as shown in Figure 4-3. The two identical prongs with spring constant k are coupled with a spring constant k_c leading to two different modes of oscillation - in-phase and out-of-phase mode. Solving the equation of harmonic oscillators for individual prongs leads to respective eigenmode frequencies given by [125]

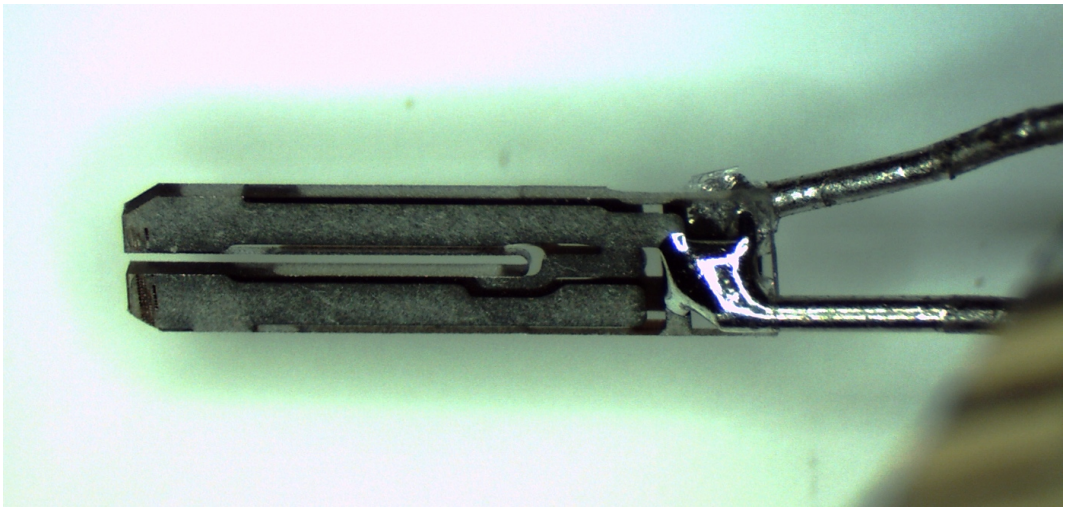

Figure 4-2: A typical 32 kHz quartz tuning fork. Metal electrodes deposited on each prong generates electric field when excited with a voltage source. This effect results in flexural motions of the prong in the plane of tuning fork.

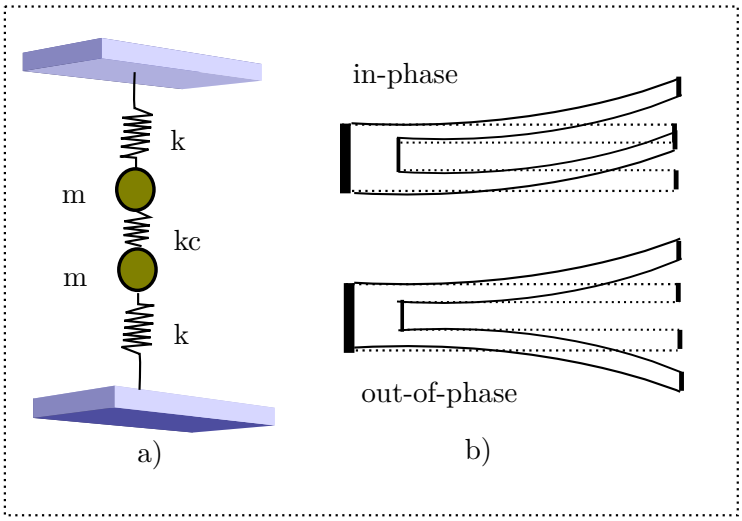

Figure 4-3: (a) Spring-mass model for a tuning fork as a coupled oscillator resonating in two possible modes as shown in (b).

$$f_o^{in-phase} = \frac{1}{2\pi}\sqrt{\frac{k}{m}} \tag{4-2}$$

$$f_o^{out-of-phase} = \frac{1}{2\pi}\sqrt{\frac{k+2k_c}{m}} \tag{4-3}$$

Considering the two prongs to be identical, the effective spring constant is given by

$$k_{eff} = 2(k + 2k_c) \tag{4-4}$$

The coupling spring constant k_c effectively affects the difference in the two eigen frequencies. Stiffness of a typical spring constant is around 1800 N/m which provides an efficient means of confining the acoustic energy in the prongs and so tuning forks are able to achieve very high Qs (typical values $\approx 10^5$). This combined with stable small oscillation amplitudes [126] enables the detection of small frequency shifts around f_o, resulting in highly sensitive measurements.

4-2 Dynamics of tuning fork

Various media in contact with the vibrating tuning fork creates mechanical perturbations which can lead to changes in resonance characteristics like frequency or motional resistance. In order to use tuning forks as sensors, it is necessary to co-relate its electrical response to the external loading parameters. The effect of air loading has been studied quite extensively [127], [128] earlier. The Q change is similar to MEMS resonator and is inversely proportional to pressure. However, becasue of the absence of an air gap, the mechanism for the shift in resonant frequency is not squeeze film damping as discussed in chapter 2. It is very well established that the shift in the frequency response is due to the interaction between the vibrating resonator and the ambient gas molecules. The drag force generated by the molecules is given by [129]

$$F = A\frac{dx}{dt} + B\frac{d^2x}{dt^2} \tag{4-5}$$

where A and B are the coefficient based on 'string-of-bead' model of quartz resonator [130]. The parameter B is significant because the second term of Eq. (4-5) has an acceleration term which means that the mass of the resonator increases from m to m+B i.e. there is an apparent increase in effective mass of the vibrating object which shifts the resonance frequency to

$$\omega = \sqrt{\frac{k}{m+B}} \tag{4-6}$$

and B is given by

$$B = 3\pi R^2\sqrt{\frac{2\eta\rho_{air}}{\omega}} + \frac{2}{3}\pi R^3\rho_{air} \tag{4-7}$$

where

R = radius of the sphere from the bead model theory
η = coefficient of viscosity

$$\rho_{air} = \text{gas density}$$

Using series expansion and ignoring the higher order terms, Eq. (4-6) can be written as

$$\omega \approx \frac{k}{m}\left(1 - \frac{B}{2m}\right) \tag{4-8}$$

$$\omega \approx \omega_o\left(1 - \frac{B}{2m}\right) \tag{4-9}$$

where ω_o is the frequency when pressure approaches 0. Th angular frequency shift for a quartz tuning fork now is given by

$$\frac{\Delta\omega}{\omega_o} \approx -\frac{B}{2m} \tag{4-10}$$

i.e. with increasing pressure, the resonance frequency of the tuning fork decreases and Q decreases. Figure 4-4 shows the frequency response of tuning fork at different pressures.

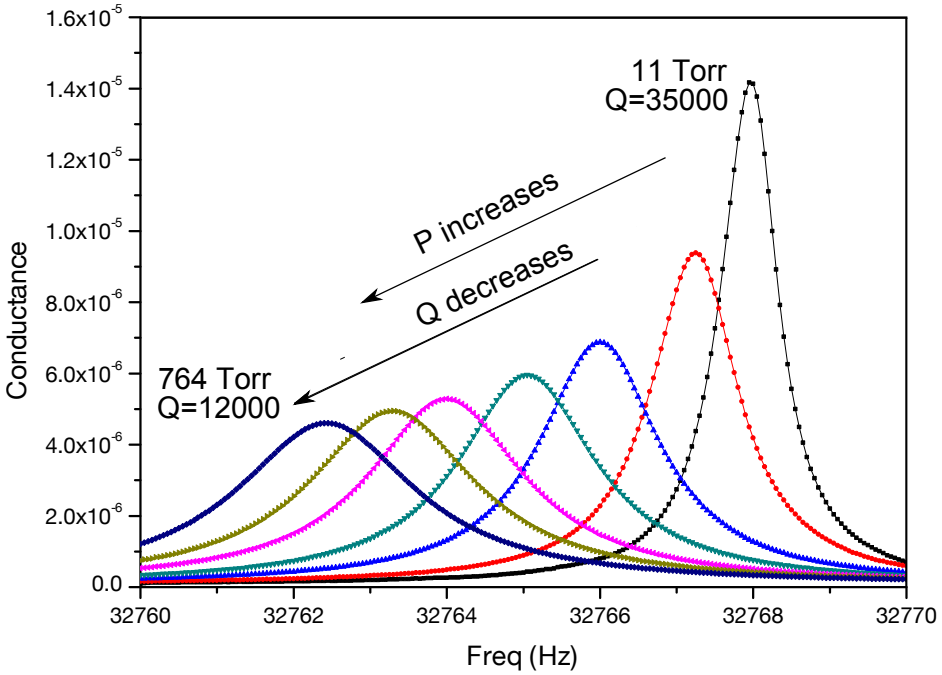

Figure 4-4: Measured frequency response of tuning fork at different pressures by an impedance analyzer. The ac peak excitation signal value was set to 100 mV. The resonant frequency shifts towards lower frequency with increasing pressure while the dependence of Q shows a similar behavior as that for MEMS resonator.

Since the change in the resonant frequency is very small (1 Hz), it is reasonable to assume that ω in Eq. (4-7) is equal to ω_o. In case of 32.8 kHz crystal, for pressures more than 10 torr, the frequency vs pressure is a linear response and it can be concluded that the second term is larger than the first term. Eq. (4-10) now reduces to

$$\frac{\Delta\omega}{\omega_o} \approx -\frac{1}{2m}\left(\frac{2}{3}\pi R^3 \rho_{air}\right) \tag{4-11}$$

$$\frac{\Delta\omega}{\omega_o} \approx -\frac{1}{4}\left(\frac{\rho_{air}}{\rho_{crystal}}\right) \tag{4-12}$$

where we have used the relation $m = 4/3.\pi R^3.\rho_{crystal}$. Clearly, the shift is directly dependent on the surrounding gas density which in terms of pressure can be written as

$$\rho_{air} = \frac{p}{R_{dryair}T} \tag{4-13}$$

where p and R are pressure and specific gas density. Using the above equation, the theoretical sensitivity is given by

$$\frac{df}{dp} = -\frac{1}{4}\frac{\omega_o}{R_{dryair}T\rho_{crystal}} \tag{4-14}$$

For R=287.058 J/(Kg.K), T=300 K and $\rho_{crystal}$ =2660 Kg/m^3, we obtain a slope of **3.6 Hz/bar** which is close to experimental result of **5.85 Hz/bar** as shown in Figure 4-5.

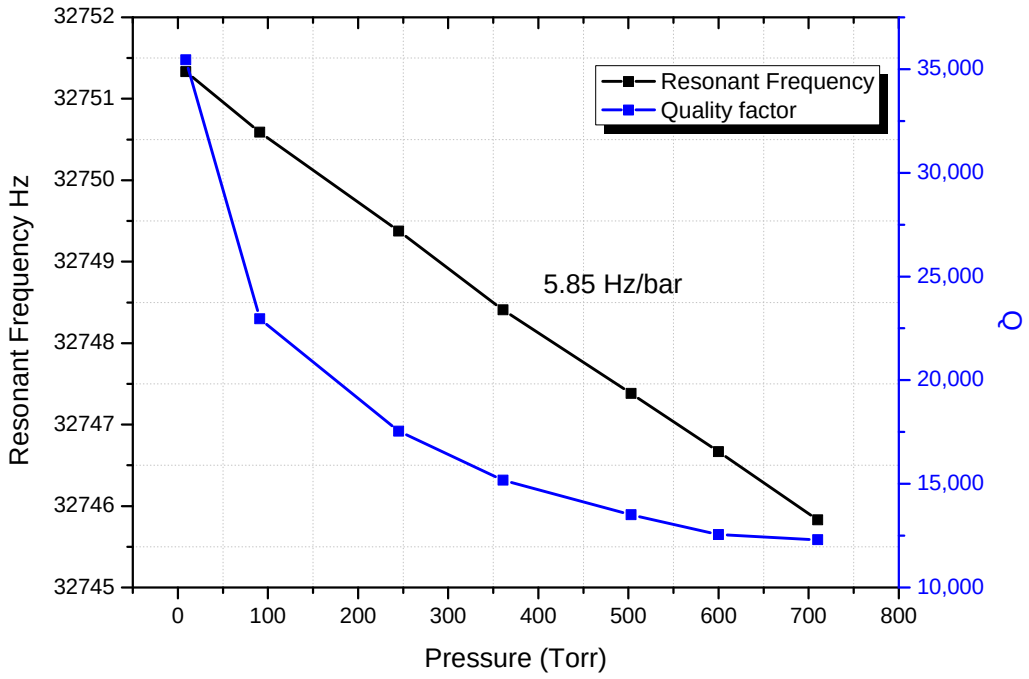

Figure 4-5: Resonant frequency vs pressure shows a negative slope of -**5.85 Hz/bar**. The Q however changes from 32000 to 12000 and is much more sensitive to pressure suggesting that viscous damping is the major loss mechanism.

Electrically, the effect of air loading can also be understood in terms of its RLC parameters where R, L and C represents acoustic losses, mass and spring constant respectively. The air molecule interactions can be electrically modeled as an additional RLC element in series [131] as shown in Figure 4-6.

To prove the above model, we extract the electrical parameters by curve fitting the conductance and phase response at different pressures. From Figure 4-7, we observe that R_m and L_m have increased while C_m has decreased at higher pressure. Of all the parameters, R_m

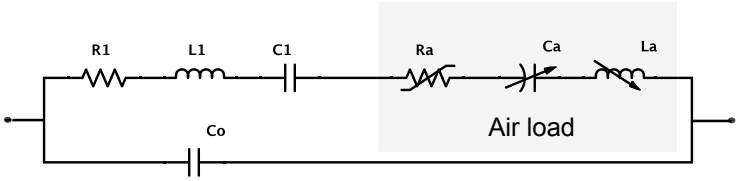

Figure 4-6: Equivalent circuit diagram of an air loaded tuning fork.

shows significant change with changing pressure which indicates higher losses and lower Q. The increase in L_m relates to the apparent increase in the effective mass of the resonator. The decrease in C_m can be explained by the fact that motional C_A due to air acts in series with unloaded C_m, thereby decreasing the net value. The high value of parasitic shunt capacitor also includes external wiring capacitors connected to the tuning fork.

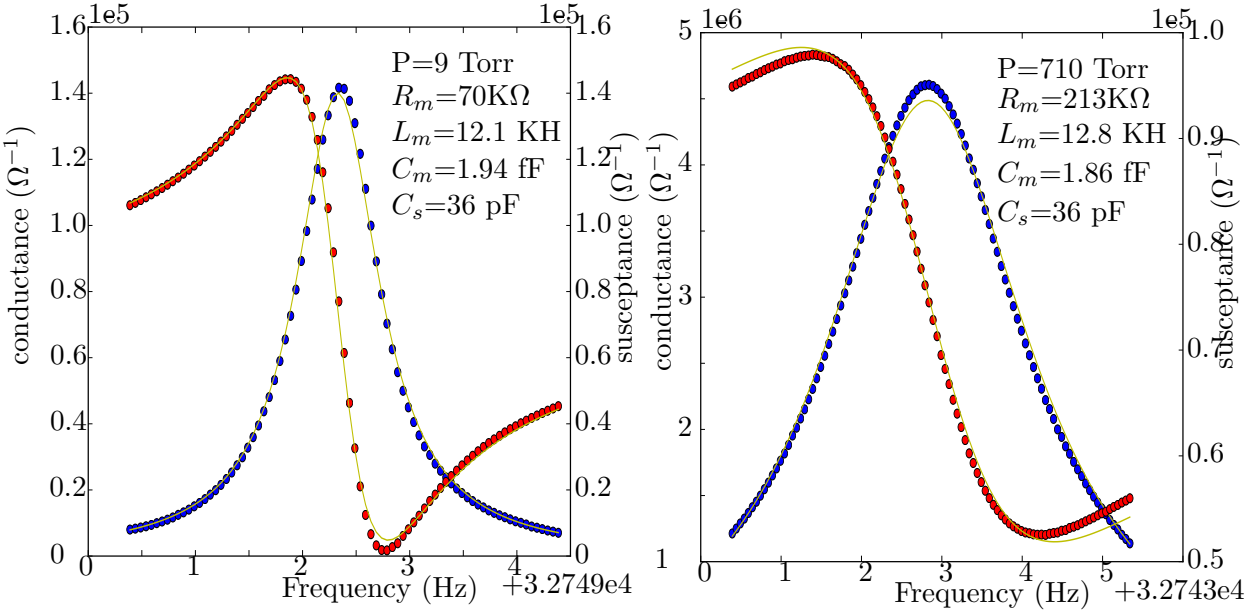

Figure 4-7: The real (conductance) and imaginary (susceptance) part of admittance measured with an impedance analyzer. The yellow line is obtained from the curve fit algorithm to extract RLC parameters.

4-3 Tuning fork oscillator as pressure sensor

4-3-1 Opto-electronic configuration

Similar to section 3-7, we drive the tuning fork into oscillation using optical feedback through LDV as shown in Figure 4-8. Due to a very stable oscillation amplitude and high value of Q, the automatic gain control as well as the phase shifter were not used. The laser beam was directed at one end of the tuning fork to detect the peak velocity response which was converted into electrical signals by the vibrometer with a gain of 50 mm/s/V. To suppress

the higher harmonics, the internal 20 kHz low pass filter was used. A sinusoidal oscillating signal with an output frequency of 32 kHz was measured with the RF counter.

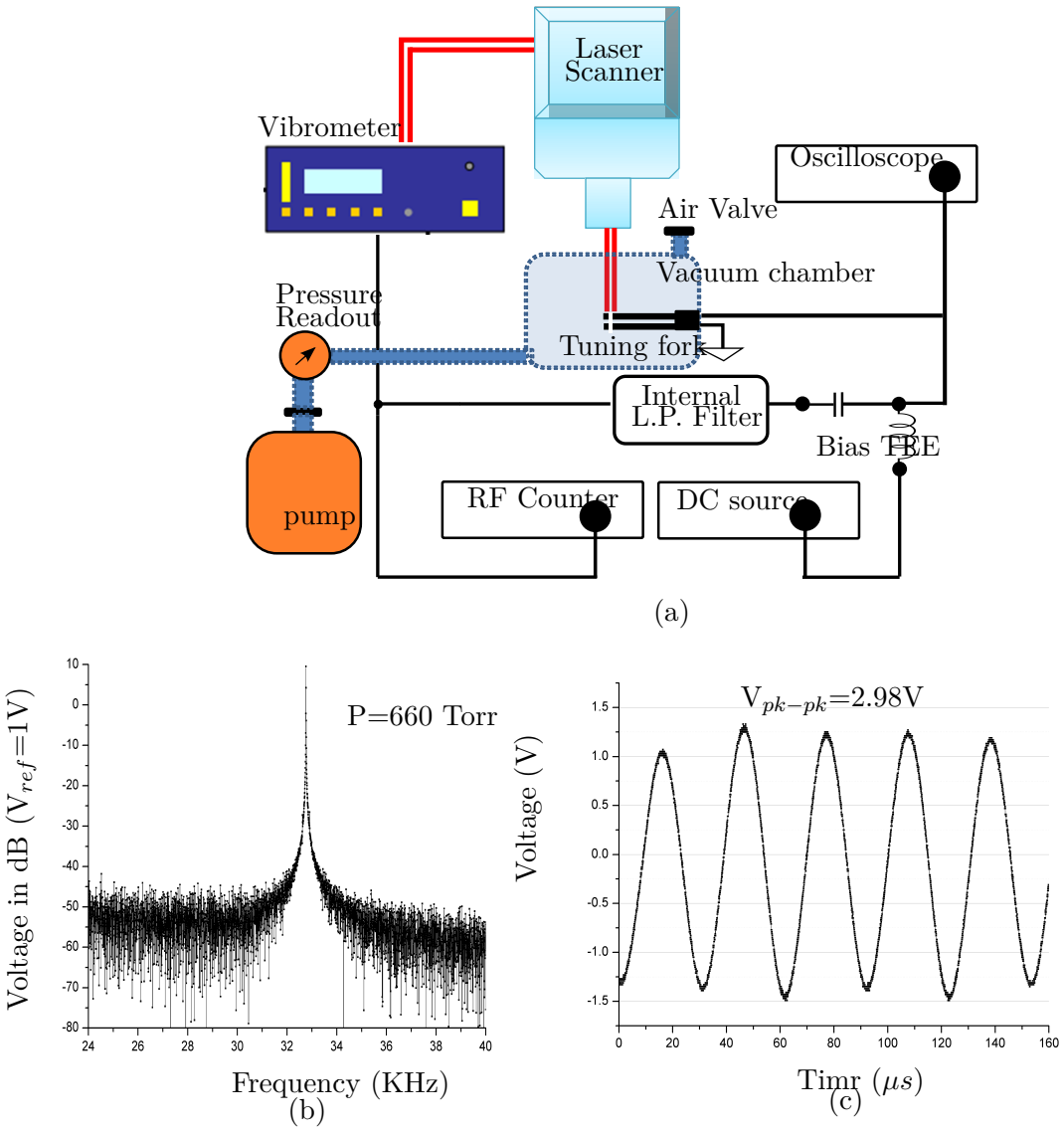

Figure 4-8: (a) Experimental setup for the opto-electronic tuning fork oscillator.(b) The output frequency spectrum with a frequency of 32.764 kHz at a pressure of 660 Torr .(b) the corresponding ac signal with 2.98 V pk-pk as measured by the oscilloscope .

4-3-2 Electrical Pierce oscillator

The tuning fork can be made to oscillate if it is connected in a positive feedback loop with a closed loop gain of more than 1. With no other frequency sensitive component in the loop, the circuit oscillates at tuning fork's resonant frequency. From circuit theory, the output frequency is dependent on L_m and C_m which is known as series resonant frequency $\omega_s = \frac{1}{\sqrt{L_m C_m}}$. The shunt capacitor C_o also gives a parallel resonance frequency [132] which is not as precise as

the other series RLC parameters. Crystals operate either at or near ω_s and parallel resonance simply implies that the crystal has a high load impedance across it's terminal. The parallel capacitor C_o merely acts as an external load to the circuit. The most common oscillator configuration is by far the Pierce oscillator but there are many other topologies as well [133]. The Pierce oscillator is a series resonant circuit shown in Figure 4-9. The circuit can work in a frequency range from 1 kHz to 200 MHz. The crystal's (X1) source and load impedance are mostly capacitive rather than resistive which gives a high internal Q and amplitude stability, not to mention a high output signal at a low power level. Large shunt capacitors to the ground also minimize noise spikes. It does however have one disadvantage. It needs a high amplifier gain to account for the losses in the circuitry surrounding the crystal.

The Circuit starts to oscillate when the total phase shift around the loop is 360^0 and gain $\geq$ 1. The npn transistor is connected in a common-emitter configuration which provides a 180^0 phase shift, C_3 and C_2 along with the crystal and external resistors acts as an integration network and provides a 90^0 phase lag each. At series resonance, the crystal's impedance is purely resistive, which combines with load capacitors and thereby provides the required phase shift. The high gain of CE amplifier ensures that the total loop gain is more than 1 in order to satisfy the oscillation criteria. The gain can be controlled by the collector and emitter resistance R_1 and R_4. R_2 and R_3 acts as a voltage divider for setting the bias voltage. For detailed analysis of Pierce oscillators, the readers are encouraged to refer to [134].

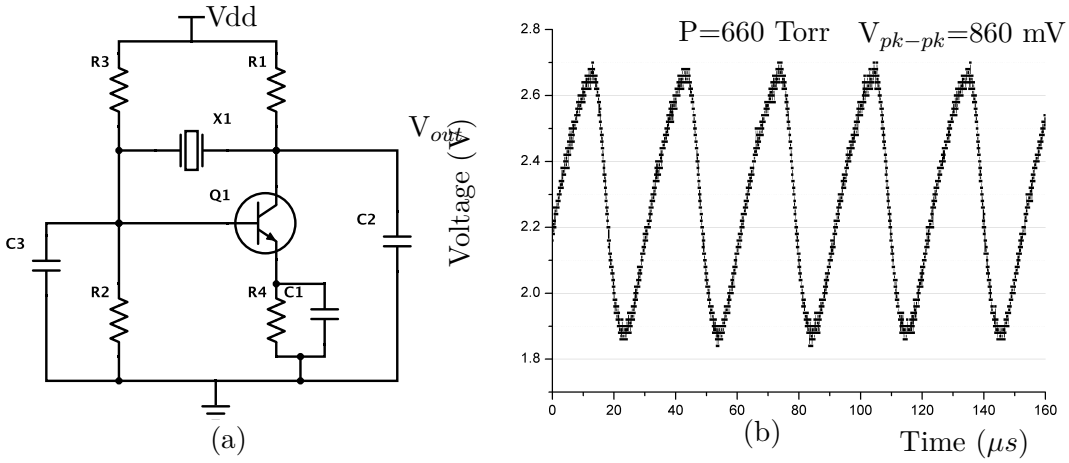

Figure 4-9: (a) Schematic of a common emitter Pierce crystal oscillator (b) Output sinusoidal waveform as measured at 660 Torr. With a DC bias of 3.94 V, a pk-pk signal of 860 mV was measured.

We place both the Pierce and opto-electronic crystal oscillator inside the vacuum chamber for simultaneous readout of output frequency at different pressures. The measured results are shown in Figure 4-10. In reality, the phase shift from the CE amplifier is less than 180^0 due to intrinsic junction capacitance. Same holds for the optical system where the phase shifts can be due to the delay in the LDV optical signal path. As such, we observe a difference in the frequency output of both the oscillators.

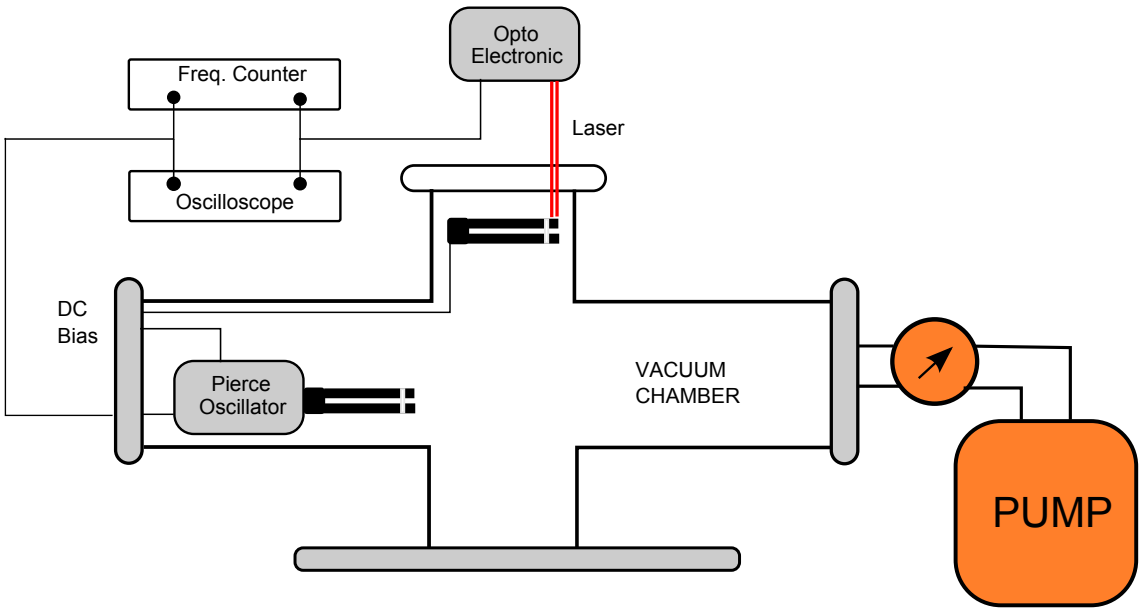

(a)

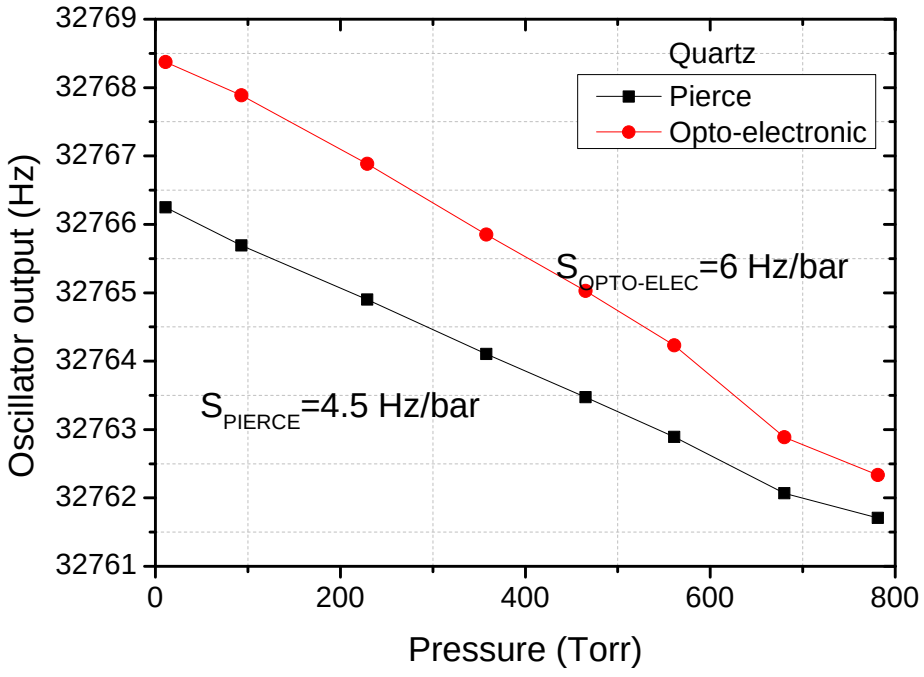

(b)

Figure 4-10: (a) Experimental setup for characterization of quartz oscillators. (b) Resonant frequency vs pressure for Pierce and opto-electronic oscillator. We observe a pressure sensitivity of **4.5 Hz/bar** for Pierce oscillator and **6 Hz/bar** for opto-electronic system.

4-4 Frequency stability and performance

Similar to the MEMS resonator, the tuning fork oscillations are also subjected to noise which defines the resolution of the sensor. Except for the displacement detector noise, all other sources of noise, namely thermal white noise, oscillator feedback induced noise and frequency drift noise are common to both types of oscillators. The phase noise spectral density due to thermal motions has already been discussed in chapter three and is equal to

$$S_{\phi}^{T}(\omega) \approx \frac{k_B T}{8\pi P_{in} Q^2} \left(\frac{\omega_{osc}}{\Delta\omega}\right)^2 \tag{4-15}$$

where

$$P_{in} = \frac{v_{in}^2}{R_m} = \frac{v_{out}^2}{G^2 R_m} \tag{4-16}$$

where G is the gain of the common emitter amplifier in case of Pierce oscillator or the velocity decoded gain from the LDV vibrometer. To characterize all other sources of noise, we measure the Allan Deviation as shown in Figure 4-11.

Similar to the Allan deviation measured for the MEMS oscillator, the noise has no dependance on pressure. The frequency noise for opto-electronic oscillator is found to be proportional to τ_A^{-1} (curve fitting parameter yields a power of m= 0.98) suggesting that the dominant noise source is white phase noise due to the optical system and the thermal noise of the oscillator electronics. Using the similar approach mentioned in chapter 3, we estimate a spectral noise density $S_{\phi}^{D} = 9.58 \times 10^{-9}$. For the Pierce oscillator, we observe regions proportional to τ_A^{-1} ($\tau_A < 0.01s$), τ_A^0 (at higher measurement time) and an intermediate $\tau_A^{-0.5}$ slope suggesting the presence of White phase noise (or flicker phase noise), white frequency noise and flicker frequency noise respectively (Figure 4-12(a)) . Regressive curve fitting can lead to the spectral noise densities according to the cutler equation [118]. For higher measurement times i.e. $\tau_A > 0.1s$, it can be seen from Figure 4-12 that Pierce oscillator shows a dependence of τ_A^0 indicating the presence of flicker frequency noise while for opto-electronic system shows random walk effect due to noise sources (τ_A^m where m >0). The response is similar to MEMS opto-electronic oscillator.

With all the possible frequency dependent and white noise, the frequency error in Pierce oscillator is observed to be 2 orders of magnitude smaller than opto-electronic oscillator. This difference is also translated into minimum pressure resolution achievable. For a low external pressure of 11 torr, the minimum Allan deviation ($\delta f/f_o$) measured at τ_A= 60 ms is equal to

$$\left(\frac{\delta f}{f_o}\right)_{opto-electronic} = 1.65 \times 10^{-5}$$
$$\left(\frac{\delta f}{f_o}\right)_{pierce} = 6.55 \times 10^{-7}$$

which using Eq. (3-83) gives us a pressure resolution of

$$\delta p_{opto-electronic} = 9KPa \tag{4-17}$$

$$\delta p_{pierce} = 456Pa \tag{4-18}$$

The resolution of electrical oscillator is **20 times** better than opto-electronic oscillator as shown in Figure 4-13. In absence of LDV noise, white phase noise, flicker noise and white

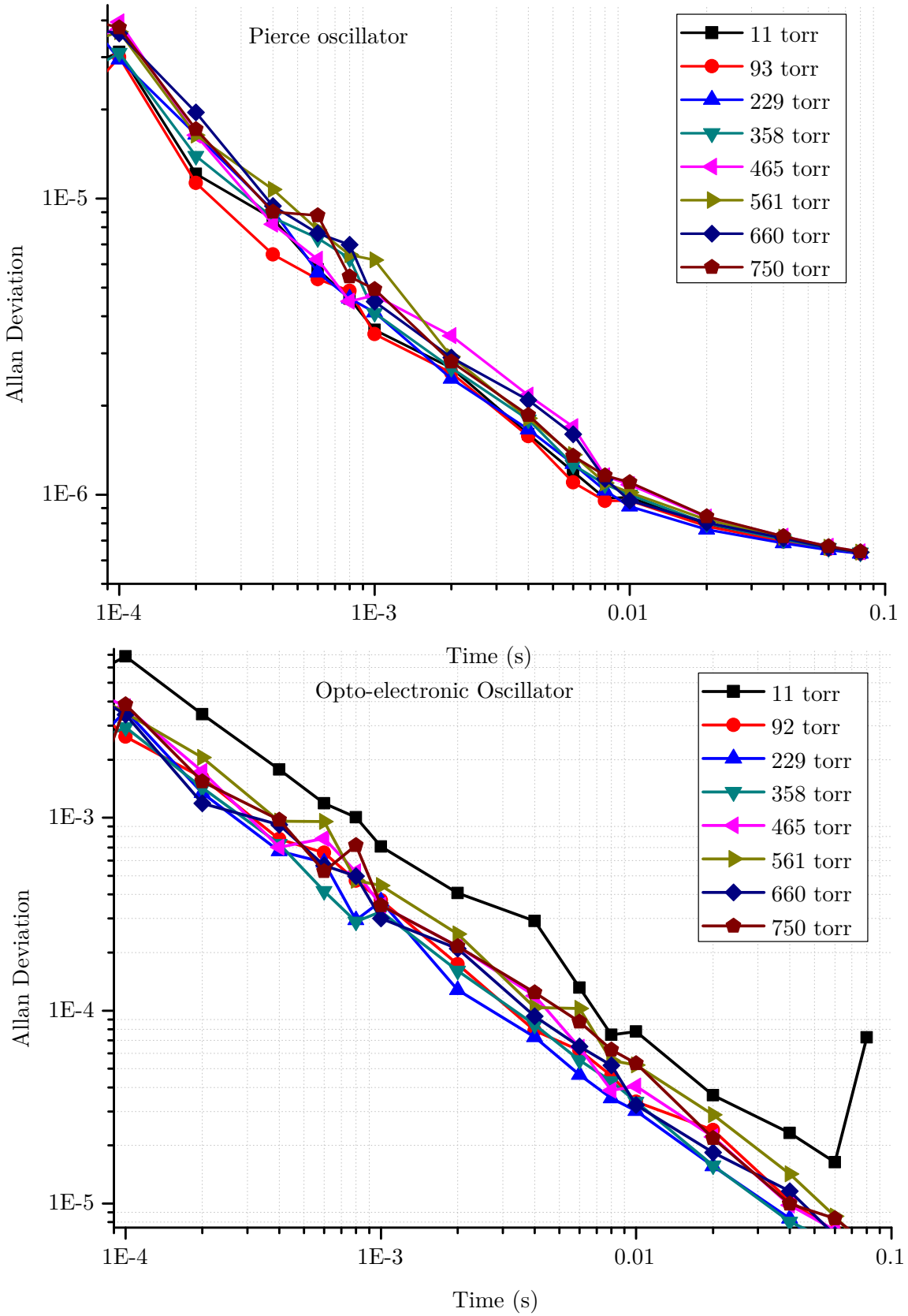

Figure 4-11: Allan deviation verses measurement time for different values of pressure. In terms of frequency stability, Pierce oscillator is almost 100 times better than opto-electronic oscillator.

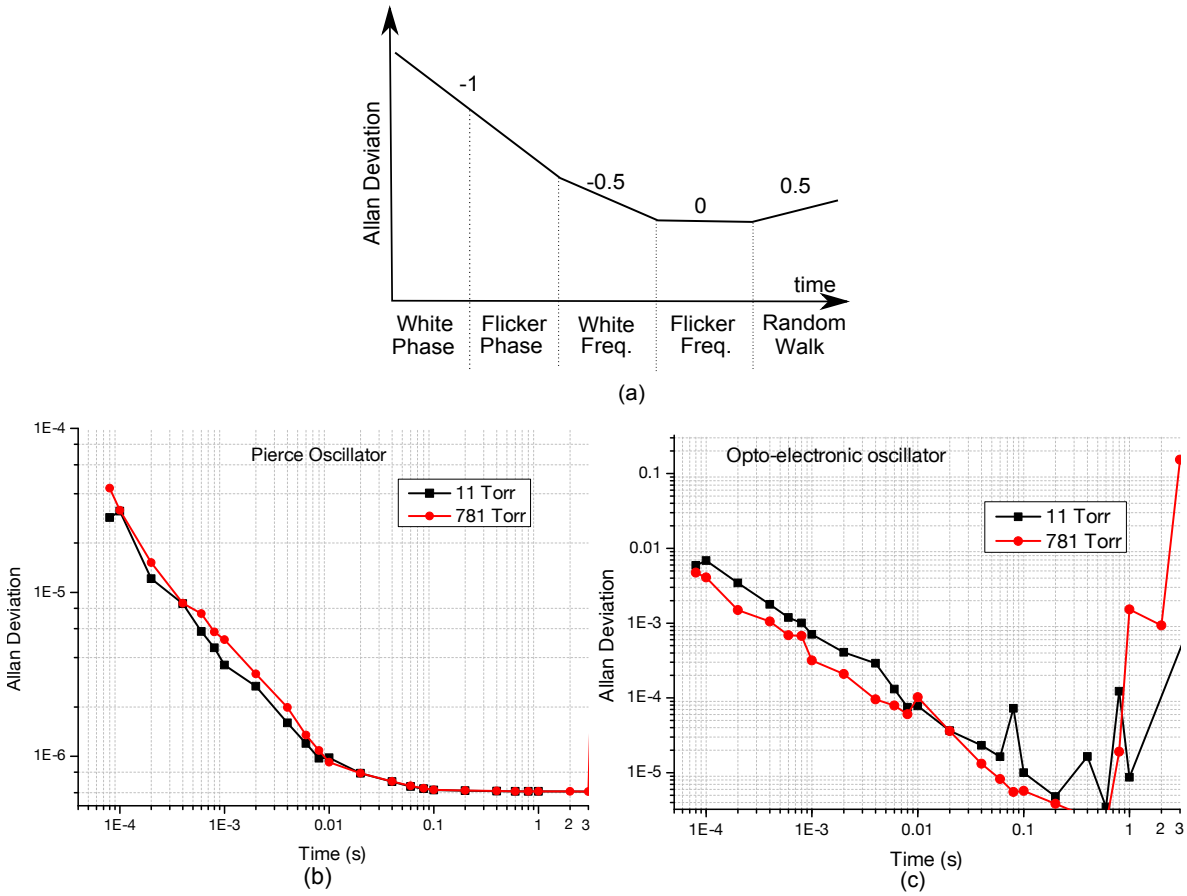

Figure 4-12: Allan deviation at low and high pressures for (b) Pierce oscillator (c) opto electronic oscillator measured vs measurement time. (a) represents the allan deviation due to various types of noise sources. Note that for a slope of τ^{-1}, allan deviation is unable to distinguish between white phase and flicker phase noise. The effect of frequency drift can be seen at higher values of τ_A.

frequency noise, Eq. (4-15) sets the fundamental limit for sensitivity of the tuning fork as a pressure sensor. The frequency error due to the resulting noise induced jitter can be estimated as [135]

$$\delta f_{thermal} = f_o \sqrt{\frac{k_B T B_f}{P_{in} Q^2}} \tag{4-19}$$

where

$$P_{in} = \frac{V_{out}^2}{G^2 R_m} \tag{4-20}$$

Here G is the open loop gain for each oscillator. The above equation is similar to Eq. (3-85) with $B_f = 1/\tau_A$. For an output ac signal of 840 mV at 11 torr (Q=35000), an amplifier gain of 80, R_m of 70KΩ and a bandwidth of 250 kHz, the fundamental limit at room temperature (300 K) leads to a pressure resolution of **27 Pa** for Pierce and **21 Pa** for opto-electronic mode. The frequency error however due to other possible noise sources far exceeds this fundamental limit. For transistor based Pierce topology, shot noise sources associated with collector and base current, flicker noise (1/f) and noise sources due to emitter degeneration resistors (R4)

leads to increase in the output phase noise [136]. For opto-electronic configuration, we can conclude that the displacement detector noise (white phase noise from the laser vibrometer) is the dominant source of noise.

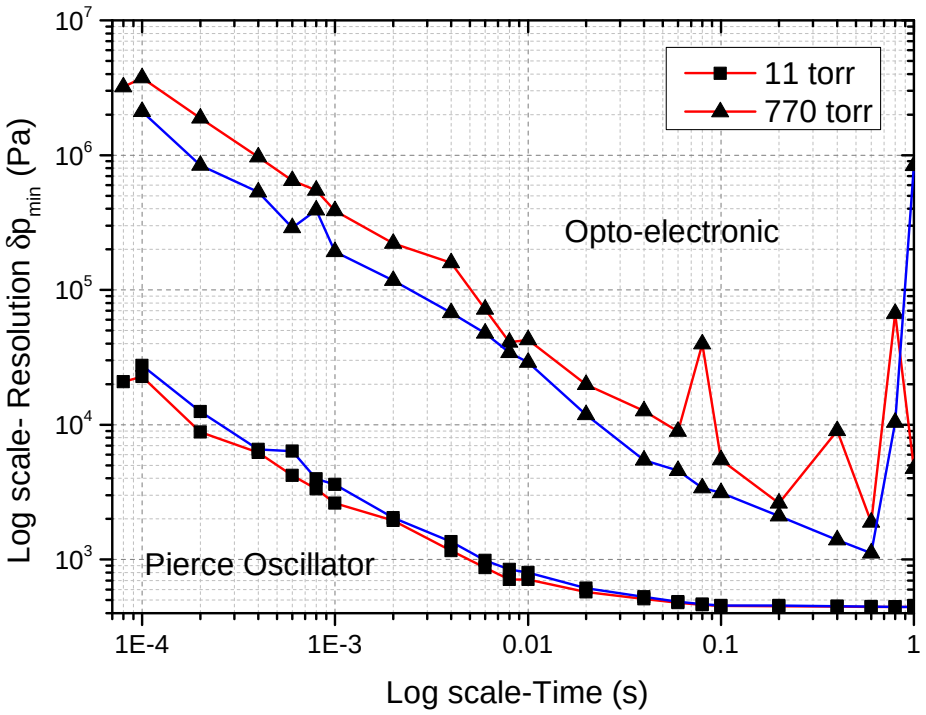

Figure 4-13: Calculated pressure resolution vs measurement time for Pierce and opto-electronic oscillator at two different pressure using Figure 4-12.

The feasibility of oscillators as resonant sensors is dependent on the frequency stability. In case of continuous monitoring of frequency, long term frequency drift arising due to temperature fluctuations (thermal drift) or external perturbations such as random walk (f^n noise sources) especially in the optical setup can lead to incorrect data acquisition during read-out. As done previously, we continuously monitor the output frequency for 2 hours. Figure 4-14 shows the long term frequency stability for both the oscillators.

In terms of frequency stability, we record a stability of $\pm$ **0.3 ppm** for Pierce oscillator and $\pm$ **300 ppm** for opto-electronic oscillator. Based on frequency stability and frequency noise, tuning fork based Pierce oscillator is **1000 times** stable and offers a pressure resolution which is **20 times** better than opto-electronic oscillator. Although tuning fork are not very sensitive to pressure (5 Hz/bar), MEMS resonators with a sensitivity of 97 kHz/bar can be used as pressure sensing elements. Opto-electronic oscillators suffer from high frequency noise and instability, but based upon the comparison result for tuning fork, MEMS based electrical oscillator (Pierce or other topologies) are expected to perform better than MEMS opto-electronic oscillator.

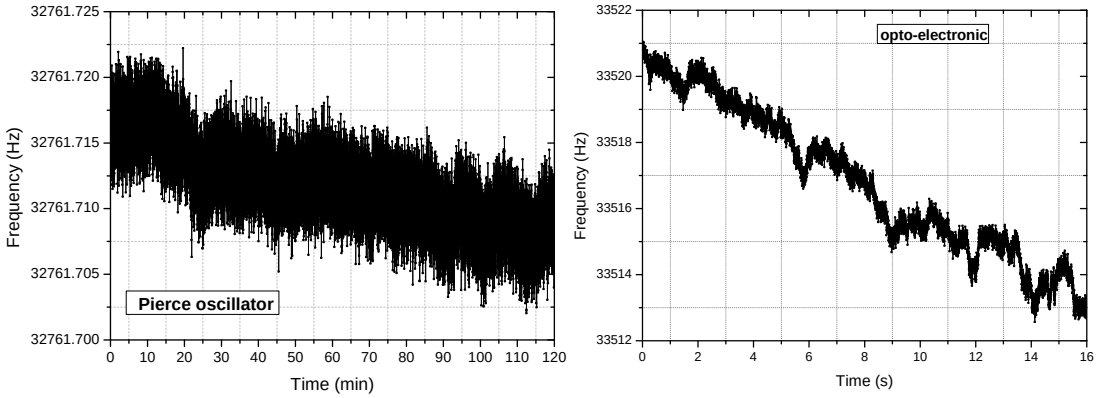

(a) **(b)**

Figure 4-14: Frequency output for (a) Pierce oscillator (b) opto electronic oscillator measured with a time interval of 1 ms. The corresponding frequency fluctuations are 10 mHz and 10 Hz .

Chapter 5

Evaluation and perspective

The research described in the previous chapters is driven by the need to develop high performance MEMS pressure sensors. The pressure sensor market is currently dominated by piezoresistive and capacitive sensing technology. For these two technologies, the need for integrated materials and additional layers adds to the fabrication complexity while signal conditioning and signal conversion reduces the simplicity of read-out electronics. Resonant sensing is fairly a new technique and the concept has been used for sensing mass, acceleration, temperature, displacement and even molecular interactions with 'state of the art' resolutions and superior performances. As such, MEMS resonant sensors also hold potential for pressure sensing which has not been explored for commercial applications so far. The fabrication process for resonant sensing is comparatively lower and the output signal in the frequency domain simplifies the read-out electronics but continuous monitoring of resonant frequency requires continuous excitation and detection of MEMS device. As such, a self oscillating MEMS resonator for pressure sensing has been proposed as a proof of concept to attain better resolution, stability and higher performance compared to existing sensor technologies.

5-1 MEMS opto-electronic oscillator

Compared to conventional MEMS oscillator with different possible excitation and detection principles, an oscillator concept using electrostatic actuation and optical detection is presented. The closed loop for sustained oscillation is created by optical feedback using Laser Doppler Vibrometry (LDV). The LDV measures the velocity of the electrostatically actuated membrane which is subsequently converted into electrical signal by a suitable velocity decoder. The optical system here is used both for optical detection and as a sustaining amplifier. Based on the vast literature on MEMS oscillator, this approach has not been explored and presented so far. Opto-electronic topology is preferred because,

- Requirement for extra amplification is eliminated. The losses at lower Q or higher pressure can be compensated by regulating the DC bias source.

- No on-chip integration of diffused resistors, piezoelectric layers or charge storage is required for actuation and detection techniques.
- The optical read-out is a non contact detection technique which eliminates the effect due to parasitics and shunt capacitor C_o, which otherwise imposes restrictions to a stable feedback loop and oscillation criteria.
- The principle can be extended for rapid characterization of on-wafer MEMS devices for oscillation frequencies in research environments. The system can be used for comparison of MEMS sensor design and to estimate sensor's amplitude during operation.
- With a frequency output, the optical system can be used for resonant pressure sensing which has been explored extensively in this work.

For a MEMS resonator to be sensitive to external pressure, a circular membrane with a center perforation is used. This makes the pressure on both sides of the membrane equal thereby enabling absolute pressure measurements. The squeeze film damping mechanism is responsible for a pressure dependent frequency shift. With MEMS resonator as a frequency sensitive element in a closed feedback loop, we obtain a pressure sensitivity of **97.16 kHz/bar** similar to open loop measurement. Gain and phase control circuit were implemented to reduce the oscillator noise. We obtain a minimum resolution of **5 Pa** with a measurement time of **1 ms** at atmospheric pressure. The white phase noise from the velocity decoder limits the highest resolution possible. The system is able to detect a frequency shift of $\approx$ **5 Hz** which requires a frequency stability of $\pm$ **8.33 ppm** at an output frequency equal to **600 kHz**. The measured frequency stability in our case is estimated to be around $\pm$**900 ppm** which corresponds to a frequency shift of 500 Hz. The reasons behind the frequency instability of the opto-electronic system is still unknown. The output is observed to be quite sensitive to external interferences due to the open laboratory setup. The signal delay between the optical receiver and the vibrometer is reported to be **8.9** μs or **100 kHz** which is comparable to the output frequency and can cause significant errors in phase and frequency. A small amount of phase lag is also added which is reported to be **-3.2**^{0} **/kHz** which corresponds to **0.003**^{0} over a bandwidth of 1 MHz. Hence, even though the self oscillating MEMS resonator is quite sensitive to external pressure, the resolution and accuracy/stability is limited by the LDV which makes an opto-electronic oscillator not suitable for resonant sensing applications. For commercial applicability, optical signals are usually not preferred due to size, cost and complexity involved. It would be fair to conclude that pressure sensing using an all-electrical MEMS oscillator can overcome the drawbacks of opto-electronic oscillators.

5-2 Electrical vs opto-electronic oscillators

To compare the performance of opto-electronic oscillator with electrical oscillator, a tuning fork crystal operating at 32.768 kHz was configured in both oscillator topologies. AGC and phase shifter were removed from the opto-electronic configuration due to stable signal amplitudes and high Q ($\approx 10^4$) associated with tuning forks. For electrical configuration, widely used pierce topology was used because of it's simplicity and superior noise performance. Similar to MEMS opto-electronic topology, the Allan deviation showed detector noise from the LDV to be the dominant noise source while pierce oscillator showed various noise sources

corresponding to white PM, white FM, flicker PM and flicker FM. Since LDV is the dominant detector noise, Allan deviation for both tuning fork and MEMS based opto-electronic oscillator were observed to be of the same order of magnitude. Table 5-1 and Figure 5-1 compares the performance of both the oscillator topologies.

Table 5-1: Comparison between tuning fork based self-oscillating pressure sensors.

Topology	Noise ($\delta f/f$)	Accuracy	Resolution	Sensitivity
Opto-electronic	10^{-5}	$\pm$ 300 ppm	9000 Pa	6 Hz/bar
Electrical (Pierce)	10^{-7}	$\pm$ 0.3 ppm	450 Pa	4.5 Hz/bar
Improvement factor	100	1000	20	-

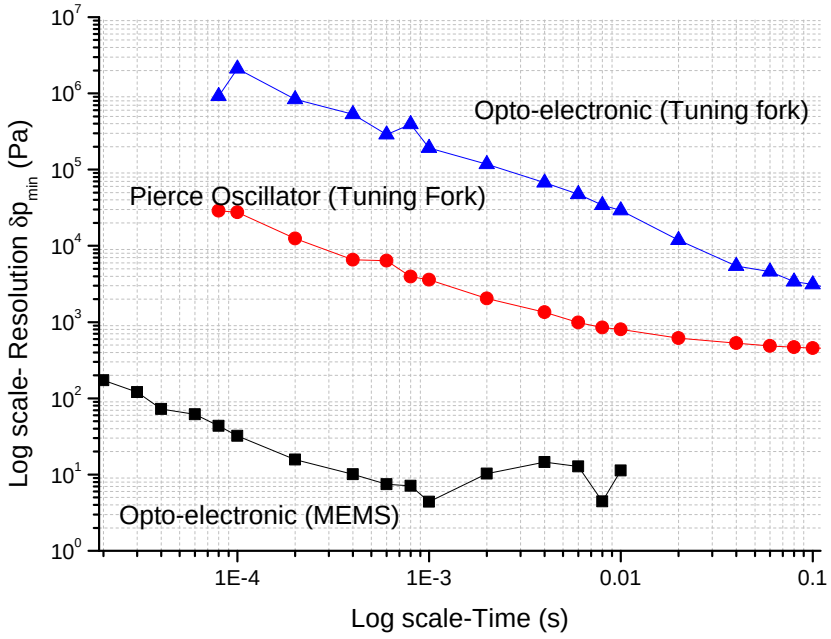

Figure 5-1: Comparison of resolutions obtained for 3 oscillators at atmospheric pressure

It is evident that electrical oscillators are far more superior than opto-electronic oscillators in terms of resolution as well as stability. MEMS Pierce oscillator or other similar all-electrical topology is expected to perform better and their commercial applicability is possible.

5-3 Competitive benchmark

In today's scenario, a vast majority of pressure sensors are based on piezoresistive effect. The principle has been used for over 50 years and now it is often preferred over other approaches due to it's technological maturity. However, compatibility to standard IC process

and feasibility in process development cannot be the only reason to consider. Excellent linearity, reliable signal conditioning and data acquisition, resolution, accuracy and precision are equally important. Certain parameters are also responsible for their success in a particular field of application i.e. For example, optical sensors are bulky, complex and consume high power but they are ideal for remote sensing applications in power lines, fuel tanks or for oil exploration. Over the last ten years, capacitive pressure sensors have shared space with piezoresistive sensors in the market for tire pressure monitoring, implantable medical devices, barometric sensors etc. They offer low power consumption, higher temperature insensitivity, high linearity and higher sensitivity. Looking back to Figure 5-1, MEMS devices are much more sensitive to pressure than quartz crystal. The Resolution is five orders of magnitude better than quartz sensors. However, quartz resonators have 100 times higher Q which means high stability and low power consumption. A fairly new technology has combined the advantages of both Quartz and MEMS by applying precision micro-processing on a quartz material and is known as QMEMS. Such ultra miniature quartz crystals controlled by semiconductor process shown in Figure 5-2 have been used as sensors for highly accurate and stable measurements. Currently QMEMS bases quartz sensing devices are used for timing applications, temperature sensors, gyroscope and pressure sensors.

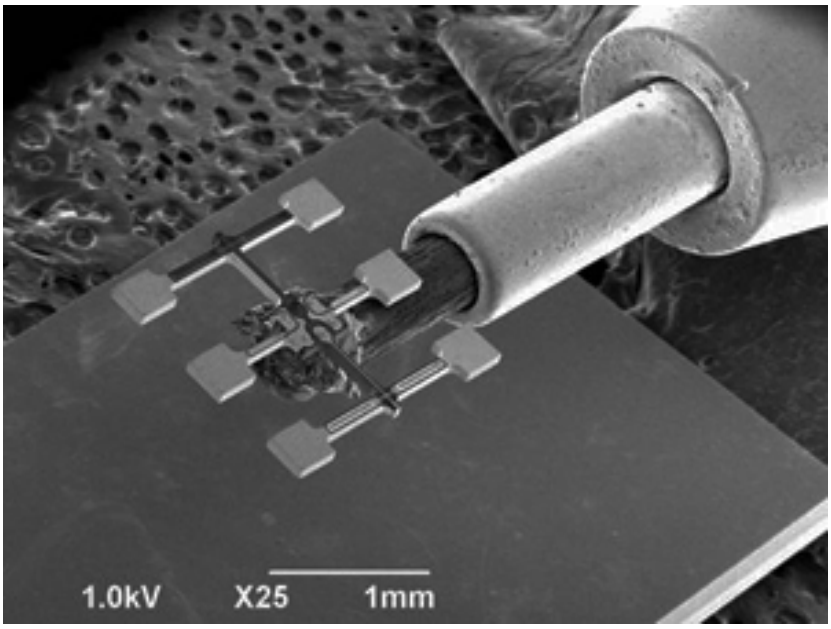

Figure 5-2: Highly sensitive gyro sensors using a hammerhead and H-groove structure produced with photo-lithography by Epson (Adapted from www. epsondevices.com).

The feasibility of MEMS oscillator as commercial pressure sensors can be studied from Table 5-2 which compares the performance of state-of-the-art pressure sensors. Using the improvement factor from Table 5-1, a hypothetical resolution of electrical MEMS oscillator equal to **0.2 Pa** can be estimated with an accuracy of $\pm$ **1 ppm**. The latter i.e. accuracy is however overestimated. For conventional piezoelectric or capacitive transduced MEMS oscillator, a typical accuracy is usually $\pm$ 20-50 ppm. The resolution (or the sensitivity) on the other hand can vary depending on the operating frequency. Oscillators operating at higher frequency usually exhibit low phase noise and can lead to better resolutions. However, high frequency

Table 5-2: Comparison between different self-oscillating pressure sensors

Topology	Noise ($\delta f/f$)	Accuracy	Resolution	Measurement time
MEMS opto-electronic	10^{-5}	± 900 ppm	5 Pa	1 ms
MEMS Electrical (hypothetical)	10^{-7}	± 1 ppm	0.2 Pa	-
Company	**Technology**	**Accuracy**	**Resolution**	**Measurement time**
Bosch Sensortec (BMP280)	Piezoresistive	± 10 Pa	2 Pa	13 ms
			1 Pa	25 ms
Murata (Mass production in Q4)	Capacitive	2 ± 10 Pa	Pa	83 ms
			0.5 Pa	1000 ms
Epson Toyocom (XP-6000CA)	QMEMS	± 30 Pa	0.3 Pa	800 ms
			1.2 Pa	200 ms
			2.5 Pa	100 ms

resonators tend to have a lower Q which can partly cancel the effect leading to phase noise reduction [43]. Oscillation frequency as high as 2 GHz for piezoelectric transduced oscillator [137] and 145 MHz for capacitive transduced oscillators [138] have been reported. Another factor to consider for resolution is the measurement time (or speed). A trade-off between these two parameters is evident from Table 5-2. A trade-off between speed and power consumption is yet another factor which must be taken into account. MEMS oscillators used for timing applications or as a sensor are sealed in a hermetic cavity to obtain high Q and low power. As such, the power consumption would be higher than the reported values when operated as a pressure sensor (especially at atmospheric pressure). It would be difficult to compare power consumption for various technologies due to lack of experimental data but in terms of resolution, accuracy, measurement time and sensitivity, self oscillating MEMS resonator certainly have a competitive potential for resonant pressure sensing.

5-4 Recommendations and future outlook

5-4-1 Reducing noise due to optical feedback

Of all the detection techniques discussed in Chapter 1 and 3 for sensing mechanical motion, optical interferometry gives the highest resolution. A displacement sensitivity of 1 fm/$\sqrt{Hz}$ [139] has been reported which can be compared to zero-point fluctuations at quantum level. However, the usefulness of optical system is greatly limited when operated in a feedback loop. The signal conversion and path delay (in time domain) in an oscillating loop can transform into phase and frequency fluctuations which can severely degrade the noise and resolution. This is one of the main drawbacks of the proposed opto-electronic oscillator. However, the signal delay can be used advantageously to create a high stability and high spectral purity opto-electronic oscillator as shown in [140]. The time delay introduced by a long optical fiber in an oscillating loop is used to modulate the frequency output. This approaches leads to a quadratic decrease in the phase noise with increasing delay lines. Optical fiber is also virtually free from any frequency dependent loss. Injection locking [141] is yet another approach which

injects a delayed version of the output signal back to the oscillator and force the oscillator to lock to its "past." This prevents the oscillator from changing its frequency and phase and hence improves the phase noise. One trade-off here is that since the delay line influences the output frequency, the relative pressure sensitivity can be degraded and partly cancel the effect of reduced phase noise.

5-4-2 Canceling shunt capacitor C_o

The large shunt capacitor not only makes it difficult to implement an oscillator, it also put restrictions on the output tuning range. The series contact resistance forms a low pass filter with C_o which limits the performance at high frequencies. Therefore capacitive cancellation techniques become necessary. The most common way to cancel capacitive effects is to use it's dual counterpart i.e. an inductor. Active inductors are usually preferred because of size, compatibility and high Q but they add extra noise to the circuit. A better approach is to implement a negative capacitor in parallel to C_o by using a negative impedance converter as shown in [142]. Complete cancellation with low power is however a challenging task.

5-4-3 Temperature sensitivity

All MEMS material have a non-zero temperature coefficient which leads to long term frequency fluctuations (Typically $>$ 25ppm/^{0}C). Providing an accurate temperature insensitive output is one of the key parameter. In most cases, temperature compensation is obtained by sensing the temperature variations by PTAT (proportional-to-absolute temperature) references [143] and subsequently adjusting the output frequency. Alternatively, phase lock loop (PLL) method [144] is capable of providing a temperature drift less than 0.1ppm/^{0}C. Material based temperature compensation is also possible. In [145], addition of SiO_2 helps to reduce the drift but lowers the Q. Quartz resonators are less prone to temperature drifts but temperature compensation circuitry is an essential part of a MEMS oscillator. Comparison of temperature drift compensation techniques for MEMS resonators can be found in [43].

5-4-4 All-electrical MEMS oscillator

A good MEMS oscillator needs to be stable both in short term (low phase noise) and long term (temperature drift, aging etc.). The frequency sensitive element - resonator should have a low motional impedance, high Q and good power handling to suppress the effect of noise sources. Based on various oscillator topologies, piezoelectric and capacitive transduced oscillators have shown the ability to perform as good as quartz based oscillators. Capacitive resonators can offer high Q approaching the values obtained for Quartz resonators at low pressures. Piezoelectric resonators however exhibit lower Q due to material losses associated with the integrated piezoelectric layers and contact electrodes. An important factor for both resonators is the coupling coefficient η. The capacitive coupling coefficient η_{cap} results from the varying capacitance between two electrodes where as piezoelectric coupling coefficient η_{piezo} is the result of strain induced variations. However, η_{piezo} is typically much larger than η_{cap} which translates into lower motional impedance R_m. As such, in spite of lower Q, piezoelectric resonators exhibit low motional impedance. To obtain higher η and low R_m,

several parameters like bias voltage, area of the resonator, air gap etc. can be optimized. The overall coupling factor can also be increased through a combination of capacitive and piezoelectric transduction [146]. Furthermore, maximum frequency possible for piezoelectric oscillators ($\approx$1 GHz) is much higher than capacitive oscillators ($\approx$ 100 MHz). This is because at higher frequencies, R_m of a piezoelectric resonator decreases and is capable to keep up with C_o whereas for capacitive resonators, R_m is relatively insensitive to frequency scaling (depends on gap width).
Clearly, several factors need to be considered for selecting the right oscillator topology. A review literature on the past and existing MEMS electrical oscillators in [43] can serve as a starting point for development of MEMS oscillating pressure sensors.

Bibliography

[1] R. Feynman, *There is plenty of room at the bottom.* H.D. Gilbert (ed.), Miniaturization, Reinhold, New York, Page 282, 1961.

[2] C. Smith, *Piezoresistive effects in silicon and germanium.* Physical Review, Volume 94, Number 1, 1954.

[3] W. Pau and G. Pearson, *Pressure dependence of the resistivity of silicon.* Physical Review, Volume 98, Number 6, 1955.

[4] O. Tufte, P. Chapman, and D. Long, *Silicon diffused-element piezoresistive diaphragms.* Journal of Applied Physics, Volume 33, Number 11, 1961.

[5] L. Liang, S. Zhang, W. Park, J. Tsai, D. Kwong, and C. Lee, *Optimization of NEMS pressure sensors with a multilayered diaphragm using silicon nanowires as piezoresistive sensing elements.* Journal of Micromechanics and Microengineering- 22, 055012, 2012.

[6] B. Bhushan, *Nanotribology and Materials Characterization of MEMS/NEMS and BioMEMS/BioNEMS Materials and Devices.* Springer Handbook of Nanotechnology , Pages 1575-1638, 2007.

[7] R. Bogue, *MEMS sensor: past, present and future.* Sensor review, Volume 27, Number 1, 2007.

[8] R. Bogue, *Recent developments in MEMS sensors:a review of applications, markets and technologies.* Sensor Review, Volume 33, Number 4, 2013.

[9] M. Madou, *Fundamentals of Microfabrication: The Science of Miniaturization, 2nd Edition.* CRC, Boca Raton, 2002.

[10] W. Gopel, J. Hesse, and J. Zemel, *Sensors a comprehensive survey.* Mechanical Sensors, Volume 7, Weinham, New York, Pages 513-556, 1994.

[11] W. Eaton and J. Smith, *Micromachined pressure sensors:review and recent developments.* Smart Materials and structures-6, Pages 530-539, 1997.

[12] K. H. Kim, B. H. Kim, and Y. H. Seo, *A non-contact intraocular pressure measurement device using a micro reflected air pressure sensor for the prediagnosis of glaucoma.* Journal of Micromechanics and Microengineering 22, (035022), 2012.

[13] E. Peake, A. Zias, and J. Egan, *Solid-state digital pressure transducer.* Electron Devices, IEEE Transactions, Volume 16, Issue 10, 1969.

[14] K. Suja, V. Gopal, and R. Komaragiri, *Optimized design of a silicon based MEMS pressure sensor for wider range and better sensitivity.* Proceedings of the International Conference on Microelectronics, Communication and Renewable Energy (ICMiCR), 2013.

[15] A. Ghosh, S. Roy, and C. Sarkari, *Design and simulation of MEMS based piezoresistive pressure sensor for enhanced sensitivity.* Proceedings of the Energy Efficient Technologies for Sustainability (ICEETS), 2013.

[16] U. Aljancic, D. Resnik, D. Vrtacnik, M. Mozek, and S. Amoni, *Temperature Effects Modeling in Silicon Piezoresistive Pressure Sensor.* 11th Mediterranean Electrotechnical Conference (MELECON), 2002.

[17] P. Eswaran, , and S. Malarvizhi, *MEMS Capacitive Pressure Sensors:A Review on Recent Development and Prospective.* International Journal of Engineering and Technology (IJET) Volume 5, Number 3, 2013.

[18] H. E. A. Elgamel, *A simple and efficient technique for the simulation of capacitive pressure transducers.* Sensors and Actuators, Volume 77, Issue 3, Pages 183-186, 1999.

[19] S. Clark and K. Wise, *Pressure sensitivity in anisotropically etched thin-diaphragm pressure sensors.* IEEE Transactions on Electron Devices-26, Pages 1887-1896, 1979.

[20] W. Wang, N. Wu, Y. Tian, C. Niezrecki, and X. Wang, *Miniature all-silica optical fiber pressure sensor with an ultrathin uniform diaphragm.* Optics Express-9007, Volume 18, Number 9, 2010.

[21] D. Wagner, J. Frankenberger, and P. Deimel, *Optical pressure sensor using two Mach-Zehnder interferometers for the TE and TM polarization.* Journal of Micromechanics and Microengineering, Volume 4, Number 1, 1994.

[22] E. Stemme and G. Stemme, *A balanced dual-diaphragm resonant pressure sensor in silicon.* IEEE Transactions on Electron Devices, Volume 37, Issue 3, 1990.

[23] M. Andrews, G. Turner, P. Harris, and I. Harris, *A resonant pressure sensor based on a squeezed film of gas.* Sensors and Actuators, Volume 36, Issue 3, Pages 219-226, 20.

[24] D. Chen and D. Cui, *Measurement of resonant microbeam pressure sensors.* Proceedings of International Conference on Information Acquisition, 2004.

[25] P. Kinnella, M. Warda, and R. Craddock, *Physical characterization of selective stress coupling for resonant pressure sensors.* Sensors and Actuators A: Physical Volume 115, Issues 2-3, Pages 230-234, 2004.

[26] D. Chen, Z. Wu, X. Shi, and J. Wangl, *Design and modeling of an electromagnetically excited silicon nitride beam resonant pressure sensor.* 4th IEEE International Conference on Nano/Micro Engineered and Molecular Systems, 2009.

[27] G. Stemme, *Resonant silicon sensors.* Journal of Micromechanics and Microengineering-1, Pages 113-125, 1991.

[28] H. Jiao, B. Xie, J. Wang, D. Chen, and J. Chen, *Electrostatically driven and capacitively detected differential lateral resonant pressure microsensor.* Micro and Nano Letters, IET, Volume 8, Issue 10, 2013.

[29] C. J. Welham, J. Greenwood, and M. M. Bertioli, *A high accuracy resonant pressure sensor by fusion bonding and trench etching.* Sensors and Actuators, Volume 76, Issues 1âĂŞ3, Pages 298-304, 2000.

[30] L. Zhang, C. Zhang, and T. Shi, *Optimization Design of a Piezoelectric Transduction Silicon Resonant Pressure Sensor.* Advanced Materials Research, Pages 139-141, 2010.

[31] D. Randall, M. Rudkin, A. Cheshmehdoost, and B. Jones, *A pressure transducer using a metallic triple-beam tuning fork.* Sensors and Actuators, Volume 60, Issue 1-3, Pages 160-162, 1997.

[32] Q. Lia, S. Fana, Z. Tanga, and W. Xingl, *Non-linear dynamics of an electrothermally excited resonant pressure sensor.* Sensors and Actuators, Volume 188, Pages 19-28, 2012.

[33] L. Prochazka and T. Roesgen, *Optically interrogated MEMS pressure sensor array.* 14th International Symposium on Applications of Laser Techniques to Fluid Mechanics, Lisbon, Portugal, 2005.

[34] H. Unzeitig and H. Bartelt, *All-optical pressure sensor with temperature compensation on resonant PECVD silicon nitride microstructures.* Electronics Letters, Volume 28, Issue 4, 1992.

[35] D. Chen, Y. Li, M. Liu, and J. Wang, *Design and experiment of a laterally driven micromachined resonant pressure sensor for barometers.* Procedia Engineering, Volume 5, Pages 1490-1493, 2010.

[36] A. Baldi, W. Choi, , and B. Ziaie, *A Self-Resonant Frequency-Modulated Micromachined Passive Pressure Transensor.* IEEE Sensors Journal, Volume 3, Number 6, 2003.

[37] P. Melvas, E. Kalvesten, and G. Stemme, *A surface-micromachined resonant-beam pressure-sensing structure.* Journal of Microelectromechanical Systems, Volume 10, Number 4, 2001.

[38] D. Y. Shin, H. Lee, and S. Kim, *A delta-Sigma interface circuit for capacitive sensors with an automatically calibrated zero point,.* IEEE Transactions on Circuits and Systems II: Express Briefs, Volume 58, Pages 90-94, 2011.

[39] J. Geen, S. Sherman, J. Chang, and S. Lewis, *Single chip surface micromachined integrated gyroscope with 50 degree/h Allan deviation.* IEEE Journal of Solid-State Circuits, Volume 37, 2002.

[40] S. Sherman, *Low cost monolithic accelerometer.* Digital VLSI Circuits Symposium, Pages 34-35, 1992.

[41] C. Chiang, C. Wang, and Y. Huang, *A CMOS integrated capacitance-to-frequency converter with digital compensation circuit designed for sensor interface applications.* IEEE Proceedings of Sensors, Pages 954-957, 2007.

[42] D. Efstathios, K. Bitzaros, N. Stathopoulos, S. Pavlos, D. Goustouridis, and S. Chatzandroulis, *A Reconfigurable Multichannel Capacitive Sensor Array Interface.* IEEE transaction on instrumentation and Measurements, Volume 60, Number 9, 2011.

[43] J. T. M. van Beek and R. Puers, *A review of MEMS oscillators for frequency reference and timing applications.* Journal of Micromechanics and Microengineering- 22 (013001), 2012.

[44] J. Verd, A. Uranga, G. Abadal, J. L.Teva, F. Torres, J. Lopez, F. Murano, J. Esteve, and N. Barniol, *Monolithic CMOS MEMS Oscillator Circuit for Sensing in the Attogram Range.* IEEE electronic devices letters, Volume 29, Number 2, 2008.

[45] J. Verd, M. Sansa, A. Uranga, C. Pey, G. Abadal, F. Perez-Murano, and N. Barniol, *Monolithic CMOS-MEMS oscillators with micro-degree temperature resolution in air conditions.* Solid-State Sensors, Actuators and Microsystems Conference, 2009.

[46] S. Bedair and G. Fedder, *CMOS MEMS oscillator for gas chemical detection.* IEEE Proceedings of Sensors, 2004.

[47] H. Mamin and D. Rugar, *Sub-attonewton force detection at millikelvin temperatures.* Applied Physics Letters-79, 3358, 2001.

[48] J. Chaste, A. Eichler, J. Moser, G. Ceballos, R. Rurali, and A. Bachtold, *A nanomechanical mass sensor with yoctogram resolution.* Nature Nanotechnology-7, Pages 301-304, 2012.

[49] O. Arcizet, P. Cohadon, T. Briant, M. Pinard, and A. Heidmann, *Radiation-pressure cooling and optomechanical instability of a micromirror.* Nature-444, Pages 71-74, 2006.

[50] A. Connell, M. Hofheinz, M. Ansmann, R. Bialczak, M. Lenander, E. Lucero, M. Neeley, D. Sank, H. Wang, M. Weides, J. Wenner, J. Martinis, and A. Cleland, *Quantum ground state and single-phonon control of a mechanical resonator.* Nature-464, Pages 697-703, 2010.

[51] R. Barnoski, *Response of elastic structures to deterministic and random excitation.* Measurement Analysis Corporation, Los Angeles, MAC 403-04, 1965.

[52] F. R. Blom, S. Bouwstra, M. Elwenospoek, and J. H. Fluitman, *Dependence of the quality factor of micromachined silicon beam resonators on pressure and geometry.* Journal of Vacuum Science and Technology, Volume B10, Number 1, Pages 19-26, 1992.

[53] R. A. Buser and N. F. Rooij, *Silicon pressure sensor based on a resonating element.* Sensors and Actuators, A25-27, Pages 717-722, 1991.

[54] R. A. Buser and N. F. Rooij, *Capacitively Activated Torsional High-Q Resonator.* IEEE Proceedings of An Investigation of Micro Structures, Sensors, Actuators, Machines and Robots, Pages 132-135, 1990.

[55] M. Andrews, I. Harm, and G. Turner, *A comparison of squeeze-film theory with measurements on a microstructure.* Sensors and Actuators A, 36, Pages 79-81, 1993.

[56] J. Blech, *On Isothermal Squeeze Films.* Journal of Lubrication Technology 105(4), Pages 615-620, 1983.

[57] H. Hosaka, K. Itao, and K. S, *Damping characteristics of beam-shaped micro-oscillators.* Sensors and Actuators- A, Volume 49, Pages 87-95, 1995.

[58] G. Hakm, *The fluid mechanics of microdevices-the Freeman scholar lecture.* Journal of Fluids Engineering, ASME 121, Pages 5-33, 1999.

[59] S. M. Lee, *Viscous Damping Effect on the CMUT Device in Air.* Journal of the Korean Physical Society, Volume 58, Number 4, 2011.

[60] Z. Skvor, *On the Acoustical Resistance Due to Viscous Losses in the Air Gap of Electrostatic Transducers.* ACU STICA, Volume 19, 1967.

[61] T. Veijola, H. Kuisma, J. Lahdenpera, and T. Ryhanen, *Equivalent-circuit model of the squeezed gas ïňĄlm in a silicon accelerometer.* Sensors and Actuators A 48, Pages 239-248, 1995.

[62] R. Pratap, S. Mohite, and A. K. Pandey, *Squeeze Film effects in MEMS Devices.* Journal of the Indian institute of Science, Volume 87:1, 2007.

[63] M. Bao, *Micro Mechanical Transducer-Pressure Sensors, Accelerometers and Gyroscopes.* Elsevier, Amsterdam (Chapter 3), 2000.

[64] M. A. G. Suijlen, *Model-based design of MEMS resonant pressure sensors.* PhD dissertation, Technische Universiteit Eindhoven, 2011.

[65] A. W. Leissa, *Vibration of Plates.* , NASA SP-160, National Aeronautics and Space Administration, 1969.

[66] S. Timoshenko and S. W. Kreiger, *Theory of Plates and Shells.* 2nd edition, New York: McGraw-Hill Higher Education, 1964.

[67] S. Errede, *Vibrations of Circular Membranes (e.g. Drums) and Circular Plates.* UIUC Physics 193 POM Physics of Music/Musical Instruments, 2002.

[68] W. C. Young and R. G. Budynas, *Roarks Formulas for Stress and Strain.* Seventh Edition McGraw-Hill, 2001.

[69] I. O. Wygant and M. Kupnik, *Analytically Calculating Membrane Displacement and the Equivalent Circuit Model of a Circular CMUT Cell.* IEEE Proceedings of International Ultrasonics Symposium, 2008.

[70] C. F. Chiang, B. Andrew, B. J. Lee, C. H. Ahn, J. Eldwin, J. O. Gary, and T. W. Kenny, *Resonant pressure sensor with on-chip temperature and strain sensors for error correction.* 26th International Conference on Micro Electro Mechanical Systems (MEMS), Pages 45-48, 2013.

[71] X. Huang, S. Li, J. Schultz, Q. Wang, , and Q. Lin, *A Capacitive MEMS Viscometric Sensor for Affinity Detection of Glucose.* Journal of Microelectromechanical Systems, Volume 18, Number 6, 2009.

[72] P. French and A. Dorey, *Frequency output piezoresistive pressure sensor.* Sensors and Actuators- 4, Pages 77-83, 1983.

[73] J. Neumeister, G. Schuster, and W. von Munch, *A silicon pressure sensor using MOS ring oscillators.* Sensors and Actuators- 7, Pages 167-176, 1985.

[74] K. Oysted, *Piezoresistive CMOS-MEMS pressure sensor with ring oscillator readout including sigma-delta analog-to-digital converter on-chip.* Proceedings of the IEEE on Custom Integrated Circuits Conference, Pages 511-514, 20.

[75] D. Young, *Interface electronics for MEMS-based wireless sensing applications.* International Symposium on VLSI Design Automation and Test (VLSI-DAT), Pages 130-133, 2010.

[76] W. Hsu, *Recent progress in silicon MEMS oscillators.* Proceedings of 40th Annual Precise Time and Time Interval (PTTI) Meeting, Pages 135-46, 2008.

[77] A. Lacaita, S. Levantino, and C. Samori, *Integrated Frequency Synthesizers for Wireless Systems.* Cambridge: Cambridge University Press, 2007.

[78] S. Moore and S. Moheimani, *MEMS based oscillator incorporating a displacement sensor.* 3rd Australian Control Conference (AUCC), Pages 147-151, 2013.

[79] X. Yin, Q. Jiao, L. Yuan, and S.-H. Liou, *MEMS Torsion Oscillator Magnetic Field Sensor.* IEEE Transactions on Magnetics, Volume 49 , Issue. 7, 2013.

[80] T. A. Roessig, R. T. Hoew, A. P. Pisano, and J. H. smith, *Surface-micromachined resonant accelerometer.* Ninth international conference in solid state sensors and actuators, Pages 859-862, 1997.

[81] F. S. chun and J. Zhenhong, *On the Temperature Profile of the Thermally Excited Resonant Silicon Micro Structural Pressure Sensor.* Chinese Journal of Aeronautics, Volume 15, Number 3, 2002.

[82] F. He, R. Ribas, C. Lahuec, and M. Jezequel, *Discussion on the general oscillation startup condition and the Barkhausen criterion.* Analog Integrated Circuits And Signal Processing, Volume 59, Number 2, Pages 215-221, 2008.

[83] E. Vittoz, *Low-Power Crystal and MEMS Oscillators-The Experience of Watch Developments.* Integrated Circuits and Systems, Volume 0, 2010.

[84] A. Prak, M. Elwenspoek, and J. H. Fluitmen, *selective mode excitation and detection of micromachined resonators.* Journal of Microelectromechanical Systems, Volume 1, Number 4, 1992.

[85] B. Morgan, *Vertically-Shaped Tunable MEMS Resonators.* Journal of Microelectromechanical Systems, Volume 17, Number 1, 2008.

[86] S. Senturia, *Microsystems Design.* Norwell, MA: Kluwer, Page 252, 2000.

[87] J. J. M. Bontemps, *Design of a MEMS-based 52 MHz oscillator.* PhD thesis-Eindhoven University of Technology, 2011.

[88] J. D. Larson, S. Paul, D. Bradley, S. S. Wartenberg, and R. C. Ruby, *Modified Butterworth-Van Dyke Circuit for FBAR Resonators and Automated Measurement System.* IEEE Ultrasonic Symposium, 2000.

[89] B. D. Hauer, C. Doolin, K. S. D. Beach, and J. P. Davis, *A general procedure for thermomechanical calibration of nano/micro-mechanical resonators.* Annals of Physics 339, Pages 181-207, 2013.

[90] M. Lequime, *Fiber sensors for industrial applications.* Proceedings of the 12th International Conference on Optical Fibre Sensors, Volume 16 of OSA Technical Digest Series, Pages 66-71, 1997.

[91] J. Dakin and B. Culshaw, *Fiber Sensors: Principals and Components-Volume 1.* Artech, Boston, Mass, USA, 1988.

[92] Y. R. Garcia, J. M. Corres, and J. Goicoechea, *Vibration Detection Using Optical Fiber Sensors.* Journal of Sensors , Article ID 936487, 2010.

[93] U. Gunasilan, *Operative factors contributing to the selection of fiber-optic techniques for remote measurement of strain/stress.* Proceedings of the IEEE 9th International Conference on Computer and Information Technology, Middlesex University Dubai, 2009.

[94] S. Binu, V. P. M. Pillai, and N. Chandrasekaran, *Fibre optic displacement sensor for the measurement of amplitude and frequency of vibration.* Optics and Laser Technology, Volume 39, Number 8, Pages 1537-1543, 2007.

[95] T. K. Gangopadhyay, S. Chakravorti, S. Chatterjee, and K.Bhattacharya, *Multiple fringe and non sinusoidal signals obtained from a fiber-optic vibration sensor using an extrinsic Fabry-Perot interferometer.* Measurement Science and Technology, Volume 16, Pages 1075-1082, 2005.

[96] S. Pullteap, H. C. Seat, and T. Bosch, *Modified fringe counting technique applied to a dual-cavity fiber Fabry-Perot vibrometer.* Optical Engineering, Volume 46, Number 11, Article ID 115603, 2007.

[97] I. D. Villar, I. R. Matias, and F. J. Arregui, *Long-period fiber gratings with overlay of variable refractive index.* IEEE Photonics Technology Letters, Volume 17, Number 9, Pages 1893-1895, 2005.

[98] G. Meltz, W. W. Morey, W. H. Glenn, and J. D. Farina, *In fiber bragg-grating sensors.* Proceedings of the Optical Fiber Sensors, Volume 2, Pages 163-166, 1988.

[99] A. Cusano, A. Cutolo, J. Nasser, M. Giordano, and A. Calabro, *Dynamic strain measurements by fibre Bragg grating sensor.* Sensors and Actuators A, Volume 110, Number 1-3, Pages 276-281, 2004.

[100] J. P. A. Perez, S. C. Pueyo, and B. C. Lopez, *Automatic Gain Control-Techniques and Architectures for RF Receivers.* Springer New York Dordrecht Heidelberg London, 2011.

[101] T. H. Lee and A. Hajimiri, *Oscillator phase noise: A tutorial.* IEEE Journal of Solid-State Circuits, Volume 35, Number 3, Pages 326-336, 2000.

[102] G. Sauvage, *Phase noise in oscillators: A mathematical analysis of Leeson's model.* IEEE Transactions of Instrumentation and Measurements, Volume 26, Number 4,Pages 408-410, 1977.

[103] B. Razavi, *A study of phase noise in CMOS oscillators.* Journal of Solid-State Circuits, Volume 31, Number 3, Pages 331-343, 1996.

[104] W. Robins, *Phase Noise in Signal Sources (Theory and Applications).* IEE Telecommunication Series 9. London: Peter Peregrinus, 1982.

[105] V. Kaajakari, J. K. Koskinen, and T. Mattila, *Phase Noise in Capacitively Coupled Micromechanical Oscillators.* IEEE transactions on Ultrasonics, Ferroelectrics, and Frequency Control, Volume 52, Number 12, 2005.

[106] L. He, Y. P. Xu, and M. Palaniapan, *A State-Space Phase-Noise Model for Nonlinear MEMS Oscillators Employing Automatic Amplitude Control.* IEEE transactions on Circuits and Systems , Volume 57, Number 1, 2010.

[107] M. Agarwal, K. Park, M. Hopcroft, S. Chandorkar, B. Candler, R.N.and Kim, R. Melamud, G. Yama, B. Murmann, and Kenny, *Effects of mechanical vibrations and bias voltage noise on phase noise of MEMS resonator based oscillators.* Proceedings of MEMS (Istanbul), Pages 154-157, 2006.

[108] J. Vig, *Noise in microelectromechanical system resonators.* IEEE Transactions on Ultrasonics, Ferroelectrics and Frequency Control, Pages 1558-1565, 1995.

[109] D. Leeson, *A simple model of feedback oscillator noise spectrum.* Proceedings of IEEE , Pages 329-330, 1965.

[110] S. Lee and C. Nguyen, *Mechanically-coupled micromechanical resonator arrays for improved phase noise.* IEEE Proceeding of Frequency Control Sym. and Exposition, Pages 144-150, 2004.

[111] J. Malo and J. Izpura, *Simultaneous magnetic and electrostatic driving of microcantilevers.* Sensors and Actuators-136, Pages 347-357, 2007.

[112] A. Grant and L. McDonnell, *A non-contact mode scanning force microscope optimized to image biological samples in liquid.* Ultramicroscopy 97, Pages 177-184, 2003.

[113] A. Mehta, S. Cherian, D. Hedden, and T. Thundat, *Manipulation and controlled amplification of Brownian motion of microcantilever sensors.* Applied Physics Letters- 78, Pages 1637-1639, 2001.

[114] H. callen and T. Welton, *Irreversibility and generalized noise.* Physics Review- Vol 83, Number 1, Pages 34-40, 1951.

[115] M. C. Wang and G. Uhlenbeck, *On the theory of Brownian motions II.* Review of Modern Physics, Vol 17, 1945.

[116] A. N. Cleland and M. L. Roukes, *Noise processes in nanomechanical resonators.* Journal of Applied Physics, Volume 92, Number 5, 2002.

[117] J. A. Barnes, A. Chi, L. Cutler, J. Daniel, B. David, E. Tomas, A. James, L. Warren, F. C. Richard, L.and Robert, and M. R. Gremot, *Characterization of Frequency Stability.* IEEE transactions on Instrumentation and Measurements, Volume 20, Number 2, 1971.

[118] F. L. Walls, *Time-domain frequency stability calculated from the frequency domain:.* 4th European Proceedings of Frequency Time Forum, Swiss Foundation for Research in Microtechnology, Neuchatel, Switzerland, 1990.

[119] W. Riley, *Handbook of Frequency Stability Analysis.* NIST Special Publication 1065, 2008.

[120] T. Roessig, R. Howe, and A. Pisano, *Surface-micromachined 1 MHz oscillator with low-noise Pierce configuration.* Proceedings of Solid State Sensor and Actuator Workshop, 1998.

[121] D. Ruffieux, F. Krummenacher, A. Pezous, and D. Spinola, *Silicon resonator based 3.2 uW real time clock with 10 ppm frequency accuracy.* IEEE Journal of Solid-State Circuits 45, Pages 224-234, 2010.

[122] J. Hu, L. Callaghan, R. Ruby, and B. Otis, *A 50 ppm 600 MHz frequency reference utilizing the series resonance of an FBAR.* IEEE Radio Frequency Integrated Circuits Symp, Pages 325-328, 2010.

[123] V. Kaajakari, T. Mattila, A. Oja, J. Kiihamaki, and H. Seppa, *Square-extensional mode single-crystal silicon micromechanical resonator for low-phase-noise oscillator applications.* IEEE Electron Device Letters- 25 , Pages 173-175, 2004.

[124] E. Momosaki, *A Brief Review of Progress in Quartz Tuning Fork Resonators.* IEEE International Frequency Control Symposium, Pages 552-565,, 1997.

[125] A. C. Gomez, N. Agrait, and G. R. Bollinger, *Dynamics of quartz tuning fork force sensors used in scanning probe microscopy.* Nanotechnology- 20 , (215502), 2009.

[126] H. Edwards, L. Taylor, and D. W. Melmed, *high-resolution atomic force microscopy using a quartz tuning fork as actuator and sensor.* Journal of Applied Physics, Volume 82, 1997.

[127] A. Genis and D. E. Newell, *Using the X-Y flexure watch crystal as a pressure-force transducer.* Proceedings in 31st Annual Frequency Conference Symposium, Pages. 71-82, 1977.

[128] K. Kokubun, M. Hirata, M. Ono, H. Murakami, and Y. Toda, *Frequency dependence of a quartz oscillator on gas pressure.* Journal of Vacuum Science and Technology- 34, 1985.

[129] L. D. Landau and E. M. Lifshitz, *Fluid Mechanics.* Pergamon, London, Chapter 2, 1959.

[130] K. Kokubun, M. Hirata, M. Ono, H. Murakami, and Y. Toda, *A bending and stretching mode crystal oscillator as a friction vacuum gauge.* Journal of Vacuum Science and Technology- 3, 1984.

[131] S. H. Song, *Experimental Investigation of the Electrical Parameter Changes of Tuning Fork Crystal Oscillators Exposed to Air.* Japanese Journal of Applied Physics - 49, 2010.

[132] P. Spevak and P. Forstner, *MSP430 32-kHz Crystal Oscillators.* Texas Instruments Application Report, SLAA322B, 2006.

[133] R. J. Matthys, *Crystal oscillator circuits.* Krieger publishing company, 1992.

[134] W. Sansen, *Design of crystal oscillators-Analog Design Essentials.* The Springer International Series in Engineering and Computer Science, Volume 859, 2006.

[135] T. R. Albrecht, P. Grutter, D. Horne, and D. Rugar, *Frequency modulation detection using high Q cantilevers for enhanced force microscope sensitivity.* Journal of Applied Physics, Volume 69, Number 668, 1991.

[136] R. D. Middlebrook, *Optimum noise performance of transistor input circuits.* Philadelphia Transistor and Solid State Circuits Conference, 1958.

[137] F. Vanhelmont, P. Philippe, A. B. M. Jansman, R. Milsom, J. Ruigrok, and Oruk, *2 GHz reference oscillator incorporating a temperature compensated BAW resonator.* IEEE Ultrasonics Symposium, Pages 333-336, 2006.

[138] H. Lavasani, A. Samarao, G. Casinovi, and F. Ayazi, *A 145 MHz low phase-noise capacitive silicon micromechanical oscillator.* Proceedings of Electron Devices Meeting (IEDM), Pages 675-678, 2008.

[139] W. Hoogenboom, T. Frederix, J. Yang, S. Martin, Y. Pellmont, M. Steinacher, S. Zach, E. Langenbach, H. Heimbeck, A. Engel, , and H. Hug, *A Fabry-Perot interferometer for micrometer-sized cantilevers.* Applied Physics Letters 86, (074101), 2005.

[140] X. Yao and L. Maleki, *Optoelectronic microwave oscillator.* Journal of the Optical Society of America B, Volume 13, Number 8, Pages 1725-1735, 1996.

[141] X. Yao and L. Maleki, *Optoelectronic oscillator for photonic systems.* IEEE Journal of Quantum Electronics, Volume 32, Number 7, Pages 1141-1149, 1996.

[142] J. Linvill, *Transistor Negative-Impedance Converters.* Proceedings of the IRE, Volume 41, Number 6, Pages 725-729, 1953.

[143] M. Tsai, C. Yeh, Y. Cho, L. Ke, P. Chen, and G. Dehng, *A temperature compensated low noise digitally controlled crystal oscillator for multi standard applications.* Proceedings of Radio Frequency Integrated Circuits, Pages 553-556, 2008.

[144] Discera, *1.8V to 3.3V Pure silicon programmable oscillator Datasheet.* www.discera.com, 2010.

[145] W. Pang, R. P. R. Ruby and, P. Fisher, M. Unkrich, J., and Larson, *Temperature-Stable Film Bulk Acoustic Wave Oscillator.* IEEE electronic devices letters, Volume 29, Number 4, 2008.

[146] A. Samarao and F. Ayazi, *Combined capacitive and piezo-electric transduction for high performance silicon microresonators.* Proceedings of MEMS, Pages 169 172, 2011.

Glossary

List of Acronyms

MEMS	Micro-Electromechanical System
MST	Micro System Technology
LIGA	Lithographie Galvanoformung Abformung
DETF	double ended tuning fork
TETF	triple ended tuning fork
SEM	Scanning Electron Microscopy
ADC	Analog-to-Digital converter
CFC	Capacitance-to-Frequency Converter
CVC	Capacitance-to-Voltage Converter
VFC	Voltage-to-Frequency Converter
CMOS	Complementary Metal Oxide Semiconductor
EMI	Electro Magnetic Interference
AFM	Atomic Force Microscopy
PSD	Power Spectral Density
KCL	Kirchoff's Current Law
KVL	Kirchoff's Voltage Law
FP	Fabry Perot
FBG	Fiber Bragg Grating
LDV	Laser Doppler Vibrometry
AGC	Automatic Gain Control
SNR	Signal-to-Noise Ratio
BVD	Butter-worth Van Dyke